Tesi di Dottorato in Fisica

XXII Ciclo

FIS/03

ULTRACOLD BOSE-BOSE MIXTURES WITH TUNABLE INTERSPECIES INTERACTIONS

Giovanni Barontini

Supervisore:

Prof. Massimo Inguscio

Coordinatore:

Prof. Alessandro Cuccoli

Contents

Introduction

Every object in the universe, being it the most fundamental particle or the widest cluster of galaxies, can be classified on the base of its spin: if it is integer the object is said to be a *boson* while, if it is semi-integer, the object is said to be a *fermion*. At the energy scale we can experience in our life bosons and fermions behave in the same way but, when the energy (hence the temperature) is sufficiently low, matter unveils its wave-like nature and the quantum mechanics formalism replaces classical mechanics. In this framework the spin classification becomes of special importance: particles with integer spin follow Bose-Einstein statistics while particles with semi-integer spin follow Fermi-Dirac statistics, which implies the Pauli exclusion principle.

This thesis is devoted to the study of some properties of the bosonic part of matter in the vicinity of the absolute zero and, in particular, it deals with experiments with ultracold pure bosonic mixtures of ^{41}K and ^{87}Rb. The Bose-Einstein statistics was theoretically formulated in 1925 and is based on the fundamental concept of the indistinguishability of identical particles. The most fascinating prediction of this theory is the appearance, near the absolute zero, of a new state of matter: the Bose-Einstein condensate. Its experimental realization in the middle nineties [1, 2, 3] was the crowning of 70 years of efforts and was also the starting point of the flourishing branch of quantum degenerate gases physics. Nowadays, after more than ten years of experience, we are able to cool small samples (also fermionic [4]) of dilute gases near the absolute zero by means of several different techniques and we are also able to manipulate their properties by magnetic fields as well as laser light or low-frequency electromagnetic radiations.

The ability to completely control almost all the parameters of such systems has been the key feature of the success of the work on cold atoms. Indeed ultracold atoms have proven to be a powerful tool to experimentally reproduce and simulate a wide range of physical phenomena that have been studied theoretically but, often, not realized in other fields of physics. Among them the most notable examples being solid state physics (adding an optical lattice) [5], few-body physics [6, 7, 8]

and quantum computation [9, 10].

The above scenario can be enormously enriched when two gases of distinguishable atoms are brought near or below the quantum degeneracy threshold. A huge amount of literature exists dealing with Fermi-Bose mixtures but, up to now, the field of ultracold Bose-Bose mixtures is rather unexplored. The experiments presented in this thesis have been made to shine a light on this new field and, in particular, they are devoted to the study of the interactions between the two bosonic species.

In the context of the physics of cold atoms interactions can be easily tuned by means of the so-called Feshbach resonances. In the proximity of these resonances the s-wave scattering length, that is the quantity that parametrizes the low-energy collisions, can be varied at will changing the magnetic field acting on the atoms. In this thesis I report an extensive characterization of the interspecies scattering scenario for the ^{41}K-^{87}Rb bosonic mixture as a function of the magnetic field. The consequent precise knowledge of the interspecies scattering properties allows us to control the interaction between the two atomic clouds. We have exploited the ability to tune these interactions to perform several different experiments that can have a large impact on many fields of physics, such as the association of heteronuclear bosonic molecules and the detection of the Efimov effect in asymmetric systems.

Another interesting tool, presented here for the first time and peculiar of heteronuclear mixtures, is the species-selective dipole potential. By suitably arranging the laser frequency it is possible to produce a dipole potential that acts only on one of the two species. We have used this potential to perform two fascinating experiments dealing with very different phenomena and regarding some aspects of fundamental physics such as the thermodynamics near the absolute zero and the interactions between systems in different dimensions.

The thesis is organized according to the following scheme. In the first chapter I will introduce the main theoretical instruments concerning the scattering of neutral atoms, the Fano-Feshbach resonances and the mean-field theory of two interacting gases. In particular I will present the fundamental equations that are useful for the complete understanding of the rest of the manuscript.

In the second chapter I will briefly present the main features of the apparatus working at LENS for the production of the ultracold ^{41}K-^{87}Rb mixture.

The third chapter is devoted to the description of the experiments concerning the study of the interspecies interactions in the ^{41}K-^{87}Rb mixture. We have detected two s-wave and two d-wave Feshbach resonances and two zero crossings below 100 G. This has allowed us to produce the first double species Bose-Einstein condensate with

tunable interspecies interactions. Moreover we have been able to produce ultracold bosonic heteronuclear molecules starting from the two atomic clouds by means of resonant radio-frequency association. Finally we have detected three three-body losses peaks signalling the existence of heteronuclear Efimov trimers. These peaks represent the first experimental evidence of Efimov physics in asymmetric systems, a long-sought goal in the nuclear physics field.

In the final chapter I will report the experiments we have performed exploiting the species-selective dipole potential. We have studied the entropy exchange between the two ultracold gases induced by the selective compression. This has allowed us to implement a novel scheme for the reversible production of a K condensate and to explore many different trajectories in the temperature-entropy plane. In addiction we have employed the species-selective potential to produce the first experimentally controlled system of two interacting ensembles with different dimensions. Indeed the K sample, trapped in the anti-nodes of a species-selective optical lattice, can be considered two-dimensional while the Rb sample remains three-dimensional. In this fascinating system we have detected several inter-dimensional Feshbach resonances as the magnetic field or the confinement is varied. Investigating further possible developments of the species-selective potential, in the last section, I will present a theoretical study on the instabilities of the degenerate ^{41}K-^{87}Rb mixture in a species-selective optical lattice.

Chapter 1

Fundamental Concepts

In this first chapter I will give an overview on the basic concepts that are necessary for the understanding of the physics contained in this thesis. Since the interactions are the main subject of the experiments presented in chapter 3 and 4, the first section is devoted to the definition of the important quantities related to the scattering of neutral atoms. In the second section I will describe the physics of the Feshbach resonances, that are the essential tool to tune the interactions of cold atomic samples. In the third section I will give the mean-field equations for the description of two interacting Bose-Einstein condensates.

1.1 Scattering Theory

The relative motion of two atoms at energy E in a central potential is described, in polar coordinates, by the following Schrödinger equation:

$$\left[\frac{1}{2\mu} \left(p_r^2 + \frac{\mathbf{L}^2}{r^2} \right) + V(r) \right] \psi(r, \theta, \phi) = E\psi(r, \theta, \phi) \tag{1.1}$$

where μ is the reduced mass of the atom pair, $V(r)$ is the interaction potential and $\mathbf{L}$ the angular momentum operator. Because the operators $\mathbf{L}^2$ and L_z commute with the hamiltonian they share a complete set of eigenstates with the hamiltonian and the eigenfunction $\psi(r, \theta, \psi)$ must have the form

$$\psi(r, \theta, \phi) = R_l(r)Y_{lm}(\theta, \phi), \tag{1.2}$$

where Y_{lm} are the spherical harmonic function and the function R_l satisfies the radial wave equation

$$\left[\frac{\hbar^2}{2\mu} \left(-\frac{d^2}{dr^2} - \frac{2}{r}\frac{d}{dr} + \frac{l(l+1)}{r^2} \right) + V(r) \right] R_l(r) = ER_l(r). \tag{1.3}$$

The term $l(l+1)\hbar^2/2\mu r$ represents the rotational energy of the atom pair at a given distance and for a given rotational quantum number l. Let us now focus on two simple kinds of interaction potentials that will be useful in the following: an arbitrary short range potential and the Van der Waals potential.

Arbitrary Short Range Potential

A short range potential is a potential that can be neglected beyond a certain radius r_0, called the range of the potential. The latter can be estimated as the distance where the contribution of the kinetic energy equals that of the interaction potential: $|V(r_0)| = \hbar^2/\mu r_0^2$. From this it follows that $V(r)$ must fall faster than $1/r^2$ to be negligible at long distance. A more careful analysis can show that the potential has to fall faster than $1/r^s$ with $s = 2l + 3$ for the existence of a finite range r_0 [11].

For distances $r \gg r_0$ eq. (1.3) reduces to the spherical Bessel equation:

$$R_l'' + \frac{2}{r}R_l' + \left[k^2 - \frac{l(l+1)}{r^2}\right]R_l = 0 \tag{1.4}$$

where k is the wave number defined as $(2\mu E)^{1/2}/\hbar$. The general solution of eq. (1.4) is

$$R_l = C[\cos\eta_l j_l(kr) + \sin\eta_l n_l(kr)], \tag{1.5}$$

with j_l and n_l that are the spherical Bessel functions. For any finite value of k the expression above has the following asymptotic form

$$R_l(r) \simeq \frac{1}{r}\sin(kr + \eta_l - l\pi/2), \tag{1.6}$$

where η_l is the *collisional phase shift* that, in the case of free non-interacting atoms must vanish, and which is defined by [11]

$$\tan\eta_l \simeq -\frac{2l+1}{[(2l+1)!!]^2}(ka_l)^{2l+1} \tag{1.7}$$

in the limit $kr \to 0$. The constant a_l is the so-called *l*-wave *scattering length* which expresses the strength of the interaction potential. For the particular case of *s*-wave[1] collisions, that will be useful in the following, we can find that:

$$\tan\eta_0 \simeq -ka \tag{1.8}$$

and the asymptotic radial wave function becomes

$$R_0(r) \simeq C\left(1 - \frac{a}{r}\right). \tag{1.9}$$

---

[1] The partial waves associated with l=0,1,2 are called *s-*,*p-* or *d*-waves

Van der Waals Potential

The Van der Waals potential may be modelled by a potential consisting of a hard core and a $-1/r^6$ tail:

$$V(r) = \begin{cases} \infty & \text{for } r \leq r_c \\ -C_6/r^6 & \text{for } r > r_c \end{cases}, \tag{1.10}$$

the C_6 constant is called Van der Waals coefficient. For this potential there exists a finite range r_0 only for s-wave and p-wave collisions (see previous subsection). It can be easily demonstrated that for the Van der Waals potential the radial wave function, for $l = 0$, has the following form [11]:

$$R_0(r) = r^{1/2}[AJ_{1/4}(x) + BJ_{-1/4}(x)] \tag{1.11}$$

where J_n are the Bessel functions and $x = 2(r_0/r)^2$, with $r_0 = (2\mu C_6/16\hbar^2)^{1/4} = l_{VdW}$ the Van der Waals length.

	C_6 $(E_H a_0^6)$	l_{VdW} (a_0)
K-K	3897	65
K-Rb	4288	72
Rb-Rb	4691	83

Table 1.1: C_6 coefficient and Van der Waals length for the species involved in the experiments presented in this thesis. E_H is the Hartreee energy $\hbar c\alpha/a_0$. Data from [12, 13].

In the long range regime $r \gg r_0(x \ll 1)$ we can take the leading term of the Bessel functions $J_{\pm n}(x) = (x/2)^{\pm n}/\Gamma(1 \pm n)$ and, choosing $B = r_0^{1/2}\Gamma(3/4)$, the radial wave function is asymptotically normalized to unity and has the form

$$R_0(r) \simeq Br^{1/2}\left[\frac{A}{B}\frac{(x/2)^{1/4}}{\Gamma(5/4)} + \frac{(x/2)^{-1/4}}{\Gamma(3/4)}\right] = 1 - \frac{a}{r}, \tag{1.12}$$

similar to the case of the short range potential, with[2]

$$a = r_0 2^{-1/2}\frac{\Gamma(3/4)}{\Gamma(5/4)}[1 - \tan(x_c - 3\pi/8)] = \bar{a}[1 - \tan(x_c - 3\pi/8)] \tag{1.13}$$

the scattering length, which diverges for $2(r_0/r_c)^2 - 3\pi/8 = (N + 1/2)$ with $N = 0, 1, 2, \ldots$ As expected, for l-wave collisions, the Van der Waals potential behaves like a short range potential.

---

[2]Imposing the boundary condition $R_0(r_c) = 0$ for $r_c \ll r_0$ we have $A/B = -J_{-1/4}(x_c)/J_{1/4}(x_c) \rightarrow -2^{-1/2}[1 - \tan(x_c - 3\pi/8)]$ [11].

Elastic Scattering of Neutral Atoms

Let us consider two distinguishable atoms moving in free space. We can define the relative momentum $\mathbf{p} = \mu(\mathbf{v}_1 - \mathbf{v}_2) = \hbar\mathbf{k}$ and the relative motion may be described by a plane wave e^{ikz} (for simplicity the direction of $\mathbf{p}$ is chosen along the z axis) so that the relative kinetic energy is given by $E = \hbar^2 k^2/2\mu$. If the atoms can scatter *elastically* under the influence of a central potential $V(r)$, the wave function, outside the region of overlap between the scattered wave and the incident wave ($r \to \infty$), must be of the form:

$$\psi_k(r) \sim e^{ikz} + f(\theta)\frac{e^{ikr}}{r} \tag{1.14}$$

where the second term represent the scattered wave and the coefficient $f(\theta)$, which is the probability amplitude for scattering over an angle θ, is called *scattering amplitude*. The general solution of a particle in a central potential field can be expressed in terms of the complete set of eigenfunctions $Y_{lm}(\theta, \phi)$ and $R_l(r)$:

$$\psi(r, \theta, \phi) = \sum_{l=0}^{\infty} \sum_{m=-l}^{l} c_{lm}(k)R_l(r)Y_{lm}(\theta, \phi); \tag{1.15}$$

this expression is known as the *partial wave expansion.*

Let us now consider, without losing generality, only those wave functions with axial symmetry along the z axis; due to the fact that they are ϕ independent we have $c_{lm\neq0} = 0$, and the partial wave expansion becomes

$$\psi_k(r, \theta) = \sum_{l=0}^{\infty} c_l(k)R_l(r)P_l(\cos\theta), \tag{1.16}$$

where P_l are Legendre polynomials.

We can now substitute eq. (1.6) for short range potentials in eq. (1.16) and we can choose the c_l coefficients imposing that the partial wave expansion must have the asymptotic form (1.14):

$$\psi_k(r, \theta) \simeq \frac{1}{2ikr} \sum_{l=0}^{\infty} (2l + 1)P_l(\cos\theta)((-1)^{l+1}e^{-ikr} + e^{2i\eta_l}e^{ikr}). \tag{1.17}$$

Also the incoming wave function can be expanded in terms of Legendre polynomials

$$e^{ikz} \simeq \frac{1}{2ikr} \sum_{l=0}^{\infty} (2l + 1)P_l(\cos\theta)((-1)^{l+1}e^{-ikr} + e^{ikr}) \tag{1.18}$$

and, consequently, the scattering amplitude is

$$f(\theta) = \frac{1}{2ik} \sum_{l=0}^{\infty} (2l + 1)(e^{2i\eta_l} - 1)P_l(\cos\theta). \tag{1.19}$$

The relation between the scattering amplitude and the total cross section is given by the well-known optical theorem

$$\sigma = \sum_{l=0}^{\infty} \sigma_l = \frac{4\pi}{k^2} \sum_{l=0}^{\infty} (2l+1)\sin^2\eta_l = \frac{4\pi}{k}\Im f(0), \tag{1.20}$$

from which follows the *unitary limit* for the partial wave contribution:

$$\sigma_l \leq \frac{4\pi}{k^2}(2l+1). \tag{1.21}$$

Using eqs. (1.20) and (1.7) we can find that, for low energy ($k \to 0$), the cross section depends only on the *s*-wave scattering length:

$$\sigma \sim 4\pi a^2. \tag{1.22}$$

In case of identical particles it's not possible to distinguish between the situation described above and the one where the two atoms are initially interchanged (i.e. described by e^{-ikz}) but scattered in the same direction (i.e. over an angle $\pi - \theta$). The asymptotic wave function can be indeed expressed as the following linear combination:

$$\psi(r,\theta) \sim A\left(e^{ikz} + f(\theta)\frac{e^{ikr}}{r}\right) + B\left(e^{-ikz} + f(\pi-\theta)\frac{e^{ikr}}{r}\right) \tag{1.23}$$

with $|A| = |B|$. The scattering amplitude becomes [11]

$$f(\theta) \pm f(\pi-\theta) = \frac{2}{ik}\sum_{l=odd(even)}(2l+1)(e^{i\eta_l}-1)P_l(\cos\theta) \tag{1.24}$$

while the cross section

$$\sigma = \frac{8\pi}{k^2}\sum_{l=even(odd)}(2l+1)\sin^2\eta_l, \tag{1.25}$$

where the even terms run for bosons and the odd terms for fermions. For low energy ($k \to 0$), using eqs. (1.25) and (1.7), we can find that

$$\sigma \sim \begin{cases} 8\pi a^2 & \text{for bosons} \\ 8\pi a_1^2(ka_1)^4 & \text{for fermions.} \end{cases} \tag{1.26}$$

1.2   Fano-Feshbach Resonances

In the previous section I described the *elastic* scattering between two cold atoms in a central potential that leaves the internal state of the atoms unchanged. However, in

general, the interaction potential depends on the internal states of the atoms and it may happen that, during the collision, the internal states change and the atoms may be bound in a molecular state. Let us consider as an example the case of two $^2S_{1/2}$ (alkali) atoms in their electronic ground state. Since the electronic motion is faster than the nuclear motion the electronic wave function can adapt itself adiabatically to the position of the nuclei; this allows us to decouple the two motions (Born-Oppenheimer approximation). The resulting potentials, calculated for a set of fixed nuclear distances, are called *adiabatic potentials*.

The unpaired electron spins $\mathbf{s}_1$ and $\mathbf{s}_2$ can be coupled to a total spin $\mathbf{S} = \mathbf{s}_1 + \mathbf{s}_2$ with the associated quantum numbers $S= 0$, which corresponds to the *singlet* state, or $S =1$, which corresponds to the *triplet* state. The corresponding adiabatic potentials are usually labelled as $^1\Sigma_g^+$ and $^3\Sigma_u^+$ respectively. The notation Σ refers to the zero projection of the electronic orbital angular momentum on the interatomic axis. The label $+$ indicates that the electronic wave function is left unchanged upon reflection in a plane containing the nuclei while g and u are associated with the *gerade* and *ungerade* symmetry upon inversion through the geometric center of the molecule. Obviously, if the atoms are of different species, the u and g symbols are dropped. For long interatomic distances the $^1\Sigma^+$ and $^3\Sigma^+$ potentials are identical and behave like the Van der Waals tail $\sim -C_6/r^6$ while, for short distances, where the two electronic clouds overlap, the two potentials split (see Fig. 1.1).

Let us now consider the hyperfine interaction between the nuclear spin $\mathbf{i}$ and the electronic spin $\mathbf{s}$ described by the total angular momentum $\mathbf{f} = \mathbf{s}+\mathbf{i}$. For alkali atoms the total momentum quantum numbers are $f = i \pm 1/2$ and the difference in energy between these two hyperfine levels is the hyperfine splitting E_{hf}. This splitting and the magnetic Zeeman energy are typically large compared to the kinetic energy in cold collisions. Consequently, the scattering properties of two atoms depend strongly on the states in which they are prepared. A scattering channel can be labelled by specifying the quantum numbers that describe each of the two initially separated atoms and the total angular momentum: $\alpha = \{f_1 m_{f1} f_2 m_{f2} l m_l\}$. For identical bosons (fermions) in the same Zeeman level only even (odd) l channels can exist. This basis is called the asymptotic basis since it is the most convenient at long range, when the electronic spins couple with the nuclear spin of the same atom. When the interatomic distance is reduced below a certain r_u, where the difference between the two Born-Oppenheimer potential equals E_{hf} (see Fig. 1.1), the two electronic spins decouple from the nuclear spins to couple between them. Consequently f, m_f are no more good quantum numbers.
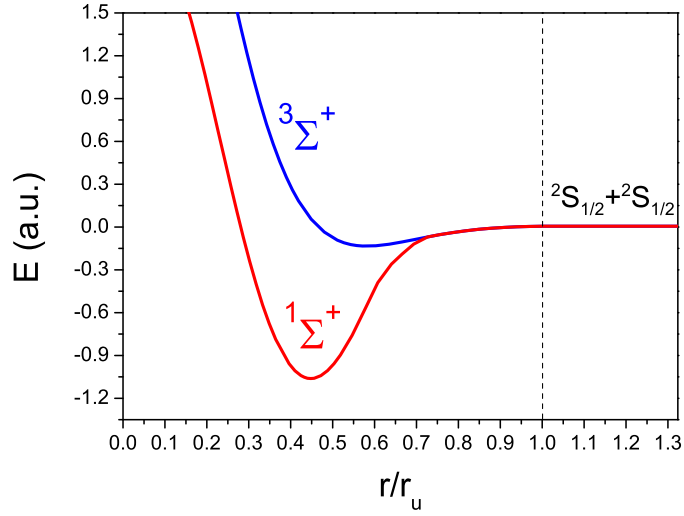
Figure 1.1: Example of $^1\Sigma^+$ and $^3\Sigma^+$ adiabatic potential curves for a dimer molecule of alkali atoms. r_u is the uncoupling distance (see text).

If the channel energy $E_\alpha = E_{f_1 m_{f1}} + E_{f_2 m_{f2}}$ is lower than the total energy of the system E the channel is said to be *open*, vice versa it is said to be *closed*. The radial wave equation now takes the form [14]:

$$R''_\alpha(E,r) + \frac{2}{r}R'_\alpha(E,r) + \frac{2\mu}{\hbar^2}\sum_\beta[E\delta_{\alpha\beta} + V_{\alpha\beta}(r)]R_\beta(E,r) = 0, \qquad (1.27)$$

where the potential $V_{\alpha\beta}$ has the following expression

$$V_{\alpha\beta}(r) = \left[E_{f_1 m_{f1}} + E_{f_2 m_{f2}} + \frac{l(l+1)\hbar^2}{2\mu r^2}\right]\delta_{\alpha\beta} + V_{\alpha\beta}^{int}(r). \qquad (1.28)$$

The first three terms, that express the separated atomic energies and the kinetic energy of axis rotation, are diagonal in the asymptotic base. The Born-Oppenheimer potentials and the spin-dependent interactions are contained in the $V_{\alpha\beta}^{int}$ term that is nondiagonal in the asymptotic base, since it describes the short range interactions. This last term can be decomposed in two parts:

$$V^{int}(r) = V_{el}(r) + V_{SS}(r). \qquad (1.29)$$

The contribution V_{el}, which is diagonal in l but not in $f_1 m_{f1} f_2 m_{f2}$, takes into account the strong electronic interaction. It is responsible for elastic scattering and inelastic spin-exchange collisions and gives rise to the broadest scattering resonances. The V_{SS} contribution is nondiagonal in $l f_1 m_{f1} f_2 m_{f2}$ and takes into account the weak
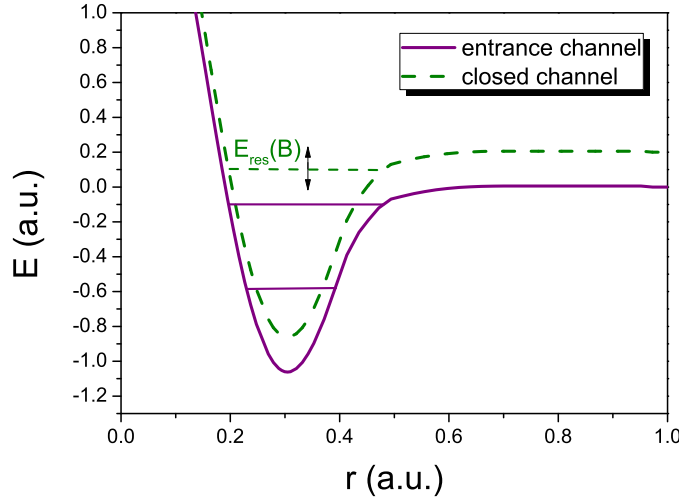
Figure 1.2: Pictorial scheme of open and closed channel potentials. The open channel threshold and the energy of one of the closed channel levels are very close and they may cross each other once an external magnetic field is applied.

spin-spin interaction. An example of short-range base, on which V_{el} is diagonal, can be obtained coupling $\mathbf{s}_1$ and $\mathbf{s}_2$ to a resultant $\mathbf{S}$ and $\mathbf{i}_1$ and $\mathbf{i}_2$ to $\mathbf{I}$. Then we can couple $\mathbf{S}$ and $\mathbf{I}$ to $\mathbf{F}$ which couples to $\mathbf{L}$ to give the total angular momentum $\mathbf{F}_{tot}$. The corresponding base is $\{SIFlF_{tot}M_{tot}\}$, with M_{tot} the projection of $\mathbf{F}_{tot}$ onto the magnetic field axis.

We saw in the previous section that, at low temperatures, the cross section depends only on the s-wave scattering length (eq. (1.22)). In general the scattering length is only weakly dependent on the magnetic-field strength B, unless B can be tuned in such a way that a closed-channel level crosses the entrance-channel scattering threshold (see Fig. 1.2). This may occur due to a difference in the magnetic moments of the entrance channel, $\partial E_\alpha/\partial B$, and of the closed channel, $\partial E_\beta/\partial B$. When the energies of the scattered atoms and of the resonant level are nearly matched, the metastability of the resonant state leads to a time delay during the collision. This causes an enhancement of the collisional phase shift and, consequently, of the scattering length. This resonant phenomenon, called *Fano-Feshbach resonance*, can indeed be used to tune the scattering length around the magnetic field B_0 associated with the singularity of a. The mechanism of Feshbach resonances can be understood using the simple approach of the two channel picture, reported in the following.

The Two-Channel Model

The accurate description of Feshbach physics requires very complicated models based on realistic molecular potentials, however, for the purposes of this thesis, it is sufficient to follow a simpler approach. Indeed, the physics of binary collisions, as well as the properties of highly excited bound states, can be well described in terms of just two scattering channels. This can be justified by the fact that, even if the spin configuration of the entrance channel is in general coupled to several closed scattering channels, the coupling is usually due to the near degeneracy of the energy of a single metastable vibrational state with the energy of the colliding atoms.

The hamiltonian for the relative motion of two colliding atoms is given by the following matrix:

$$H = \begin{pmatrix} H_{en} & W(r) \\ W(r) & H_{cl} \end{pmatrix} \tag{1.30}$$

where W are the energies associated with the spin exchange (or dipole) interaction and provide the inter-channel coupling. The diagonal elements H_{en} and H_{cl} are the entrance- and closed-channel hamiltonians in the absence of coupling, given by

$$H_{en} = -\frac{\hbar^2 \nabla^2}{2\mu} + V_{en}(r) \tag{1.31}$$

$$H_{cl} = -\frac{\hbar^2 \nabla^2}{2\mu} + V_{cl}(B, r). \tag{1.32}$$

Here and for the following, the threshold energy of the entrance channel is chosen to be the zero energy. For this reason the dependence of the hamiltonian on the magnetic field B is contained only in V_{cl}. The closed-channel hamiltonian must support the bare Feshbach resonance state: $H_{cl}|\phi_{res}\rangle = E_{res}(B)|\phi_{res}\rangle$. Again, $E_{res}(B)$ can be tuned with respect to the entrance threshold energy through the external magnetic field. In the asymptotic region $r \to \infty$ ($V_{en} \to 0$) the entrance-channel continuum wave function ϕ_k^+ must instead satisfy $H_{en}|\phi_k^+\rangle = (\hbar^2 k^2/2\mu)|\phi_k^+\rangle$ and must have the same behaviour as eq. (1.14), defining f_{bg} as the associated scattering amplitude.

In general, the atomic wave functions will have the form $S_{en}|\phi_{en}\rangle + S_{cl}|\phi_{cl}\rangle$, with S_{en} and S_{cl} the entrance- and closed-channel spin configurations. From eq. (1.30) follows that the $|\phi_{en}\rangle$ and $|\phi_{cl}\rangle$ components are determined by the following set of coupled Schrödinger equations

$$\begin{aligned} H_{en}|\phi_{en}\rangle + W(r)|\phi_{cl}\rangle &= E|\phi_{en}\rangle \\ H_{cl}|\phi_{cl}\rangle + W(r)|\phi_{en}\rangle &= E|\phi_{cl}\rangle. \end{aligned} \tag{1.33}$$

Solutions with negative energies are associated to molecular bound states while those with positive energies belong to the continuum spectrum and describe collisions between initially separated atoms. At asymptotically large interatomic distances the entrance-channel components must behave like eq. (1.14), while the closed channel components must decay exponentially.

Let us define the Green's functions

$$G_{en}(z) = \left[z - \left(-\frac{\hbar^2 \nabla^2}{2\mu} + V_{en} \right) \right]^{-1} \qquad (1.34)$$

$$G_{cl}(B, z) = \left[z - \left(-\frac{\hbar^2 \nabla^2}{2\mu} + V_{cl}(B) \right) \right]^{-1} \qquad (1.35)$$

where z have the dimensions of an energy. We can now rewrite Eqs. (1.33) as:

$$\begin{aligned}
|\phi_{en}\rangle &= |\phi_k^+\rangle + G_{en}(E + i0) W |\phi_{cl}\rangle \\
|\phi_{cl}\rangle &= G_{cl}(B, E) W |\phi_{en}\rangle.
\end{aligned} \qquad (1.36)$$

It can be demonstrated [14] that the asymptotic behaviour of G_{en} has the following form in spatial coordinates:

$$G_{en}(z, \mathbf{r}, \mathbf{r}') \sim -\frac{2\mu(2\pi\hbar)^{3/2}}{4\pi\hbar^2} \frac{e^{ikr}}{r} [\phi_k^-(\mathbf{r}')]^* \qquad (1.37)$$

with $\phi_k^-(\mathbf{r}') = [\phi_{-k}^+(\mathbf{r}')]^*$, while, in the single resonance approach, we have

$$\langle \phi_{res} | G_{cl}(B, E) | \phi_{res} \rangle = (E - E_{res}(B))^{-1} = \Delta E^{-1}. \qquad (1.38)$$

Usually the resonance detuning ΔE is negligible compared with the spacing between the discrete energy levels of H_{cl}. Consequently the G_{cl} function is dominated by the contribution associated with the Feshbach resonance level, thus we can write

$$G_{cl}(B, E) \simeq |\phi_{res}\rangle \Delta E^{-1} \langle \phi_{res}|, \qquad (1.39)$$

that, inserted in the second of eqs. (1.36), leads to the following expression for the overlap factor:

$$\langle \phi_{res} | \phi_{cl} \rangle = A(B, E) = \langle \phi_{res} | W | \phi_{en} \rangle \Delta E^{-1}. \qquad (1.40)$$

We can now substitute $|\phi_{cl}\rangle$ in favour of A and $|\phi_{res}\rangle$ in eqs. (1.36) obtaining

$$\begin{aligned}
|\phi_{en}\rangle &= |\phi_k^+\rangle + G_{en}(E + i0) W |\phi_{res}\rangle A(B, E) \\
|\phi_{cl}\rangle &= |\phi_{res}\rangle A(B, E)
\end{aligned} \qquad (1.41)$$

and, hence,

$$A(B, E) = \frac{\langle \phi_{res} | W | \phi_k^+ \rangle}{\Delta E(B) - \langle \phi_{res} | W G_{en}(E + i0) W | \phi_{res} \rangle}. \tag{1.42}$$

Once all the energy states associated with V_{en} and the resonance state are known, eqs. (1.41) and (1.42) establish the complete solution of the coupled equations (1.36). We note here that the only dependence on the magnetic field is contained in the detuning ΔE. Usually it is sufficient to take only the linear leading term of the expansion around $E_{res}(B_{res}) = 0$, obtaining $E_{res}(B) \simeq \mu_{res}(B - B_{res})$. The coefficient μ_{res} is the difference between the magnetic moments of the Feshbach resonance state and a pair of asymptotically separated atoms.

In the asymptotic region, using eqs. (1.37) and (1.41), we can find that the scattering amplitude has the form:

$$f(\theta, k) = f_{bg}(\theta, k) - \frac{2\mu(2\pi\hbar)^{3/2} \langle \phi_k^- | W | \phi_{res} \rangle}{4\pi\hbar^2} A(B, E) \tag{1.43}$$

that, in the zero momentum limit, leads to the well-known expression for the scattering length

$$a(B) = a_{bg} \left(1 - \frac{\Delta B}{B - B_0} \right). \tag{1.44}$$

The parameter a_{bg} is associated to the bare scattering amplitude f_{bg} and is called background scattering length. The width of the resonance ΔB is given by

$$\Delta B = \frac{2\mu(2\pi\hbar)^{3/2}}{4\pi\hbar^2 a_{bg} \mu_{res}} |\langle \phi_{res} | W | \phi_0^+ \rangle|^2 \tag{1.45}$$

and the resonance position B_0 is

$$B_0 = B_{res} - \langle \phi_{res} | W G_{en}(0) W | \phi_{res} \rangle / \mu_{res}. \tag{1.46}$$

Universal Properties of Molecular Bound States

Let us consider the dressed molecular bound state determined, similarly to eqs. (1.36), by the following coupled equations:

$$\begin{aligned}
|\phi_b^{en}\rangle &= G_{en}(E_b) W | \phi_b^{cl}\rangle \\
|\phi_b^{cl}\rangle &= G_{cl}(E_b, B) W | \phi_b^{en}\rangle.
\end{aligned} \tag{1.47}$$

Here the bound state energy E_b is negative and both channels are closed. From eq. (1.39) and from the normalization condition $\langle \phi_b^{en} | \phi_b^{en} \rangle + \langle \phi_b^{cl} | \phi_b^{cl} \rangle = 1$ follows that

the previous set of equations can be rewritten as

$$
\begin{aligned}
|\phi_b^{en}\rangle &= \frac{1}{C} G_{en}(E_b) W |\phi_{res}\rangle \\
|\phi_b^{cl}\rangle &= \frac{1}{C} |\phi_{res}\rangle
\end{aligned}
\tag{1.48}
$$

where the normalization constant C has the following expression

$$
C = \sqrt{1 + \langle \phi_{res} | W G_{en}^2 W | \phi_{res} \rangle}.
\tag{1.49}
$$

From eqs. (1.47) follows also that the molecular binding energy can be expressed as

$$
E_b = \mu_{res}(B - B_{res}) + \langle \phi_{res} | W G_{en}(E_b) W | \phi_{res} \rangle.
\tag{1.50}
$$

This equation recovers eq. (1.46) in the limits $E_b \to 0$ and $B \to B_0$ if the magnetic field strength approaches B_0 from the side of positive scattering lengths. This directly implies that the binding energy of the Feshbach molecule vanishes at B_0. It can be demonstrated [14] that, from eq. (1.50), follows that

$$
E_b(B) = -\frac{\hbar^2}{2\mu[a_{bg}\Delta B/(B - B_0)]^2}
\tag{1.51}
$$

which, in the limit $B \to B_0$, becomes the well-known expression for the binding energy in the universal regime:

$$
E_b(B) = -\frac{\hbar^2}{2\mu a(B)^2}.
\tag{1.52}
$$

The range in the magnetic field strength where the molecular state, as well as its binding energy, only depend on the scattering length a is usually called the *universal regime*. Its existence is common to all Feshbach resonance phenomena in cold gases.

In accordance with the second of eqs. (1.47) we can now write, for the closed-channel component of the Feshbach molecule, that

$$
\langle \phi_b^{cl} | \phi_b^{cl} \rangle = C^{-2} = Z(B)
\tag{1.53}
$$

with the renormalization constant Z that can be expressed [14] as

$$
Z(B) = \frac{1}{\mu_{res}} \frac{\partial E_b}{\partial B} \sim \frac{\hbar^2}{2\mu a^2} \frac{2a}{\Delta B a_{bg}}
\tag{1.54}
$$

where the last passage is valid for $B \to B_0$ from the side of positive scattering length. From this equation follows that the normalization constant C diverges approaching

B_0, where $a \to \infty$. This implies that the closed-channel admixture is negligible in the universal regime and that the Feshbach molecule can be described in terms of just its entrance-channel component in the proximity of B_0. As a consequence, the coupling between the channels, in the vicinity of a Feshbach resonance, can be treated as a perturbation of V_{en} and the whole potential matrix can be replaced by the appropriate single-channel potential $V(B, r)$. Therefore we can replace the two-body hamiltonian matrix of eq. (1.30) with the single-channel hamiltonian

$$H = -\frac{\hbar^2}{2\mu}\nabla^2 + V(B, r). \tag{1.55}$$

The corresponding scattering length recovers eq. (1.13) and the binding energy, in the limit $a \gg \bar{a}$, is

$$E_b \approx -\hbar^2/2\mu(a - \bar{a})^2. \tag{1.56}$$

When the binding energy is well approximated by eq. (1.56) and when

$$\left| E_b(B) + \frac{\hbar^2}{2\mu(a(B) - \bar{a})^2} \right| < \left| E_b(B) + \frac{\hbar^2}{2\mu a^2(B)} \right| \tag{1.57}$$

the Feshbach resonance is denoted as entrance-channel dominated. Conversely, those resonances in which the properties of the bound states become universal only in a narrow region in the vicinity of B_0 are called closed-channel dominated.

We can finally estimate the size of the universal regime from eqs. (1.44) and (1.54) as the region where

$$\left| \frac{B - B_0}{\Delta B} \right| \ll 2\mu a_{bg}^2 \frac{|\mu_{res}\Delta B|}{2\hbar^2}. \tag{1.58}$$

From this equation and from eq. (1.57) we can extract a criterion for the classification of the Feshbach resonances: if

$$\eta = \left| \frac{2\bar{a}}{a_{bg}\mu_{res}\Delta B} \frac{\hbar^2}{2\mu\bar{a}^2} \right| \ll 1 \tag{1.59}$$

the resonance is open-channel dominated; vice versa if $\eta \gg 1$ a resonance is referred to as closed-channel dominated. We will see in chapter 3 that in our system there are one open-channel resonance and one closed-channel resonance below 100 G.

1.3 Mean-Field Equations for Degenerate Bose-Bose Mixtures

Up to now I described the collision properties of two atoms in the low energy regime, be they either bosons or fermions. Since this thesis deals with experiments on pure

bosonic mixtures, I will consider only bosons in the following. In particular, in this section, I will jump from the single-particle treatment to the many-particles treatment, that is at the base of the so-called *mean-field* theory. The equations provided by this theory are appropriate to describe the behaviour of degenerate Bose gases and, in this section, I will give their extension to the case of two interacting Bose-Einstein condensates.

It is well-known that for a Bose gas in a harmonic trap there exist a transition temperature for the Bose-Einstein condensation given by

$$T_c = \frac{0.94\hbar\omega_{ho}N^{1/3}}{k_B},\tag{1.60}$$

where ω_{ho} is the mean frequency of the harmonic potential and N the total number of atoms. In a binary bosonic mixture there are two different critical temperatures, one for each species, and the so-called double Bose-Einstein condensation occurs when the temperature is below the lowest T_c. The many body hamiltonian describing a two species gas of interacting bosons in an external potential V^{ext} is given, in second quantization, by [15]

$$\hat{H} = \sum_{i=1}^{2}\left\{\int d^3x\hat{\Psi}_i^*(\mathbf{x})\left[-\frac{\hbar^2\nabla^2}{2m_i}+V_i^{ext}(\mathbf{x})\right]\hat{\Psi}_i(\mathbf{x})+\right.$$
$$\left.+\sum_{j=1}^{2}\frac{1}{2^{\delta_{ij}}}\int d^3x d^3x'\hat{\Psi}_i^*(\mathbf{x})\hat{\Psi}_j^*(\mathbf{x}')V_{ij}(\mathbf{x}-\mathbf{x}')\hat{\Psi}_i(\mathbf{x})\hat{\Psi}_j(\mathbf{x}')\right\}\tag{1.61}$$

where $\hat{\Psi}_i$ and $\hat{\Psi}_i^*$ are the annihilation and creation bosonic field operators and $V_{ij}(\mathbf{x}-\mathbf{x}')$ is the two body interatomic potential. From the Bogoliubov's mean-field theory the condensate wave functions are defined as the expectation values of the field operators: $\Psi_i = \langle\hat{\Psi}_i\rangle$. The condensate densities are fixed by $|\Psi_i(\mathbf{x},t)|^2 = n_{i0}(\mathbf{x},t)$, that lead to the normalization conditions $\int|\Psi_i|^2 = N_i$.

The equations for the condensate wave functions are obtained from the Heisenberg equations:

$$i\hbar\frac{\partial}{\partial t}\hat{\Psi}_i(\mathbf{x},t) = [\hat{\Psi}_i,\hat{H}]\tag{1.62}$$

in which the field operators must be replaced by the classical fields Ψ_i. We saw in the previous sections that, at low temperatures, binary collisions are characterized only by the scattering length, independently on the details of the interatomic potential. For this reason we can replace $V_{ij}(\mathbf{x}-\mathbf{x}')$ with the effective interaction potentials $g_{ij}\delta(\mathbf{x}-\mathbf{x}')$ defining

$$g_{ii} = \frac{4\pi\hbar^2 a_{ii}}{m_i}\tag{1.63}$$

$$g_{ij} = 2\pi\hbar^2 a_{ij}\left(\frac{m_i + m_j}{m_i m_j}\right). \tag{1.64}$$

Inserting the effective potentials in eq. (1.62) we can obtain the following set of coupled Gross-Pitaevskii equations (GPEs)

$$i\hbar\frac{\partial}{\partial t}\Psi_1(\mathbf{x},t) = \left(-\frac{\hbar^2\nabla^2}{2m_1} + V_1^{ext}(\mathbf{x}) + g_{11}|\Psi_1(\mathbf{x},t)|^2 + g_{12}|\Psi_2(\mathbf{x},t)|^2\right)\Psi_1(\mathbf{x},t)$$

$$i\hbar\frac{\partial}{\partial t}\Psi_2(\mathbf{x},t) = \left(-\frac{\hbar^2\nabla^2}{2m_2} + V_2^{ext}(\mathbf{x}) + g_{21}|\Psi_1(\mathbf{x},t)|^2 + g_{22}|\Psi_2(\mathbf{x},t)|^2\right)\Psi_2(\mathbf{x},t) \tag{1.65}$$

that can be used for the description of the macroscopic behaviour of two interacting Bose-Einstein condensates (BECs).

The ground state of the system can be found solving the Lagrange multipliers problem of minimizing the energy functional

$$\mathcal{E} = \int d^3x \sum_{i=1}^{2}\left[\frac{\hbar^2}{2m_i}|\nabla\Psi_i|^2 + V_i^{ext}(\mathbf{x})|\Psi_i|^2 + \sum_{j=1}^{2}\frac{g_{ij}}{2^{\delta_{ij}}}\Psi_i^*\Psi_j^*\Psi_i\Psi_j\right] \tag{1.66}$$

with the condition imposed by the normalization. This leads to the following set of coupled stationary GPEs:

$$\left(-\frac{\hbar^2\nabla^2}{2m_1} + V_1^{ext}(\mathbf{x}) + g_{11}|\Psi_1(\mathbf{x},t)|^2 + g_{12}|\Psi_2(\mathbf{x},t)|^2\right)\Psi_1(\mathbf{x},t) = \mu_1\Psi_1(\mathbf{x},t)$$

$$\left(-\frac{\hbar^2\nabla^2}{2m_2} + V_2^{ext}(\mathbf{x}) + g_{21}|\Psi_1(\mathbf{x},t)|^2 + g_{22}|\Psi_2(\mathbf{x},t)|^2\right)\Psi_2(\mathbf{x},t) = \mu_2\Psi_2(\mathbf{x},t), \tag{1.67}$$

the Lagrange multipliers μ_i are called chemical potentials. The equations described above are used for the numerical simulations presented in chapter 3 and in chapter 4.

Chapter 2

Experimental Apparatus

In this chapter I will give a brief description of the experimental apparatus used to perform the experiments described in chapter 3 and 4. Each section of the apparatus is presented following the typical experimental sequence: in two separated chambers the ^{87}Rb and ^{41}K atoms are collected from room temperature vapours and pre-cooled by means of a 2D-MOT scheme. The cold atoms are then pushed inside the main chamber where the two resulting atomic jets are used to load a mixed-species 3D-MOT. The atoms from the MOT are then further cooled, projected in the $|2,2\rangle$ state and transferred into the magnetic millimetric trap (millitrap). Here the Rb atoms are cooled down by means of the evaporative cooling technique allowing also the sympathetic cooling of the K atoms. At the temperature of ~ 1 μK the evaporation is stopped and the atoms are loaded in a crossed dipole trap where they are transferred in the $|1,1\rangle$ state. A uniform magnetic field is then applied on the atoms to tune the interspecies scattering length. At the end of the experimental sequence the atoms are observed by means of destructive absorption imaging. Each run lasts approximately 1 minute.

2.1   Laser Sources and Vacuum Chambers

Our experimental apparatus has been built up on two different optical tables. One of them is devoted to the generation and to the preparation of the different laser frequencies that are needed for the experiments while, on the other, is placed the vacuum apparatus. This set-up is designed to isolate the laser sources from vibrations and the atoms from stray light. The laser light is delivered across tables by means of several optical fibers.

Laser Sources

The most efficient and the most widely used cooling scheme for alkali atoms requires the use of two different laser frequencies for each atomic species. Both of them operate on the D_2 atomic transition. A first frequency, called *cooler*, acts on the $|^2S_{1/2}, F = 2\rangle \rightarrow |^2P_{3/2}, F' = 3\rangle$ transition while the second, called *repumper*, acts on the $|^2S_{1/2}, F = 1\rangle \rightarrow |^2P_{3/2}, F' = 2\rangle$ transition (see Fig. 2.1). The repumper light is needed to close the cooling transition, since, with the latter alone, some optical pumping in the $|^2S_{1/2}, F = 1\rangle$ state cannot be avoided. Without the repumper light, atoms in this state would be lost in the cooling process, reducing the cooling efficiency.

The above scheme works well for ^{87}Rb, once the detunings are suitably adjusted, but needs to be revisited in the case of ^{41}K. Indeed, for this species, the hyperfine structure of the excited level is small compared to the natural linewidth, as shown in Fig. 2.1, hence, it is not possible to consider the levels as isolated, even in presence of an auxiliary repumping beam. Moreover, the dynamics of the internal degrees of freedom of the atoms involves all the hyperfine components of the excited state and therefore the force is due to both the lasers from the $|^2S_{1/2}, F = 1\rangle$ and $|^2S_{1/2}, F = 2\rangle$ states. It has been demonstrated [16] that, to reach the Doppler temperature in a K sample, a careful balance of the two intensities and detunings is required. However, for this atomic species, no easy mechanism exists to reach the sub-Doppler regime. This has been the major obstacle for the realisation of a K BEC [17].

Since for ^{87}Rb the leakage to the $|^2S_{1/2}, F = 1\rangle$ state is small only a small intensity of repumping light is needed. Conversely, for ^{41}K, optical pumping to the $|^2S_{1/2}, F = 1\rangle$ level is strong and the light intensity of the repumper must be at the same level as the cooler. For a matter of convenience, in the following, the distinction between cooler and repumper light will be kept also for ^{41}K, indicating with cooler (repumper) the light with the lower (higher) frequency.

In our apparatus, all the light is provided by semiconductor lasers sources, as explained in the following.

Rubidium

As we can see in Fig. 2.1, the frequency difference between cooler and repumper for ^{87}Rb is about 6.8 GHz so it is convenient to use two different laser diodes for the two colours. For the cooler light we use a Sharp GH0781JA2C laser diode (maximum output power 120 mW) mounted in an extended cavity in Littrow configuration.
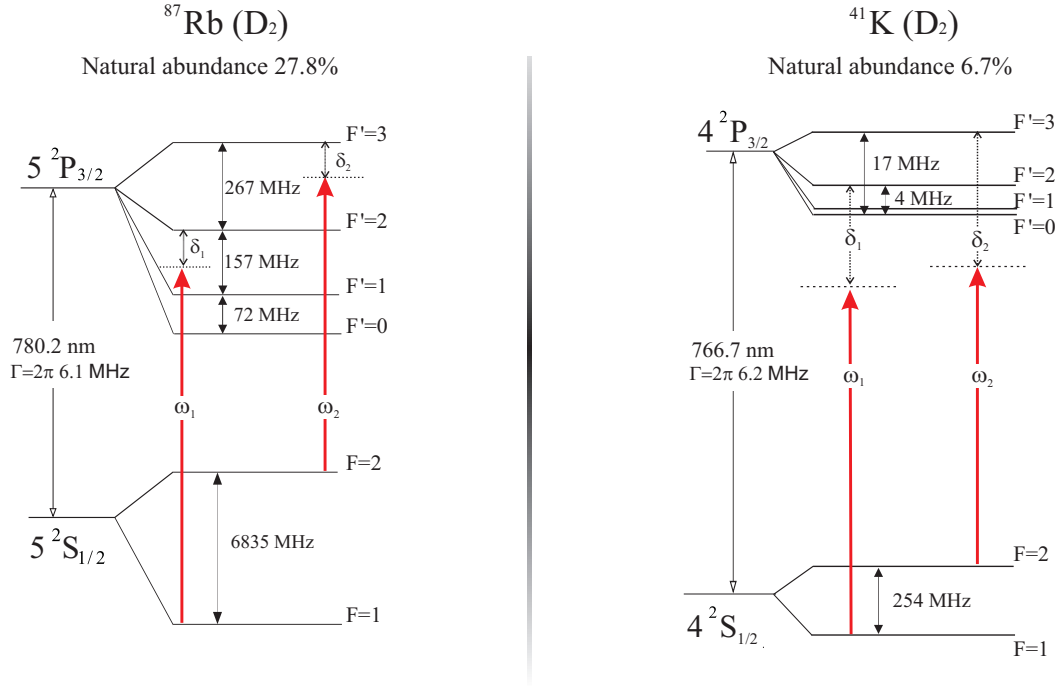
Figure 2.1: Level scheme for the D_2 transition for ^{87}Rb and ^{41}K. With ω_1 (δ_1) and ω_2 (δ_2) are indicated the repumper and cooler light frequencies (detunings) respectively. For every step of the experimental sequence the detunings are suitably arranged by means of acousto-optic modulators.

The cooler light is then amplified with a commercial tapered amplifier (Toptica DL-100), which provides about 600 mW as output power. As explained above for the repumping light a lower power is sufficient; this is given by a Sanyo DL7140-201 laser diode (maximum output power 70 mW) mounted again in Littrow configuration. Each laser is offset locked to a chosen line in the saturated absorption spectrum obtained from a reference cell by means of a modulation transfer spectroscopy scheme [18].

Potassium

As explained above, for the cooling of the ^{41}K atoms, the cooler and the repumper lights must have approximately the same power. To obtain this we employ a commercial grating-stabilized Tapered Amplifier (Toptica DLX-110) as repumper. This device is able to provide up to 600 mW of power. Its emission is offset locked on the saturated absorption spectrum of ^{39}K (since this is the most abundant isotope) around 767 nm, in the same way as ^{87}Rb. Since the frequency difference between

cooler and repumper is only 254 MHz, it is possible to obtain the cooler light by shifting the repumper with an acousto-optic modulator (AOM) without the need of a further locking scheme. For this purpose the output of the repumper is split in two beams; the less intense (~ 70 mW) is delivered at the AOM and then is amplified by a tapered amplifier chip EagleYard EYP-TPA-0765, that provides about 900 mW as output power.

Frequencies Management

The experimental procedure has several phases, each of them requiring a specific frequency of the laser light for the cooler and the repumper of both atomic species. To obtain the desired frequencies for each experimental step the light at the output of the four lasers described above is then split in several beams by means of a system of $\lambda/2$ wave plates and polarizing beam splitter cubes. In particular each species requires different frequencies for the pre-cooling, the loading of the MOT, the optical pumping and the detection. To independently control the frequency and the amplitude of each beam we feed each of them into a double pass AOM. After the double passage the beams are delivered into 7 polarization maintaining fibers, whose output is placed on the vacuum optical table. Detailed descriptions of the laser optical table can be found in [19] and [20].

The Vacuum Apparatus

Our vacuum system is mainly composed by three different chambers: two external identical pre-cooling chambers, one for each species, and a central "science" chamber, as depicted in Fig. 2.2.

The pre-cooling chambers are machined from a solid titanium block and rectangular BK7 windows are glued on it. The rear part of each chamber is connected to a vacuum ion pump (20 l/s per chamber), that maintains a pressure about 10^{-9} mbar, and to the dispensers; the latter release the atomic vapours once the current flows into them. Adjusting the current we can regulate the vapour pressure inside each external chamber.

The "heart" of the experiment is the main central chamber. There we mix the two species and we further cool the atomic samples down to few tens of nK. The main chamber consists of a cylindrical structure machined using non-magnetic stainless steel. The cylinder has an outer diameter of 180 mm and a height of 45 mm. This chamber is connected to a vacuum ion pump (55 l/s) that ensures a pressure of the
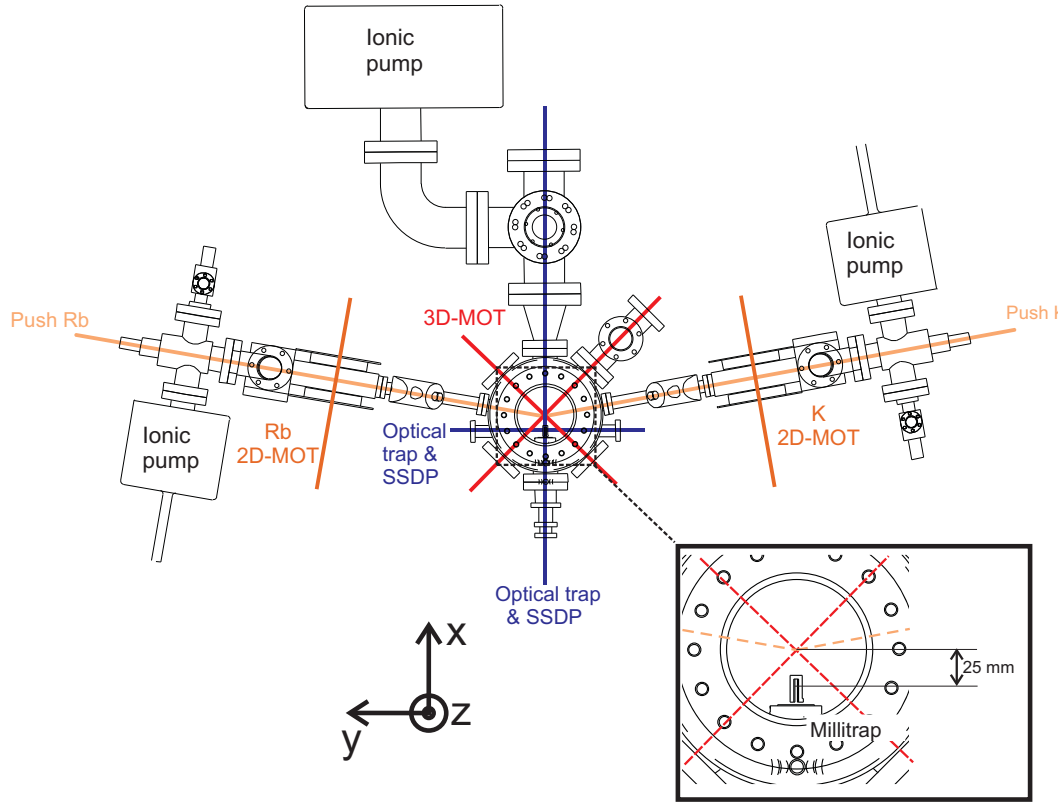
Figure 2.2: Scheme of the vacuum apparatus. The three chambers are visible, together with the magnetic millitrap (in the inset a magnification). The directions of the 2D- and 3D-MOT beams are also shown, as well as the directions of the optical trap beams and of the Species-Selective Dipole Potential beams. Here and for the following the main axes of the apparatus are those reported in figure.

order of 10^{-11} mbar.

Particular care has been used to maintain the biggest possible differential vacuum between each of the two pre-cooling cells and the main chamber. Therefore both connections are given by a 1cm long hole with a diameter of 1 mm followed by a 10cm long bellow. Moreover, inside each bellow, there are three graphite cylinders of increasing inner diameter (6, 8 and 10 mm respectively). The bellow is directly connected to the main chamber and relaxes the mechanical stress between the different sections of the vacuum setup.

One of the main features of our setup is given by the magnetic millitrap. This trap is placed directly inside the main chamber, as reported in Fig. 2.2. This innovative scheme gives higher frequencies with respect to the usual magnetic traps (hence a faster evaporation) without significantly affecting optical access to the trapping

region (as in the case of the μ-traps). A more detailed description is given later in section 2.3.

2.2   Magneto-Optical Trapping

The Rubidium and Potassium atoms that come from the dispensers inside the two external chambers are at room temperature and have a density n of the order of 10^8 cm^{-3}. Hence their phase space density (PSD), defined as $n\lambda_{dB}^3$, where λ_{dB} is the thermal de Broglie wavelength, is $\sim 10^{-19}$. Experiments with ultracold or degenerate atomic samples require a typical PSD of the order of 1. To reach this final value, as we will see, many steps are needed; the first of them exploits the combined action of magnetic fields and optical pressure to collect and cool the atoms.

2D-MOTs

The cooling of the atomic gases starts in the two external chambers. There the atoms are collected and pre-cooled starting from the vapour, and then pushed inside the main chamber. To do this we employ a 2D magneto-optical trap (2D-MOT) scheme. As depicted in Fig. 2.3, the four windows provide the optical access to the two counter-propagating beams in the transverse directions. An axially symmetrical magnetic field is also present, and is generated by the two rectangular coils placed outside the cell. Through a system of cylindrical lenses the beams assume an elliptic shape (axes ratio 3:1) in order to match the elongated shape of the chamber. Along the cell axis we shine another beam, called *push*, with σ^+ polarization, that is needed to push the trapped atoms through the 1 mm hole at the center of the output mirror, delivering them into the central chamber.

The 2D-MOT scheme cools the atoms in the transverse directions and selects a restricted class of atoms with low velocities in the longitudinal direction. Indeed, if an atom has a high longitudinal velocity, it cannot be trapped by the transverse beams since it goes across the entire cell in a too short time interval. Hence, along the cell axis, only the slower atoms are trapped and the push beam is needed to give them the necessary velocity to leave the chamber. The result is the generation of two cold atomic jets, one for each species, with an associated flux of the order of 10^9 atoms/s. More detailed analysis and descriptions can be found in [19], [20], [21].

One of the main features of our apparatus is that we can independently handle the two atomic jets that come out from the two external chambers. This gives

Figure 2.3: Pictorial representation of the 2D-MOT scheme described in the text. The scheme is applied to both atomic species.

us good control of the number of atoms loaded into the central 3D-MOT for each atomic species, allowing us to balance the atomic populations at will. By suitably regulating the length of the two push beam pulses (typically in the range 10-20 s).

3D-MOT

The mixing of the two species occurs in the central chamber by means of a 3D-MOT. The loading is provided by the two atomic jets that originate by the two 2D-MOTS. The magnetic field is originated by two circular coils with an outer diameter of 15 cm and an inner diameter of 4 cm in which flows a 4 A current. They are in thermal contact with water cooled aluminium heat sinks. The coils are mounted in the anti-Helmholtz configuration thus generating a quadrupole field that vanishes at the center of the chamber with a gradient of about 15 G/cm along the vertical direction. The current in the MOT coils is provided by an Agilent 6692A power supply (60 V, 110 A). The 3D-MOT scheme is completed by a set of 6 counter-propagating beams, two for each direction, that intercept each other in the center of the main chamber, as reported in Fig. 2.2. To compensate the stray magnetic fields a further set of three pairs of coils, one for each direction, is mounted on the apparatus.

Preparation of the Atoms for the Magnetic Trapping

After typically 20 s the 2D-MOT beams are switched off and the atomic jets are hence interrupted. At this point, as we will see later, it is necessary to reduce the size of the clouds. This is realized introducing a short phase (94 ms) of compressed MOT at the end of the loading of the 3D-MOT. We increase the magnetic gradient by a factor two (going from 4 to 10 A) and we shift the laser frequencies away from resonance. As a consequence we have the suppression of the photon re-scattering and the reduction of the size of the cloud by about a factor 2.

To compensate for the heating during the compression an optical molasses is applied for a few ms. The quadrupole field is switched off and the laser beams induce again the sub-Doppler cooling on the Rb atoms. For K atoms this cooling is not efficient hence the cloud simply expands in this phase. To avoid an excessive increase of the K cloud we keep the optical molasses duration below 5 ms.

At this stage the atoms populate all the sub-levels of the Zeeman manifolds of the $^2S_{1/2}$ level. Since, as we will see in the following, we want to transfer in the magnetic trap the atoms in the $|F = 2, m_F = 2\rangle$ state, it is necessary to apply an optical pumping towards this state. To do so we shine on the atoms a beam, σ^+ polarized, that contains the cooler and repumper light of both species tuned near the $|^2S_{1/2}, F = 2\rangle \rightarrow |^2P_{3/2}, F = 2\rangle$ and $|^2S_{1/2}, F = 1\rangle \rightarrow |^2P_{3/2}, F = 2\rangle$ transitions respectively. Once the optical molasses is over the optical pumping beam is shone along the vertical z axis and a weak uniform magnetic field is applied in this direction to define the right quantization axis. This phase lasts 320 μs.

2.3   The Magnetic Traps

With laser cooling techniques it is not possible to obtain temperatures below the recoil limit (for Rb only, the K sample cannot go below the Doppler limit), that is on the order of some hundreds nK. Moreover, in typical experimental conditions the lowest temperature achievable with this techniques is on the order of some tents of μK. To proceed further in the cooling of the atomic clouds and to reach the degenerate or the quasi-degenerate regime we have to make use of another technique: the evaporative cooling. This technique can be applied in magnetic or dipolar traps; in our experimental procedure both these traps are used, the first of them is the magnetic one.

The magnetic trapping is based on the interaction between an atom with a

permanent magnetic dipole moment μ and an inhomogeneous magnetic field $\mathbf{B}(\mathbf{r})$. The potential energy has a spatial dependence that can be written as

$$V(\mathbf{r}) = -\mu \cdot \mathbf{B}(\mathbf{r}). \tag{2.1}$$

If the time variation of $\mathbf{B}$ experienced by the atom occurs on a time scale τ, such that $\tau \gg \hbar/(\mu B)$, the direction of the atomic magnetic moment is always aligned with the local magnetic field, hence the interaction simplifies to:

$$V(\mathbf{r}) = g_F m_F \mu_B B(\mathbf{r}) \tag{2.2}$$

where m_F is the magnetic quantum number of the atomic state, g_F is the Landé factor and μ_B is the Bohr magneton. Depending on the sign of the product $m_F g_F$ a certain atomic state $|F, m_F\rangle$ can be classified as either low-field seeker ($m_F g_F > 0$) or high-field seeker ($m_F g_F < 0$). Since it is not possible to have an isolated magnetic field maximum in free space, only low-field seeker states can be magnetically trapped in a local minimum of the field. ^{87}Rb and ^{41}K share the same magnetic quantum numbers; the trappable states for these species in the $^2S_{1/2}$ level are $|F = 2, m_F = 2\rangle$, $|F = 2, m_F = 1\rangle$ (with $g_F = 1/2$) and $|F = 1, m_F = -1\rangle|$ (with $g_F = -1/2$). Among them we choose the $|F = 2, m_F = 2\rangle$ state, since for it the product $m_F g_F$ is largest ($g_F m_F \mu_B/h = 1.4$ MHz/G).

Magnetic Transfer

Once the optical pumping procedure is completed the atoms, now in the $|F = 2, m_F = 2\rangle$ state, must be compressed further and transported inside the millitrap, whose center, as shown in Fig. 2.2, is displaced of 25 mm on the x axis with respect to the center of the 3D-MOT. This procedure is executed by means of a quadrupole magnetic trap, provided by the same coils that originate the 3D-MOT field. The magnetic potential in this case is

$$V(\mathbf{r}) = g_F m_F \mu_B b\sqrt{x^2 + y^2 + 4z^2} \tag{2.3}$$

that vanishes in (0,0,0), the center of the trapping region.

As soon as the optical pumping beam is switched off, we raise the current inside the coils up to 20 A. In this way the spatial extension of the magnetic trap nicely matches the size of the two atomic clouds, this allows us to trap the atoms without inducing appreciable heating. At this point we have to compress the two clouds in order to make them pass into the small aperture of the millitrap. To do so we raise
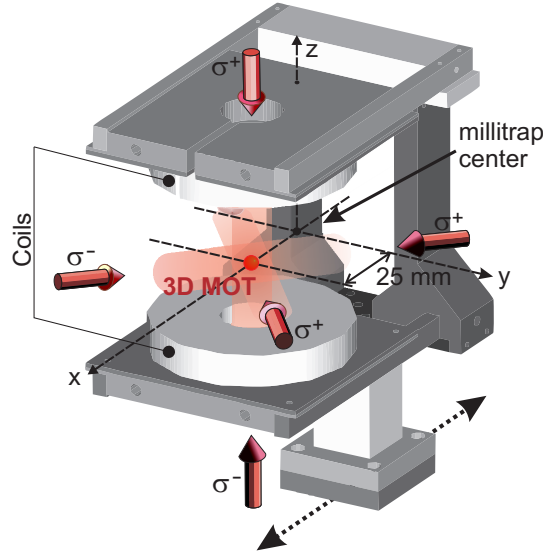
Figure 2.4: Pictorial representation of the translational stage in our apparatus. The two coils are glued to two heat sinks that are mounted on the translational stage. The latter moves the atoms on the x axis from the center of the 3D-MOT to the center of the millitrap.

again the current inside the two coils to 65 A, increasing the magnetic gradient to $\sim$130 G/cm. This compression raises the temperature of the atoms slightly below 1.1 mK and reduces the confinement length to some hundreds μm.

Once the atoms are trapped and compressed we need to move them to the center of the millitrap. The two coils, together with their heat sinks, are mounted on a translational stage that is is moved by a mechanical actuator driven by a brush-less motor (see Fig. 2.4). The translation stage moves the atoms to the center of the magnetic trap in 500 ms: the motion is obtained with a positive constant acceleration and a final constant deceleration. Limited losses and heating were observed in the atomic samples during the transport: the number of remaining atoms after a round trip is about 80%.

The Magnetic Millimetric Trap (Millitrap)

It is not possible to reach very low temperatures in a quadrupole magnetic trap. This is due to the presence of a zero in the field: an atom which stays a long time in the region of weak magnetic field around the minimum will have a finite probability to undergo a spin flip and therefore being repelled by the magnetic field gradient. Such a process is called Majorana spin-flip and it is the limiting factor

for the lifetime of a quadrupole trap at low temperatures. To avoid this effect it is necessary to trap the atoms in a magnetic field configuration that admits a non-zero local minimum. The most successful and widely used scheme is the so-called Ioffe-Pritchard configuration: two cylindrical coils with the same current create a Helmholtz field whose minimum is not zero. Four wires, perpendicular to the coils and in which flows the same current, create a gradient in the plane orthogonal to the trap axis (see Fig. 2.5). Through the multipolar expansion we can find that, around the minimum, the modulus of the field generated with such a configuration is

$$|B(\mathbf{r})| \simeq \sqrt{\left(B_0 + \frac{B''}{2}x^2\right)^2 + (B'\rho)^2} \tag{2.4}$$

where $\rho = \sqrt{y^2 + z^2}$, B' and B'' are the first and second terms of the multipoles expansion and B_0 is the bias field of the trap. All the three coefficients depend on the current that flows in the coils and in the wires. In the region where $z^2 \ll B_0/B''$ and $\rho^2 \ll (B_0/B')^2$ the trap field is harmonic:

$$|B(\mathbf{r})| \simeq B_0 + \frac{1}{2}B''x^2 + \frac{B'^2}{2B_0}\rho^2 \tag{2.5}$$

and we can define the harmonic frequencies as

$$\omega_x = \sqrt{\frac{g_F m_F \mu_B B''}{m}} \qquad \omega_\rho = \sqrt{\frac{g_F m_F \mu_B B'^2}{B_0 m}}, \tag{2.6}$$

with m the atomic mass.

In our apparatus we employ an innovative kind of trap that substantially mimics the Ioffe-Pritchard configuration described here above: the millitrap. The main structure of the millitrap is machined out of a pure oxygen-free copper tube in which four cut are open: the resulting shape is that of four bars connected by two pairs of semi-rings, as depicted in Fig. 2.5. The current flows in the bars and in the semi-rings as in the Ioffe-Pritchard configuration. The whole structure is then vacuum brazed on a ceramic chip on which a copper circular trace adheres. This circular trace, together with the two semi-rings on the other side of the millitrap, mimic the function of the two Helmholtz coils of the Ioffe-Pritchard trap. A 4 mm diameter hole in the center of the chip provides longitudinal optical access to the trapping region. The back side of the chip is in electrical contact with two copper tubes that are connected to the poles of an Agilent 6671 (0-8 V, 0-220 A) power supply.

As we can see from eqs. (2.6), the axial frequency depends only on the millitrap design and current (through B''), while the radial frequency can be varied changing
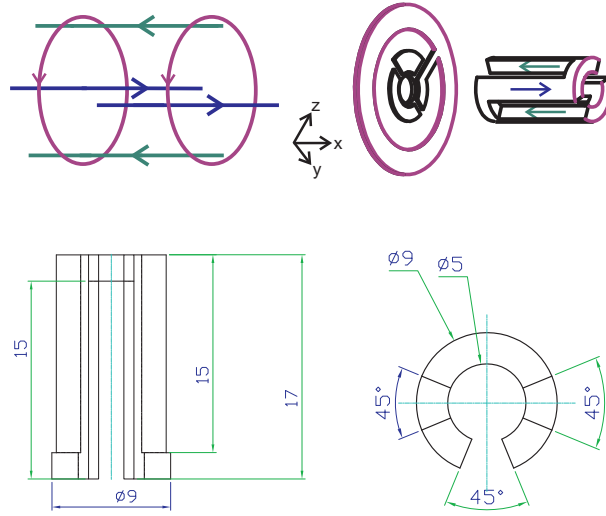
Figure 2.5: Upper row, pictorial scheme of a Ioffe-Pritchard trap configuration and 3D representation of the millitrap. In purple are indicated the Helmholtz coils while in blue (green) are indicated the forward (backward) bars. Bottom row: schematic drawings of the millitrap.

the bias field. For this reason an additional 6 loops square coil was inserted in series to the millitrap circuit to reduce B_0. The resulting harmonic frequencies, with a current of 70 A, for the ^{87}Rb sample are $\omega_x^{Rb} = 2\pi \times 16.5$ Hz and $\omega_\rho^{Rb} = 2\pi \times 204$ Hz. For the ^{41}K sample, since the potential is the same, the frequencies are a factor $\sqrt{m_{Rb}/m_K}$ larger than those of the ^{87}Rb, hence, $\omega_x^K = 2\pi \times 24$ Hz and $\omega_\rho^K = 2\pi \times 297$ Hz.

In our typical experimental procedure, once the translation stage has reached the final position, we raise the current inside the millitrap in about 150 ms to a peak current of 105 A. When the current is stabilized (~ 300 ms after turn on), the quadrupole field is turned off in about 300 ms leaving the atoms in the harmonic trap. Then we lower the current in the millitrap to the typical value of 70 A. At this stage we start the evaporative cooling process.

Evaporative and Sympathetic Cooling

When the transfer process is finished the ^{87}Rb and ^{41}K atoms are confined by the millitrap field only and, in absence of any light radiation, they interact by inter-species and intraspecies collisions. Since the two gases are very dilute the dominant processes are the elastic collisions between two atoms while the multi-particles collisions can be neglected. Elastic collisions ensure the kinetic energy redistribution and

thermal equilibrium between the atoms. The evaporative cooling technique, which has been proven to be the key technique to reach the degenerate regime, exploits this capability of thermalization between the atoms to cool them well below the degeneracy threshold.

The evaporative cooling consists in a continuous energy-selective removal of the hottest atoms from the magnetic trap volume and in the thermalization between the remaining atoms, to progressively reduce the temperature. An atom in the $|F, m_F\rangle$ state, trapped in the harmonic field (2.5), experiences a position-dependent Zeeman shift

$$\Delta E(\mathbf{r}) = g_F m_F \mu_B \left(B_0 + \frac{1}{2} B'' x^2 + \frac{B'^2}{2B_0} \rho^2 \right), \qquad (2.7)$$

that increases as soon as the distance from the center of the trap increases. Since the trapped atoms are distributed with the Maxwell-Boltzmann distribution function, those with higher velocities (hence higher energies) belong to the tails of this distribution, hence they spend most of their time where the Zeeman shift (2.7) is bigger. Exploiting this effect we can selectively choose a particular energy class since it is connected to a well defined spatial position in the trap. Using a certain radiation, that depends on the atomic species and on the hyperfine state, we can induce a spin-flip transition on the atoms driving them in a anti-trappable (or non-trappable) state and thus removing them from the trap. The frequency of the radiation determines the energy class to be expelled; by setting the right frequency we can cut the distribution tails only. A progressive reduction of the cutting frequency then leads to a cooling of the sample and to a reduction of the trapped atoms.

The entire process is based on the thermalization of the remaining atoms to a lower temperature. To ensure the thermalization we have to give the atoms the necessary time to collide. This means that the reduction of the cutting frequency has to be slower than the inverse of the elastic collision rate[1], $\tau = (\bar{n}\sigma\bar{v})^{-1}$ (being $\bar{n}$ the average density, σ the scattering cross section and $\bar{v}$ the mean velocity). For our atomic species, since $a_{RbRb} = 99a_0$ and $a_{KK} = 63a_0$, we can estimate that, at the beginning of the evaporative cooling process ($T \sim 1$ mK, $N_{Rb} \sim 10^8$ and $N_K \sim 10^6$), $\tau_{RbRb} \simeq 6 \times 10^{-2}$ s and $\tau_{KK} \simeq 10$ s[2]. The more we proceed in the evaporation the more these times are reduced, allowing a faster frequency reduction. This is due to the large density increase caused by the fact that the remaining atoms, having a lower mean energy, tend to sit at the center of the trap.

---

[1]The mean number of elastic collisions that are necessary to the thermalization is usually less than 5.

[2]This is a lower limit since at this temperature also p- and d-wave collision may occur.

Evaporative cooling is an efficient technique to reach very low temperatures and very high PSD if the initial number of atoms is sufficiently large and if τ_{el} is sufficiently small. This is not the case of ^{41}K since we are not able to load a big number of atoms in the millitrap and since the temperature of the sample at the beginning of the evaporation is above the Doppler limit. The most successful technique to cool this species has been proven to be the sympathetic cooling technique [22]. This is based on the continuous thermalization of K atoms with Rb atoms, that have the function of a thermal reservoir. The Rb sample can be considered a thermal reservoir only if its heat capacity $C_{Rb} = 3N_{Rb}k_B$ is much larger than the one of the K sample $C_K = 3N_K k_B$, simply implying that, during the whole cooling process, must be $N_K \ll N_{Rb}$. If this condition is satisfied, the temperature of the K sample follows the one of the Rb sample (see Fig. 2.6). Obviously also in this case the cutting frequency reduction for Rb must be slow enough to permit the thermalization between the two species. Since $a_{KRb} = 164a_0$, at the beginning of the evaporation $\tau_{KRb} \simeq 10^{-1}$ s; hence the KRb thermalization is faster than the KK thermalization ensuring a good efficiency in the sympathetic cooling process.

Usually the evaporative cooling is made inducing radio-frequency transitions between the trappable and the anti-trappable (or non-trappable) states in the same hyperfine manifold. In our experiment it is not convenient to use this approach since ^{87}Rb and ^{41}K share the same quantum numbers and the evaporation would act on both species. Hence, to selectively remove the Rb atoms, we drive the microwave transition between the $|2,2\rangle$ and $|1,1\rangle$ hyperfine levels. As we can see from Fig. 2.1 this transition, at ~ 6.8 GHz, is far away from any K transition thus the microwave cut leaves the K atoms unperturbed. The microwave radiation is given by a HP E8257D (dwell time 40 ms) synthesizer and, after an amplification to 40 dBm, it is fed into a horn antenna that maximises the power irradiated on the atoms.

We experimentally optimize the microwave ramp by maximizing the PSD of the Rb sample after every step. The resulting ramp is made by 5 linear steps, its total duration is $\sim$20 s and its shape is roughly exponential. The frequency span is about 100 MHz which means that the evaporation starts removing those atoms that have the temperature of 5 mK. As it is shown in Fig. 2.6, the K temperature follows the Rb temperature during the whole process and the degenerate regime is reached. Typically, at the end of the evaporation, we have $\sim 5 \times 10^4$ Rb condensed atoms and $\sim 4 \times 10^4$ K condensed atoms in the $|2,2\rangle$ state.

The determination of the temperature and of the number of atoms is made measuring the atomic density distribution by means of the absorption imaging technique.
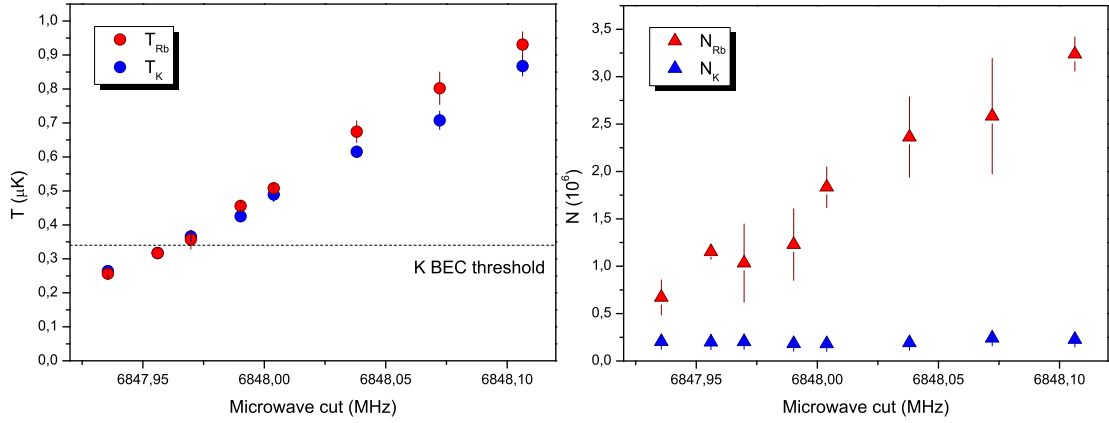
Figure 2.6: Evaporative and sympathetic cooling for ^{87}Rb and ^{41}K respectively. By slowly decreasing the microwave cut (from right to left) we cool the Rb sample expelling the hottest atoms from the trap. The K atoms continuously thermalize with the Rb atoms and, hence, they are also cooled down. The sympathetic cooling process is efficient since we ensure that, during the entire evaporation, the number of K atoms is always lower than the number of Rb atoms. Note that the microwave cut does not affect the K population.

At the end of the evaporation we switch off the current in the millitrap and we let the atoms expand ballistically. After a certain expansion time (typically 10-20 ms) we shine on the atoms a beam of resonant light (on the closed transition $|2,2\rangle \rightarrow |3,3\rangle$) and the absorption profile is recorded onto a CCD. In our experiment two separate probe beams exist: one comes along the $-z$ direction and the other along the x direction. The CCD camera is a Theta System SIS1-s285 (size of the sensor 1040 $\times$ 1392 pixels, each pixels is a square of 6.45 μm of side) that can operate the array in the so-called inter-layer mode: the first picture is stored in a dark region so that the array can be exposed again within less than 1 μs. We exploit this feature to image the two species almost simultaneously.

2.4   The Dipole Traps

To tune the interaction by means of Feshbach resonances it is necessary, as explained in chapter 1, to apply on the atoms a uniform magnetic field. When this field is present the magnetic trap can no longer trap the atoms, hence, another kind of trap is needed: the optical trap. This trap exploits the dipole force of one or two laser beams that acts on the atoms. Indeed, when a laser light is shined on an atom, the

electric field, at frequency ω, induces a dipolar moment on the atom that oscillates at the same frequency. The interaction potential between the field and the induced dipole is given by

$$U = -\frac{1}{2\epsilon_0 c}\Re(\alpha)I \tag{2.8}$$

where $\alpha(\omega)$ is the atomic polarizability, ϵ_0 the permittivity of free space, c the speed of light and I the laser intensity. For alkali atoms, in case of large detuning and negligible saturation, the intensity of the dipole potential is given by [23]

$$U(\mathbf{r}) = \frac{\pi c^2 \Gamma}{2}\left(\frac{2 + Pg_F m_F}{\Delta_{2,F}\omega_2^3} + \frac{1 - Pg_F m_F}{\Delta_{1,F}\omega_1^3}\right)I(\mathbf{r}), \tag{2.9}$$

with ω_1 and ω_2 the frequencies of the D_1 and D_2 atomic transition, $\Delta_{1,F}$ and $\Delta_{2,F}$ the detuning of the laser light from the same transitions and P that takes into account the laser polarization ($P = 0$ for linear polarizations and $P = \pm 1$ for $\sigma^\pm$ polarizations). If the term in brackets on the right hand side of eq. (2.9) is negative (positive) the laser light is said to be red (blue) detuned and the resulting potential has a minimum (maximum) where the laser intensity is maximum (minimum). Since the potential is proportional to the intensity of the light field, it is possible to engineer a proper optical potential for the atoms by varying the spatial intensity of a laser beam, localizing them in the field intensity maxima or minima in agreement with the sign of the detuning. The intensity of laser beams propagating along the x axis has a spatial Gaussian profile

$$I(\mathbf{r}) = \frac{2\mathcal{P}}{\pi w^2(x)}e^{-\frac{2\rho^2}{w^2(x)}}, \tag{2.10}$$

where $w(x) = w_0(1 + x/x_r^2)^{1/2}$ is the $1/e^2$ radius, w_0 the beam waist, $x_r = \pi w^2/\lambda$ the Rayleigh length (being λ the laser wavelength) and $\mathcal{P}$ the power of the laser. A red detuned Gaussian beam like this produces a cylindrically symmetric dipole trap. In the center of the trap the atoms are subjected to a harmonic potential with trapping frequencies $\omega_\rho = \sqrt{4U(\mathbf{0})/mw_0^2}$ and $\omega_x = \sqrt{2U(\mathbf{0})/mx_r^2}$.

Another important quantity, that must be kept into account for dipole traps, is the photon scattering rate defined as

$$\Gamma_{sc}(\mathbf{r}) = \frac{\pi c^2 \Gamma}{2\hbar}\left(\frac{2 + Pg_F m_F}{\Delta_{2,F}^2\omega_2^3} + \frac{1 - Pg_F m_F}{\Delta_{1,F}^2\omega_1^3}\right)I(\mathbf{r}), \tag{2.11}$$

that takes into account the atomic absorption and the successive emission of photons. These cycles of absorptions and emissions tend to heat up the sample, hence, the

wavelength of the optical trap must be chosen in such a way that the potential (2.9) is sufficiently strong to trap the atoms while the photon scattering rate (2.11) is the lower possible. The easiest way to fulfil these requirements is to choose a laser light that is far detuned from both the D_1 and D_2 transitions. Indeed, since $U \propto \Delta^{-1}$ and $\Gamma_{sc} \propto \Delta^{-2}$, the scattering rate diminishes much faster than the dipole potential as the detuning increases.

The Crossed Optical Trap

In order to trap both ^{87}Rb and ^{41}K by means of an optical potential we use a 1064 nm light provided by a commercial IPG YLR-20-1064-LP-SF fiber laser device capable of delivering up to 20 W with a linewidth of about 100 kHz. This wavelength has been chosen since it is far detuned from the D_1 and D_2 transition of both species, thus eqs. (2.9) and (2.11) are valid and the photon scattering rate is strongly reduced. The dipolar potential produced by the 1064 nm light is $\sim$10% larger for Rb than for K, according to eq. (2.9).

An optical trap scheme that provides a good control on the experimental parameters, e. g. trap depth or aspect ratio, can be realized crossing two beams with orthogonal polarization and equal waist under an angle of about 90 degrees. The result is a trap with nearly isotropic trapping volume and tight confinement in all directions.

In our experiment, to independently control the power and the frequency of the two crossing beams, we built up the optical scheme depicted in Fig. 2.7. The axial beam, that propagates along the x direction, has a frequency that is $\sim$ +110 MHz shifted (this corresponds to the +1 order of the AOM) with respect to the source light and has a waist of 110 μm at the center of the millitrap. The radial beam, that instead propagates along the $-y$ direction, has the same waist but its frequency is $\sim$ -110 MHz shifted (-1 order of the AOM) with respect to the source light. Hence the two beams are $\sim$220 MHz detuned the one to the other and, moreover, they are linearly polarized along orthogonal directions, thus preventing possible interference phenomena.

The above scheme has been used in all the experiments presented in chapter 3 while, for the experiments in chapter 4, we employ a slightly different scheme. Indeed, in this case, we deliver the two beams into two high-power polarization-maintaining fibers. This scheme allows us to conspicuously shorten the optical path, thus reducing the vibrations-induced noise, and to have on the atoms two perfect
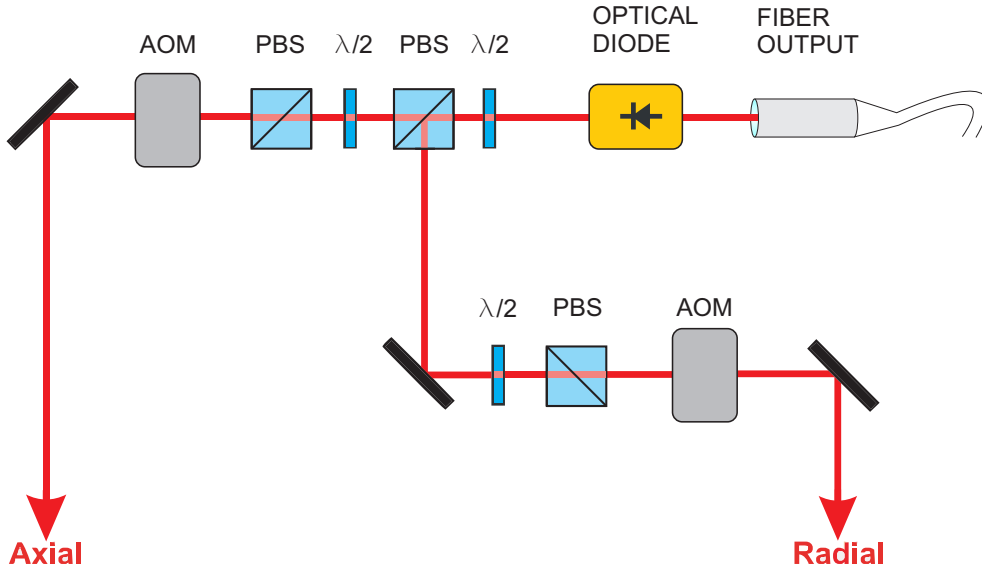
Figure 2.7: Scheme of the optical setup for the crossed dipole trap.

Gaussian beams with 80 μm waist. In both schemes the power of the two beams is stabilized with a feedback loop on the AOMs driven by the photodiode signal produced with a sampling of each beam.

To load the atoms in the crossed dipole trap we stop the evaporation at ~ 1 μK and we ramp down the current of the millitrap in 200 ms with an exponential ramp. Simultaneously we exponentially ramp up the power of the two dipole trap beams in order to maintain the trapping frequencies approximately constant along the whole transfer procedure (efficiency $\sim$80%). We have chosen to transfer the atoms at this temperature because, as we will see in the following, we need to transfer the atoms in the $|1, 1\rangle$ state and the hyperfine transfer procedure heats up the samples by $\sim$100 nK. This heating is just 10% for thermal clouds at 1 μK but can be more than 100% for degenerate clouds, implying a big drop in the PSD. Once the hyperfine transfer is completed the atoms can be further cooled down performing the evaporative cooling in the optical trap. In this case, to image the atomic samples, we abruptly switch off the two laser beams and we let the clouds expand. Just 400 μs before the probe beam is shined on the atoms we pump them again in the $|2, 2\rangle$ state with a 300 μs pulse of repumper light, thus they can produce the absorption profile on the imaging beam.

Adiabatic Hyperfine Transfer

We will see in chapter 3 that several heteronuclear Feshbach resonances are predicted for ^{87}Rb and ^{41}K once both species are in their absolute ground state $|F = 1, m_F = 1\rangle$. As explained in the previous sections, in our experimental procedure we trap and cool the atoms in the $|2, 2\rangle$ state and we cannot do the same for the $|1, 1\rangle$ state since the corresponding Landé factor is $-1/2$ and it cannot be magnetically trapped. Hence, once the atoms are loaded in the optical trap, we need to transfer them in the desired state.

As soon as the field of the millitrap is extinguished we raise up the current in the big squared coil (bias coil) depicted in Fig. 2.8. In such a way we generate a field that is orientated along the x axis at the center of the optical trap, providing a quantization axis for the trapped atoms. This field induces a well defined Zeeman shift between the $|2, 2\rangle$ and $|1, 1\rangle$ states. In order to adiabatically transfer the atoms in their ground state we exploit this Zeeman shift to induce the spin-flip transition. To avoid spin-flip collisions between atoms of different species, that would deplete the transfer efficiency, we need to transfer first the Rb atoms, whose hyperfine splitting is 6.835 GHz, much larger than the K one, 254 MHz (see Fig. 2.1).

Our experimental procedure is the following: we linearly ramp up the current in the bias coil in 40 ms thus producing a ~ 7.9 G field. Then, from the horn antenna, we send on the atoms a 6851 MHz radiation, carefully tuned on the $|2, 2\rangle \rightarrow |1, 1\rangle$ Rb transition at this field. Immediately after the microwave is switched on we linearly ramp up the bias field of 0.17 G in 100 ms. This is made to avoid Rabi oscillations between the two levels, to minimize the effects of the field fluctuations and to take into account the spatial extension of the atomic cloud. The overall efficiency of the process is $\sim$90%, the remaining atoms in the $|2, 2\rangle$ state are then blasted away with a light pulse resonant on the $|2, 2\rangle \rightarrow |3, 3\rangle$ transition.

Once the Rb atoms are transferred we switch off the microwave radiation and, exploiting a small circular coil placed on the top of the vacuum chamber (see Fig. 2.8), we send on the atoms a 272.2 MHz radiation, tuned on the $|2, 2\rangle \rightarrow |1, 1\rangle$ K transition at $\sim$8 G. Also in this case we ramp up the bias field of 0.055 G in 50 ms, leading to a $\sim 90\%$ transfer efficiency.

At this point both species are in the desired state but the transfer process induces a $\sim$100 nK heating on the samples. To reach the degenerate or quasi-degenerate regimes we perform the evaporative cooling in the crossed optical trap. The evaporation is made decreasing the intensity of the beams with a typical exponential ramp that lasts 3 s. During the whole process a uniform magnetic field is applied on the
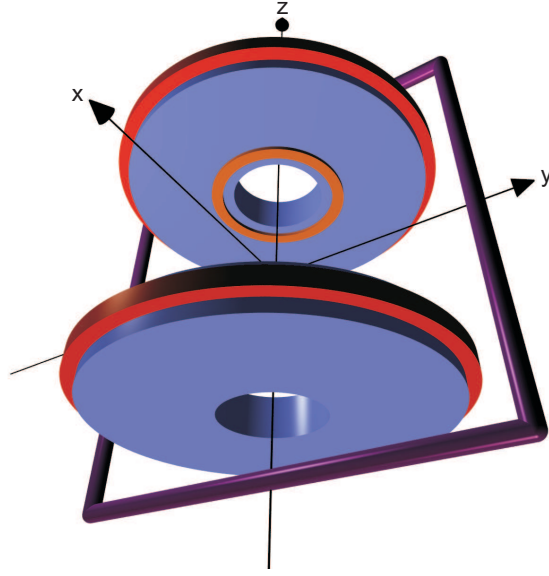
Figure 2.8: Pictorial scheme of the coil system in our apparatus. The two big blue cylinders represent the two MOT-Feshbach coils. The smaller red coils around them are used to compensate the stray fields during the MOT phase and to produce the optical pumping field. The big purple squared coil produces the bias field employed for the atomic hyperfine transfers. The small circular orange coil is the antenna that provide the radiation for the K spin-flip transfer.

atoms, as explained in the following, in order to tune the interspecies interactions.

The Species-Selective Dipole Potential

An interesting feature of the dipole potential is that, according to eq. (2.9), the same light produces different potential for different species. This is not the case of magnetic potential, at least for ^{87}Rb and ^{41}K that share the same quantum numbers. We can exploit this feature to selectively act on one species leaving the other unperturbed. Indeed, when the frequency of the laser beam is red detuned from the D_2 transition and blue detuned from the D_1 transition of a certain species such that the term in brackets on the right hand side of eq. (2.9) vanishes, this species is transparent at the laser light. Another species, with different D_1 and D_2 frequency, will instead experience the dipole potential produced by the same light. Hence, by suitably arrange the wavelength of the laser beam, we can produce a Species-Selective Dipole Potential (SSDP).

For ^{87}Rb we have $\lambda_1 = 794.9$ nm (in vacuum) and $\lambda_2 = 780.2$ nm while for ^{41}K
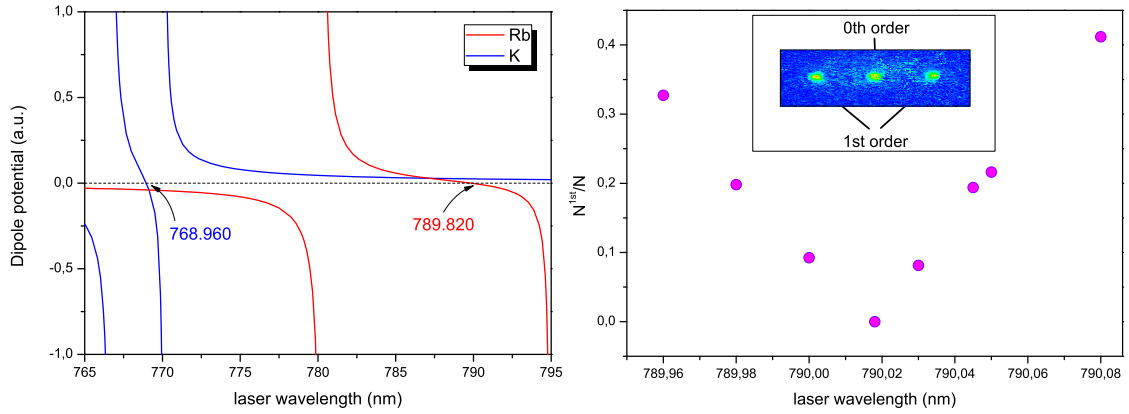
Figure 2.9: Determination of the Species-Selective Dipole potential wavelength. On the left is reported the behaviour of the dipole potential as a function of the laser wavelength according to eq. (2.9) for both species (linear polarization). On the right are reported the data for the experimental determination of the SSDP wavelength that is the wavelength at which the population of the first order of the Raman-Nath diffraction is minimum ($\simeq 0$). Data are taken after a 17 μs pulse of 180 mW. In the inset is shown a typical absorption image of the diffracted degenerate cloud.

$\lambda_1 = 770.1$ nm and $\lambda_2 = 766.7$ nm from which follows that, for a linearly polarized light, the Rb atoms experience no optical potential when $\lambda_{SSDP}^{Rb} = 789.8$ nm and the K atoms when $\lambda_{SSDP}^{K} = 768.9$ nm (see Fig. 2.9). For our experiments we have chosen to selectively act on the K sample, hence to use λ_{SSDP}^{Rb} mainly for two reasons: 1) the D_1 and D_2 separation is bigger for Rb than for K thus, in this case, the frequency of the SSDP beam is more detuned with respect to every atomic transition leading to a reduced photon scattering rate. 2) In the experiments presented in chapter 4 we need to use the unperturbed sample as a thermal reservoir and, in our case, it is easier for Rb to play this role.

The SSDP light is provided by a commercial Coherent MBR-110 Ti:Sapphire laser device (up to 3.5 W, linewidth 75 kHz) pumped by a Coherent Verdi V-18 laser (18 W). The beam at the output of the Ti:Sapphire laser is delivered into an AOM and then into a polarization-maintaining fiber, whose output is divided in two linearly polarized beams. One of them propagates along the x axis and is focused on the atoms with 90 μm waist; the other propagates along the $-y$ direction with a waist of 55 μm. In both cases the power is stabilized with a stabilization loop that acts on the AOM.

The experimental determination of the SSDP wavelength is made by minimizing

the efficiency of the Raman-Nath diffraction caused by a pulsed standing wave on the Rb condensate (being it in the optical or magnetic trap). To do this we retro-reflect the SSDP beam thus producing an optical lattice on the sample. The Raman-Nath technique allows us to determine the height of the optical lattice by measuring the populations of each order of the diffraction pattern as a function of the light pulse duration. Changing the length of the pulse the populations complete many oscillations, whose frequency is determined by the height of the optical lattice: the lower the frequency the lower the height. Hence, for a given pulse length, we change the laser wavelength in order to minimize the frequency of the oscillations of the populations. In particular, for very low heights of the lattice, only the 0th and 1st order population are involved and the SSDP wavelength is the one that minimize the simple ratio N^{1st}/N. The results are shown in Fig. 2.9.

In the experiments presented in chapter 4 we employ the SSDP in two different configuration: in the experiment of section 4.1 the atoms are trapped by the millitrap field and the SSDP beam is shone along the $-y$ direction while, in the experiments of section 4.2, the atoms are in the optical trap, subjected to the Feshbach field, and the SSDP beam propagates along the x direction. Due to the different setup the wavelength that minimize the Raman-Nath diffraction pattern is slightly different for the two cases: when the SSDP beam propagates along the $-y$ direction we obtain $\lambda_{SSDP} = 789.85(1)$ nm, while when it propagates along the x direction $\lambda_{SSDP} = 790.018(10)$ nm. This difference is due to the different alignment of the polarization axis with the field that, in the first case is directed along x and in the second case along z. In particular we find that, when the beam propagates along the $-y$ direction, it is not possible to perfectly align the polarization axis of the light with the field. Indeed, in this case, we measure that the ratio between the potential acting on K and the one acting on Rb is $\sim 0.08(1)$ while, when the beam propagates along the x direction, it is $0.0067(1)$.

2.5   The Feshbach Field

One of the most important parts of our experimental apparatus is represented by the two big coils that produce the MOT field and that provide the quadrupole trap for the transfer of the atoms in the millitrap. In addition we employ these two coils also for the generation of the Feshbach field needed to tune the interactions. This implies that their control circuit has to fulfil many different requirements.

The total resistance of the series of the two coils is 0.5 Ω and their total induc-

tance is 2 mH; this leads to an intrinsic time constant of 4 ms, but the one of the coils-power supply circuit is 50 ms. The power supply is remotely controlled via the GPIB interface and an analog current control. The time constant of 50 ms is appropriate when we ramp up the field in the MOT and in the quadrupole trap or when we slowly switch it off during the transfer in the millitrap, but it is too long in the case we want to abruptly switch off the field. For this purpose an IGBT transistor is inserted (see Fig. 2.10) to break the current flow when the magnetic field has to be turned off in sub-ms time intervals, as before the molasses phase or at the end of the experimental sequence. When the base-emitter voltage is driven to zero via a TTL driver, the circuit is suddenly opened, and the potential drop between source and drain terminals can reach very high values (exceeding some kV). A 75 volts AC varistor is connected between collector and emitter terminals, and has the double feature to protect the IGBT from the aperture extra-voltage and to set the fall time of the magnetic field to 1 ms. The current stability of the whole system is the nominal stability of the Agilent 6692A power supply (0.1%).

In the experimental sequence described up to now the two coils are always in the anti-Helmholtz configuration thus producing a quadrupole field. We have seen in chapter 1 that, to tune the interactions by means of Feshbach resonances, it is necessary to use a uniform magnetic field on the atoms. In our experiment this can be produced simply switching the configuration of the two coils from anti-Helmholtz to Helmholtz, exploiting a set of two electromechanical normally-open relais to revert the current flow in one of the two coils, as depicted in the scheme of Fig. 2.10. This switching operation can only take place when no current is flowing in the coils, and the commutation time of the relais is $\sim$200 ms.

Once the coils are in the Helmholtz configuration we can let the current flow into them producing a uniform magnetic field along the z direction. In this phase the current must be very stable, to reduce the noise on the field, and the time constant of the circuit must be quite low to allow fast field sweeps, that, e. g., can be useful for the adiabatic association of molecules across a Feshbach resonance. The Agilent 6692A power supply provides a very high current stability but, as we have seen at the beginning of this paragraph, allows only slow rise/fall times. Therefore we insert in parallel at the Agilent power supply a Kepco BOP 20-10M ($\pm$ 20 V $\pm$ 10 A) power supply that enables fast rise/fall times (a few μs). The current provided by this power supply must be stabilized. For this purpose we insert a LEM IT-150-S current transducer in the circuit that reads out the current. The voltage at the output of the LEM is then compared with the remote voltage control at the input
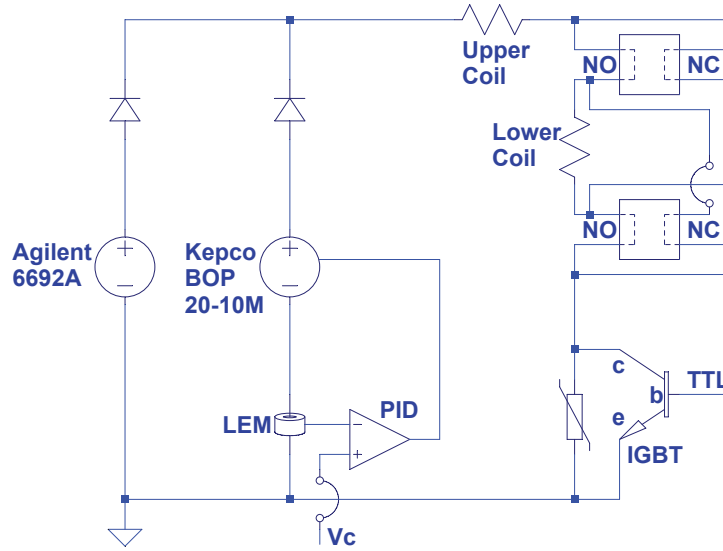
Figure 2.10: Schematic of the circuit employed for the control of the quadrupole and Feshbach fields.

stage of a PID controller. The feedback signal at the output of the PID stabilizes the power supply current. The stabilization loop reduces the rise/fall time of the circuit but it still enables fast field sweeps of 5 G/ms.

In our experimental sequence the current in the coils is switched off as soon as the atoms are in the millitrap field. Then, as described in the previous sections, the atoms are cooled down to 1 μK, loaded in the crossed dipole trap and adiabatically transferred in the $|1,1\rangle$ state. At this stages the two relais are commuted in the normally-closed position and the current in the coils is linearly ramped up in 20 ms by means of the stabilized Kepco power supply. Simultaneously the bias field (directed along the x axis) is ramped down to zero. Now the atoms are subjected to a uniform magnetic field along the vertical z direction and their scattering properties can be varied at will changing the magnetic field strength. Typically we initially set the magnetic field to a value for which the interspecies scattering length is low (a few hundreds a_0) in order to reduce three-body recombination losses. Then we start the evaporation in the dipole trap and, once the desired temperature is reached, we move the magnetic field to tune the interactions. The details of this procedure depends on the experiment we want to perform and are described in chapter 3 and 4.

To precisely calibrate the field we exploit the dependence of the Zeeman shift on

it. We can accurately calculate this shift solving exactly the Zeeman hamiltonian or, at least for the ground state hyperfine manifold, using the Breit-Rabi expression:

$$E_{|J=1/2,I=3/2,m_F\rangle} = -\frac{h\nu_{fs}}{8} - g_I\mu_B m_F B \pm \frac{h\nu_{fs}}{2}\sqrt{1 + \frac{4m_F x}{4} + x^2} \qquad (2.12)$$

where $x = (g_J - g_I)\mu_B B/(h\nu_{fs})$, $g_J = 2.002331$ the fine structure Landé factor, $g_I = -0.000995$ the nuclear g-factor and $h\nu_{hf}$ the energetic fine structure separation.

The experimental procedure is the following: we prepare a sample of Rb atoms in the $|2,2\rangle$ state and we load it in the optical trap. Then we switch on the Feshbach field to the desired value and we send on the atoms a microwave radiation that, approximately, corresponds to the $|2,2\rangle \rightarrow |1,1\rangle$ transition at this field. As a first step we make a 1 G sweep in the magnetic field in a few hundreds ms. If we do not detect losses (without the repumper pulse the atoms in the $|1,1\rangle$ state cannot be detected) we slightly change the radiation frequency and we repeat the procedure. Conversely, if an atom loss is detected, we progressively reduce the amplitude and the duration of the sweep to maximise the losses. With this method we can calibrate the field with an uncertainty of ± 5 mG.

Chapter 3

Two- and Three-Body Physics in Ultracold Bosonic Mixtures

^{41}K and ^{87}Rb in their absolute ground state are expected to exhibit many heteronuclear Feshbach resonances [24] providing the possibility to widely tune the interspecies scattering length from $-\infty$ to $+\infty$ by means of an external magnetic field. For this reason, as reported in the first section of this chapter, we perform an intense Feshbach spectroscopy in the [0,100] G range locating two s-wave resonances [25], two d-wave resonances [12] and two zero-crossings for the s-wave scattering length [25]. The precise knowledge of the scattering behaviour below 100 G allows us to produce the first double BEC with tunable interspecies interactions [25]. Moreover, in the second section, I will show that, exploiting the two s-wave Feshbach resonances, we are able to associate heteronuclear bosonic dimers starting from two ultracold atomic samples [26]. Finally, in the third section, I report on the first observation of Efimov physics in asymmetric systems, i. e., in systems composed by distinguishable particles, taking advantage of the ability to tune at will the scattering length [27].

3.1 ^{87}Rb-^{41}K Feshbach Spectroscopy

In the past years an intense research activity has been carried out on Feshbach resonances in K-Rb mixtures. In particular in Ref. [24] a model has been developed which, starting from measured resonances in the ^{40}K-^{87}Rb and ^{39}K-^{87}Rb mixtures, predicts the existence of several *heteronuclear* Feshbach resonances in the ^{41}K-^{87}Rb bosonic mixture in the absolute ground state $|1, 1\rangle$.

Our first goal has been to perform precise Feshbach spectroscopy in the $[0, 100]$

G range where two distinct s-wave resonances and two distinct zero crossings are predicted, as shown in Fig. 3.1. In Tab. 3.1 are reported the theoretical values for those two resonances. In principle, the determination of the positions of the resonances and of the zero crossings allows us to tune the scattering length in the $(-\infty, +\infty)$ range just by adjusting the external magnetic field.

	B_0 (G)	$|\Delta B|$ (G)	$a_{bg}(a_0)$	$|\mu_{res}|$ (μ_B)	η	assignment
low-field	39.4	37	284	1.65	0.0775	open-channel
high-field	78.92	1.2	284	1.59	2.48	closed-channel

Table 3.1: Theoretical values of the two Feshbach resonances below 100 G for the ^{41}K-^{87}Rb bosonic mixture in the $|1, 1\rangle$ state [24].

For ultracold atoms, Feshbach resonances can be detected as an enhancement of the three-body losses. Indeed, when three atoms are close enough, i.e., contained in a volume $\sim a^3$, it could happen that two of them bind into a molecule and the third carries away the released momentum and energy. More in detail, in the proximity of an heteronuclear Feshbach resonance, we can have

- Three body recombination: X+X+Y→X+XY. If we denote with ε the molecular binding energy, the molecule and the third atom will receive an energy $\varepsilon m_X/(2m_X + m_Y)$ and $\varepsilon(m_X + m_Y)/(2m_X + m_Y)$ respectively. Since usually ε is large compared to the trapping potential depth, both the molecule and the atom are expelled from the trap.

- Vibrational relaxation: X+(XY)* →X+XY. During the collision the shallow Feshbach molecule (XY)* releases energy and decays into the deeply bound molecule XY. The released kinetic energy is usually enough to free the atom and the molecule from the trap. This process occurs only on the side of positive scattering length, where highly excited Feshbach molecules (XY)* exist.

All those processes cause losses from the trap that can be modelled by the following rate equation

$$\dot{n}(t) = -\alpha n_X^2 n_Y(t), \tag{3.1}$$

where n_i are the atomic densities and α the event collision rate, i. e., the number of collisions events per unit of time and volume. Let us consider a couple of colliding atoms with a third atom located inside a sphere of radius $\sim a$ around the colliding pair. This location is characterized by a statistical weight $\sim na^3$ and the third atom
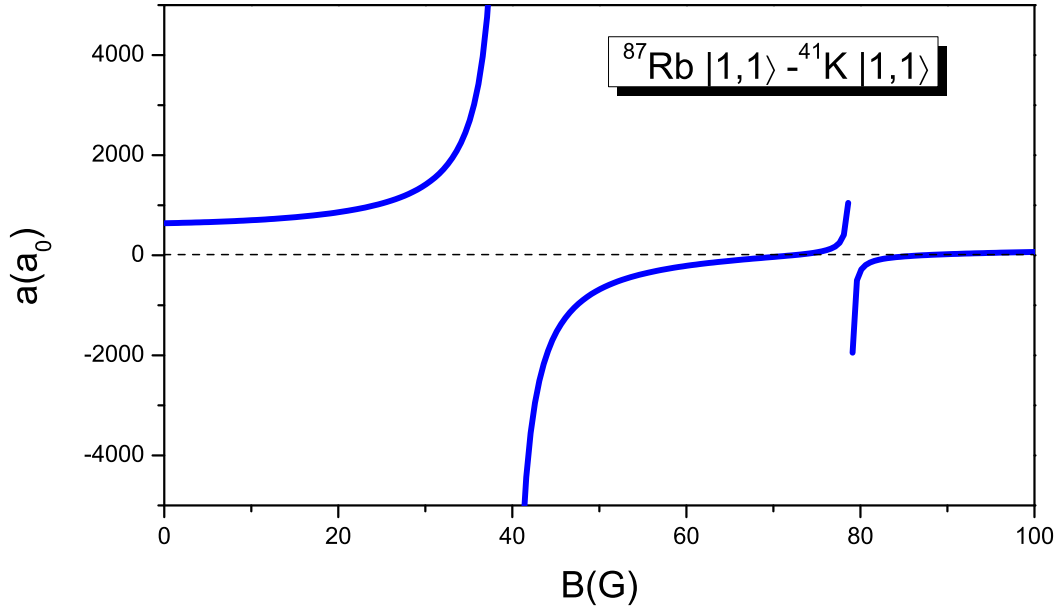
Figure 3.1: Theoretical behaviour of the interspecies scattering length as a function of the magnetic field for the ^{41}K-^{87}Rb mixture in the $|1,1\rangle$ state below 100 G [28].

can form a molecule with one of the colliding atoms with a probability of order unity. The number of such events per unit of time and volume is $\nu = \alpha n^3$ that can be estimated as $8\pi a^2 n^2 v(na^3)$. If we set $v \sim \hbar/(am)$ the velocity of the third atom relative to the center of mass of the molecule, we can immediately find that $\alpha \sim a^4$. This is a very important result that demonstrates that, as it was said before, approaching a Feshbach resonance the three-body losses are enhanced. A more quantitative explanation can be found in [29].

In a heteronuclear mixture there are four different α coefficients, two intraspecies and two interspecies. Since in our experiment we can tune the interspecies scattering length only the two interspecies contributions will vary with the magnetic field, namely α_{KRbRb} and α_{KKRb}. Moreover we have experimentally verified that no significant losses are observable in our system when single species samples are trapped in the optical trap with B fields below 100 G. Hence we can neglect the non-resonant intraspecies contributions and the resulting rate equations for the two densities are

$$\begin{aligned}
\dot{n}_K &= -2\alpha_{KKRb}n_K^2 n_{Rb} - \alpha_{KRbRb}n_K n_{Rb}^2 \\
\dot{n}_{Rb} &= -\alpha_{KKRb}n_K^2 n_{Rb} - 2\alpha_{KRbRb}n_K n_{Rb}^2
\end{aligned} \tag{3.2}$$

in the regions where the two atomic clouds overlap. From these equations we can

find that the total density $n = n_K + n_{Rb}$ obeys the following rate equation

$$\dot{n} = -3\alpha_{KKRb}n_K^2 n_{Rb} - 3\alpha_{KRbRb}n_K n_{Rb}^2. \tag{3.3}$$

Detection of s-wave Resonances

Our experimental procedure for the detection of Feshbach resonances is the following: we first prepare the mixture in the $|1,1\rangle + |1,1\rangle$ state in the optical trap and, in case, we perform an evaporation. Then we change the magnetic field in ~ 20 ms stabilizing it at the desired value and we hold the atoms for a fixed time interval. After this we switch off the trap and the magnetic field and we take the absorption images of the two expanding clouds recording the number of remaining atoms. As the main observable we choose the total atom number $N = N_K + N_{Rb}$ (that follows the same rate equation of n after integration over the volume) since it contains all the information regarding the two populations and since is the less affected by the fluctuations induced by the sympathetic cooling process. Two typical experimental line-shapes are shown in Fig. 3.2 where data are fitted with Gaussian functions. The position of the measured centres, $B_{0-lf} = (37.16 \pm 0.40)$ G and $B_{0-hf} = (78.42 \pm 0.015)$ G, nicely, but not perfectly, agree with the theoretical predictions.

The small discrepancy between theory and data is due to the fact that the positions of Feshbach resonances, measured with three-body losses, are affected by complicated dynamics that take place between atoms and molecules. Those dynamics are strongly temperature dependent, indeed, the center, the width and the shape of the experimental curves change with the temperature as shown in Fig. 3.3. This can be explained with a simple pictorial scheme: let us consider a three-body recombination process between three identical atoms (the same picture holds for distinguishable atoms) on the side of positive scattering length where, as it was explained before, the products of the collision are an atom with 2/3 of the binding energy and a shallow Feshbach molecule with 1/3 of the binding energy. If the depth of the optical trap (that fixes the temperature) is bigger than 2/3 of the binding energy, both the atom and the molecule are kept in the trap. Then, in a secondary collision the shallow molecule can collide with another trapped atom and decay due to vibrational relaxation. In this case the total number of atoms lost is *three*. If, vice versa, the trap depth is lower than 1/3 of the binding energy both the atom and the molecule are lost in the recombination process, thus leading to a loss of *three* atoms.

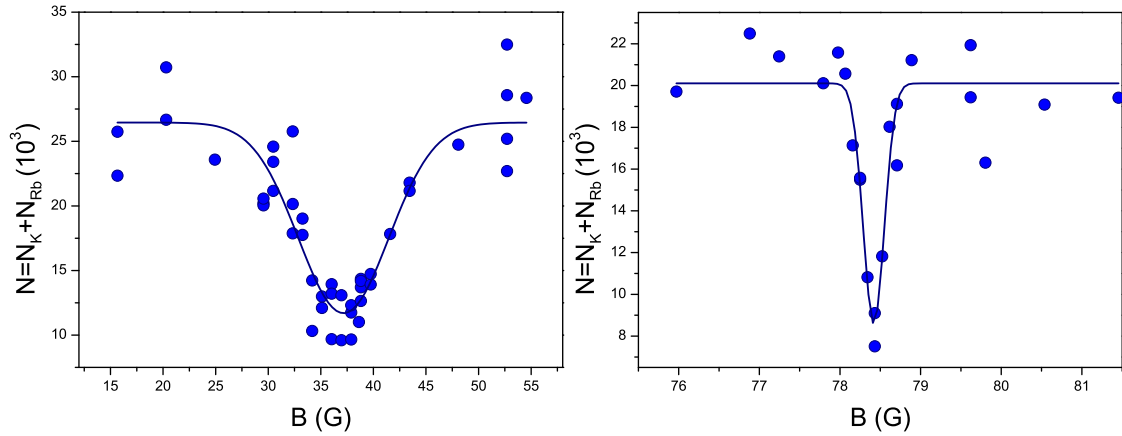A third possibility is when the trap depth is bigger than 1/3 but lower than 2/3

Figure 3.2: *s*-wave Feshbach resonances: total number of atoms $N = N_K + N_{Rb}$ as a function of the magnetic field. In the left panel is reported the three-body loss feature due to the broad low-field Feshbach resonance (T=150 nK, hold time=100 ms), in the right panel the one due to the narrow high field Feshbach resonance (T=200 nK, hold time=60 ms). The solid lines are Gaussian fits.

of the binding energy. In this case the atom is immediately lost while the molecule is lost after a secondary collision with a fourth atom that causes the vibrational relaxation, thus the number of atoms lost is *four*. Therefore we will have a maximum of losses that is moved on the side of positive scattering length with respect to the center of the Feshbach resonance; the higher the temperature, the bigger the displacement. Usually this displacement is hampered by the $\sim a^4$ dependence of the three-body losses that has its maximum at the center of the resonance. Anyway, if the resonance is broad enough, the temperature effect can have a dramatic impact on the experimental line-shape. For this reason the experimental data agree more nicely with theory for the high-field narrow resonance than for the low-field broad resonance. We will see in the next section a more accurate way to measure the positions of Feshbach resonances using the molecular binding energy.

Detection of *d*-wave Resonances

As it was explained in the first chapter broad *s*-wave resonance are the result of the spin-exchange coupling of the incoming *s*-wave atomic pair with $l' = 0$ molecules. Such processes are induced by the spherically symmetric exchange interaction V_{el} that conserves the angular momentum l, its projection m, the projection of the total hyperfine spin m_f and, consequently, the total angular momentum projection M_{tot}.
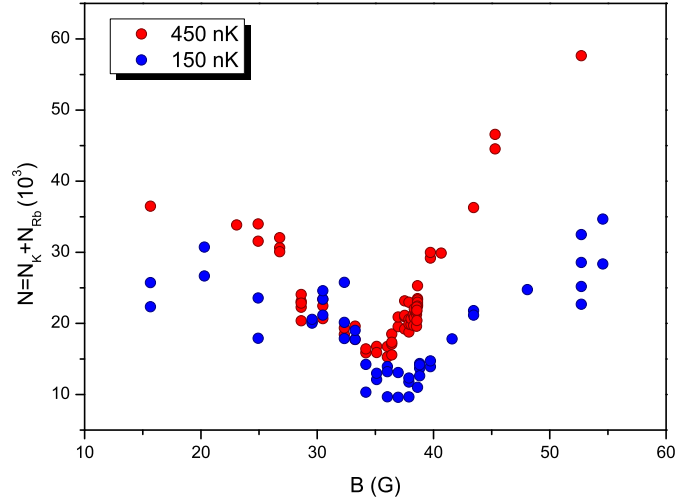
Figure 3.3: Low field Feshbach resonance: total number of atoms as a function of the magnetic field for two different temperatures. Increasing the temperature the center of the resonance is moved to the left (the side of positive scattering length).

Relativistic spin-spin and second order spin-orbit interactions are instead contained in the V_{SS} contribution that is anisotropic and that enables first-order coupling of l-wave atomic pairs with l' symmetry molecules, provided that the selection rule $0 \leq |l - l'| \leq 2$ (with the $l = 0 \rightarrow l' = 0$ collision forbidden) is satisfied. The rotational symmetry about the magnetic field implies, also in this case, the conservation of M_{tot}. Taking into account all the selection rules, the total interaction, in our experiment, couples the incoming atomic pair, characterized by $l = 0$ and $m_f = 2$, with molecular states which have $0 \leq l' \leq 2$ and $0 \leq m_f \leq 4$. Therefore colliding pairs with $l = 0$ may give raise to high partial wave Feshbach resonances. Conversely, collisions for incoming atoms with $l > 0$ tend to be suppressed at temperatures below the l-wave centrifugal barrier of the $\hbar^2 l(l+1)/(2\mu r^2) - C_6/r^6$ potential (for p-waves this barrier is ~ 170 μK).

High partial wave resonances can be detected, exactly as the s-wave resonances, looking at the behaviour of the three body losses as a function of the magnetic field. The challenge, in this case, is represented by the fact that these resonances are very narrow. Despite that, we detect two narrow features, one at (44.58 ± 0.05) G, with an HWHM of 0.1 G, and one at (47.97 ± 0.02) G, with an HWHM of 0.08 G, at the limit of our experimental resolution (see Fig. 3.4).
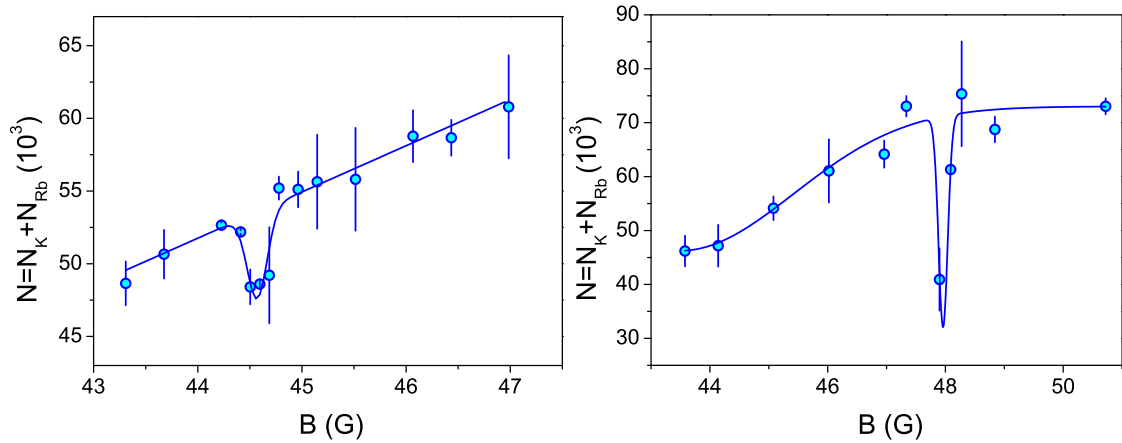
Figure 3.4: *d*-wave Feshbach resonances: total number of atoms $N = N_K + N_{Rb}$ as a function of the magnetic field. The solid lines are Gaussian fits on a broader pedestal, which is linear for the low-field resonance and Gaussian for the high-field resonance. The hold time is 100 ms for both data sets. $T = 400(10)$ $(450(10))$ nK for the low(high)-field resonance.

The assignment of these two narrow features can be made looking at the theoretical model of [24], whose predictions are reported in Fig. 3.5. In that figure the molecular levels for the lowest values of the angular momentum ($l' = 0, 1, 2$) are shown. Looking at the points where the molecular levels intercept the free-atom threshold we can label both features as *d*-wave resonances, whose quantum numbers are $(f, m_f, l) = (2,1,2)$ for the feature at 44.58 G and $(2,0,2)$ for the one at 47.97 G. The quantum number f is precisely defined only at $B=0$, anyway here we use it as an approximate quantum label also for $B \neq 0$. We will see in the next section that the positions of these two resonances, together with the binding energy measurements, can been used to improve the collisional model of [24].

Detection of Zero-Crossings

In order to complete the map of the scattering length behaviour below 100 G we must also measure the positions of the two zero crossings, that are the values of the magnetic field where the interspecies scattering length vanishes. The theoretical prediction for these values are $Z_{lf} = 72.18$ G and $Z_{hf} = 87.19$ G.

The positions of the zero-crossings can be measured looking at the efficiency of the sympathetic cooling process between the ^{87}Rb and the ^{41}K, that depends on the interspecies scattering length. To this end, once the mixture is prepared
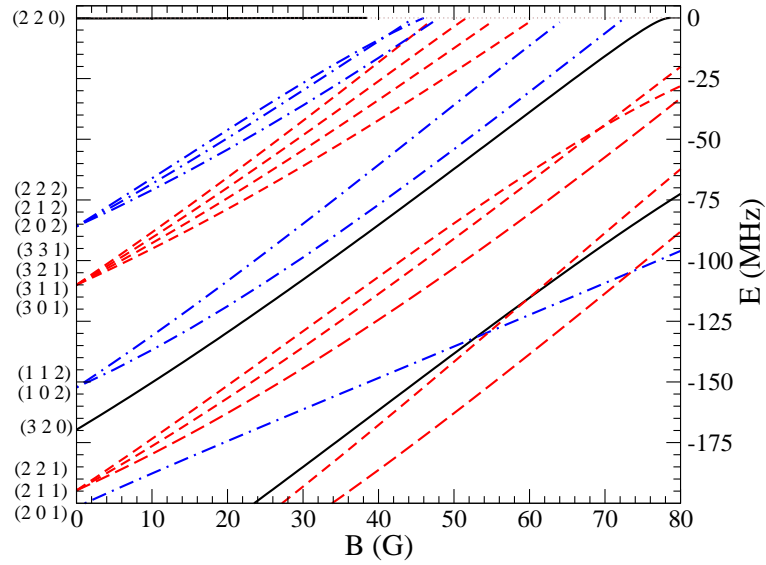
Figure 3.5: Molecular levels for the ^{41}K-^{87}Rb mixture in the [0,80] G range. Solid lines l'=0, dashed lines $l' = 1$, dash-dotted lines $l' = 2$. On the right side of the figure are reported the (f, m_f, l) quantum numbers associated to each level. All energies refer to the atomic threshold.

in the $|1, 1\rangle$ state, we set the magnetic field at the desired value and we apply an evaporation stage that reduces the optical trap power of 50% in 1.5 s. At the end of the evaporation we switch off both the trap and the B field and we take the absorption images of the two expanding clouds. Due to the gravitational sag and to the fact that the trap depth is 10% larger for ^{87}Rb than for ^{41}K, we evaporate mostly the ^{87}Rb and rely on the sympathetic cooling for ^{41}K. The positions of the zero crossings are expected to be those where the temperature of the ^{41}K sample is the highest.

During the evaporation the ^{41}K temperature decreases exponentially with a rate that is proportional to the interspecies elastic cross section. As it was explained in chapter 1, the cross section depends quadratically on the scattering length hence, the final temperature of the ^{41}K sample is a decreasing function of a_{12}: $T_K^{fin} = T_{eq} + \Delta T \exp(-\eta a_{12}^2)$. Here η is a parameter that takes into account the overlap of the two clouds and the thermalization time. As shown in Fig. 3.6 we fit our data with this simple model, where the dependence of a_{12} on the magnetic field B is taken from the theory. As a fit parameter, in addition to T_{eq}, ΔT and η, we introduce a global offset of the magnetic field values δB in order to verify the agreement between
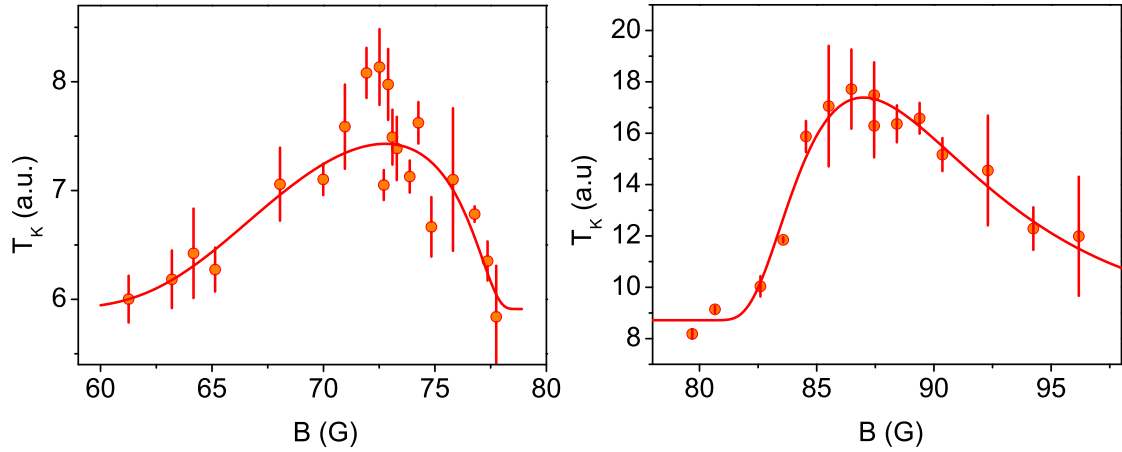
Figure 3.6: Zero crossings: ^{41}K temperatures after the sympathetic cooling as a function of the magnetic field. The solid lines are the fits with the simple model explained in the text.

our data and the theoretical predictions. Since the δB fit values are (0.59 ± 0.64) G for the low-field zero crossing and (-0.21 ± 0.32) G for the high-field zero crossing we can conclude that our measurement are in good agreement with the theoretical predictions.

Exploiting the two zero-crossings we can precisely tune the interspecies interactions around zero. Since the slope is 16.8 a_0/G and 8.9 a_0/G for the low-field and the high-field zero-crossing respectively, we can control a_{12} with a precision better than $1a_0$.

Double Species Bose-Einstein Condensate with Tunable Interspecies Interactions

The knowledge of the positions of both s-wave Feshbach resonances and both zero-crossings allows us to precisely tune the interspecies scattering length between Rb and K. In particular the region between the two zero crossings is especially interesting since, with increasing B field, the scattering length goes from 0 to $+\infty$ and from $-\infty$ to 0 again in quite a narrow range (see Fig. 3.1). Exploiting this feature we are able to produce a double-species condensate on both sides of the high-field resonance.

To achieve the double condensation, once the mixture is prepared in the $|1,1\rangle$ state, we set the B field value to 77.7 G, where the scattering length is weakly repulsive $a_{12} \simeq 250a_0$, and we lower the trap depth in 3 s. In order to reduce the rate of three body losses, in the last 500 ms of the ramp, when Bose-Einstein
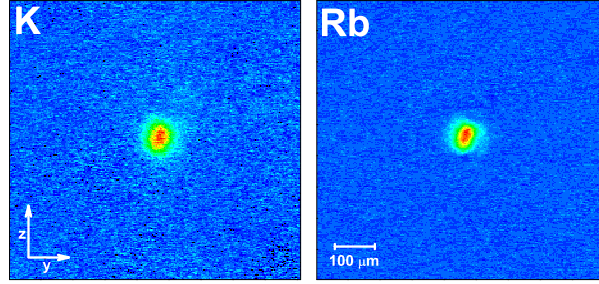
Figure 3.7: Horizontal absorption image of the ^{41}K-^{87}Rb double species condensate in the $|1,1\rangle$ state after 9 ms of expansion.

condensation starts to occur and the densities increase, the B field is brought to 76.8 G, where $a_{12} \simeq 150a_0$. With this scheme we are able to produce pure double species BECs with repulsive interactions with typically $9{\times}10^3$ atoms of ^{87}Rb and $5{\times}10^3$ atoms of ^{41}K (see Fig. 2BEC11).

We can also produce BECs on the right side of the high-field resonance, i.e., in the region where the interspecies scattering length is negative. To do this we adopt the same scheme as before but the evaporation is performed at B=80.7 G, where $a_{12} \simeq -185a_0$. In such a way we can produce the double condensate with attractive interspecies interactions with the same typical number of atoms.

The production of the double BEC on the side of negative scattering length can be achieved exploiting an important feature of our experimental setup: at the end of the evaporation the measured harmonic frequencies of the dipole trap in the vertical direction are $\omega_{Rb} = 84$ Hz and $\omega_K = 122$ Hz (in the other directions are $\omega_i/\sqrt{2}$ Hz). This, due to the differential gravity sag $g/(\omega_K^2 - \omega_{Rb}^2)$, force the centres of the two clouds to be 13 μm apart (see Fig. 3.8). Since there is no contact between the two clouds, all the mean-field dynamics induced by the interspecies interactions are avoided.

Interspecies mean-field dynamics are all those phenomena that arise from the non-linear term $g_{ij}|\Psi_j|^2$ of both eqs (1.65); among them there are the phase separation for large and positive a_{12}, and the collapse, that occurs for large and negative scattering length. Here large means that the condition $g_{12}^2 > |g_{11}g_{22}|$ is satisfied. The strong displacement completely washes away these effects and this is of special importance in the case of attractive scattering length, where the interactions-induced
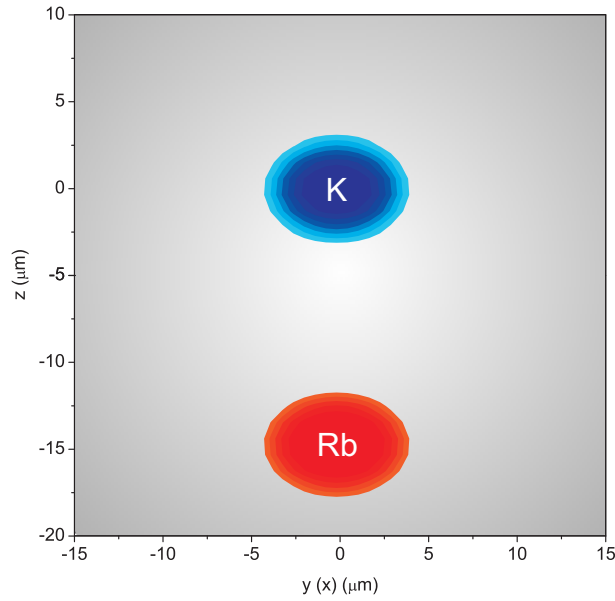
Figure 3.8: $x(y) = 0$ slice of the densities of the ground state of a double BEC with $9(4) \times 10^3$ atoms of ^{87}Rb(^{41}K) in a harmonic trap with $\omega_z = 84$ Hz and $\omega_{x,y} = 84/\sqrt{2}$ Hz for ^{87}Rb. The vertical sag is 13 μm. The ground state is obtained solving numerically eqs. (1.67).

collapse completely destroy the double condensate. Hence, by carefully balancing the number of atoms we arrange the BEC to first occur for ^{41}K; immediately afterwards the two clouds separate and also ^{87}Rb reaches the condensation. In case, the separation can be reduced recompressing the trap.

3.2 Association of Bosonic Ultracold Heteronuclear Molecules

As it was shown in section 1.2 Feshbach resonances arise from the resonant coupling of the energy of two colliding atoms with a molecular bound state. Moreover it has been experimentally demonstrated many times that Feshbach resonances can be used to convert a couple of colliding atoms into a dimer [6, 7] [27-43], . Among dimers, ultracold *heteronuclear* molecules are of special interest since they are characterized by the long-range interaction that arises from their permanent electric dipole moments. Many theoretical works have been done proposing such molecules as candidate qubits [47, 48] as well as the constituents of strongly correlated systems [49] or of the next generation of dipolar BECs [50].
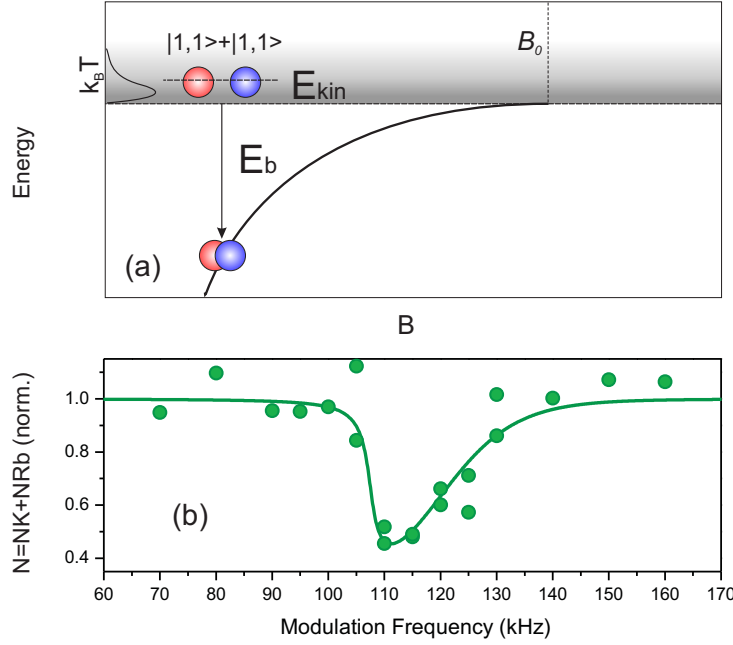
Figure 3.9: (a) Pictorial scheme of the molecular rf association. Two free atoms with relative kinetic energy E_{kin} are resonantly transferred to a molecular level by modulating the magnetic field. (b) Typical line shape for an association time of 30 ms, B=78.25 G. The solid line is a fit with the model described in the text

Starting from ultracold atoms, molecules have been created following two different approaches: photoassociation [43] and magnetoassociation [6, 44, 45]. Anyway, up to now, only a few experiments have reported the production of heteronuclear molecules; among them three groups have reported the creation of fermionic KRb molecules [37, 38, 39, 40], that cannot condense, and one group the association of bosonic ^{85}Rb-^{87}Rb molecules [41], that can have only a very small permanent dipole moment.

To produce bosonic dipolar molecules one can start from a Fermi-Fermi [42] or, as in our case, from a Bose-Bose heteronuclear atomic mixture. In principle, pure bosonic mixtures are preferable since they have the great advantage to allow high phase-space densities, provided that three-body losses can be neglected.

After having prepared both species in the $|1, 1\rangle$ state at the desired temperature, following [46], we add a resonant radio-frequency (rf) modulation to the external magnetic field, on the side of positive scattering length of both s-wave Feshbach resonances, that allows us to associate ^{41}K^{87}Rb bosonic molecules starting from the

ultracold mixture (see Fig. 3.9(a)). The rf modulation pulse has a typical length of 15-30 ms with a simple square envelope and a typical amplitude of $\sim$130 mG. Dimers are created when the modulation frequency f_m is close to the binding energy E_b/h of the Feshbach molecular level. The production of molecules is revealed by the reduction of the total number of atoms $N = N_K + N_{Rb}$ at the end of the rf pulse, as we scan the modulation frequency. A typical line shape is reported in Fig. 3.9(b). Starting from 4×10^4 atoms of ^{87}K and 3×10^4 atoms of ^{41}K we are able to associate up to 12×10^4 dimers at temperatures between 200 and 600 nK.

Even if we are not able to directly image the molecules, since their lifetime in the presence of unbound atoms is shortened by collisional relaxation, the rf association spectra provide a clear signature of molecule production and their analysis carries a large amount of information on the association dynamics. For such an analysis we have developed a simple theoretical model, that is presented in the following.

Analysis of the rf Association Spectra

Association spectra as the one shown in Fig 3.9(b) can be described by means of a simple theoretical model that considers an atom pair in the center-of-mass frame. Let us introduce the annihilation operators $\hat{a}, \hat{b}$ and $\hat{m}$ for atoms A, with momentum p, for atoms B, with momentum $-p$, and for molecules respectively. In the absence of coupling the time dependent hamiltonian is

$$\hat{H}_0 = \left(-E_b(B(t)) - i\frac{\hbar\gamma}{2}\right)\hat{m}^+\hat{m} + \frac{p^2}{2m_A}\hat{a}^+\hat{a} + \frac{p^2}{2m_B}\hat{b}^+\hat{b} \qquad (3.4)$$

where m_A and m_B are the two atomic masses and γ is the lifetime of the molecule. The time dependence of the binding energy is brought by the oscillating magnetic field $B(t) = B_{dc} + B_\omega \sin(\omega t)$, with $\omega = 2\pi f_m$.

The coupling between atoms and molecules is induced by the oscillating part of the magnetic field. Following [51], we can write the single-particle coupling as $\Omega(B(t)) = \Omega_0(B_{dc})\cos(\omega t)$ with $\Omega_0(B) = \omega B_\omega(\partial_{B'}\langle\psi_m(B)|\psi(B')\rangle)_{B=B'}$. The resulting rf coupling hamiltonian is

$$\hat{H}_{rf} = \hbar\Omega(t)(\hat{m}^+\hat{a}\hat{b} + \hat{m}\hat{a}^+\hat{b}^+). \qquad (3.5)$$

We can now write the Heisenberg equations

$$\frac{d}{dt}\langle\hat{\mathcal{O}}\rangle = \frac{i}{\hbar}\langle[\hat{H},\hat{\mathcal{O}}]\rangle \qquad (3.6)$$

for the three operators $\hat{a}, \hat{b}, \hat{m}$, obtaining the following rate equations for their expectation values

$$
\begin{aligned}
i\dot{m} &= \left(-\frac{E_b(t)}{\hbar} - i\frac{\gamma}{2}\right) m + \Omega_0 \cos(\omega t) ab \\
i\dot{a} &= \frac{p^2}{2\hbar m_A} a + \Omega_0 \cos(\omega t) b^* m \\
i\dot{b} &= \frac{p^2}{2\hbar m_B} b + \Omega_0 \cos(\omega t) a^* m
\end{aligned}
\tag{3.7}
$$

where the $\langle\rangle$ notation has been dropped. Note that if $\gamma = 0$ the quantity $2|m|^2 + |a|^2 + |b|^2$ is constant. This set of equation admits analytical solution once two approximations are introduced:

- Rotating wave approximation: we write the rate equations in terms of the slowly varying amplitudes $\alpha = a \exp(ip^2/(2\hbar m_A)t)$, $\beta = b \exp(ip^2/(2\hbar m_B)t)$ and $\mu = m \exp(-i(\omega - E_{kin}/\hbar)t)$; with $E_{kin} = p^2/2m_A + p^2/2m_B$. This implies neglecting all those terms $\propto \exp(i(E_{kin}/\hbar + \omega)t)$.

- Adiabatic approximation: since the molecular decay is fast the molecular amplitude μ follows the evolution dictated by the slower rf coupling, thus leading to $\dot{\mu} = 0$.

With these approximations we can find the following equations for the slowly varying amplitudes:

$$
\begin{aligned}
\mu &= -\frac{\Omega_0}{2(\delta - i\gamma/2)}\alpha\beta \\
\dot{\alpha} &= \frac{\Omega_0}{2}\beta^*\mu \\
\dot{\beta} &= \frac{\Omega_0}{2}\alpha^*\mu
\end{aligned}
\tag{3.8}
$$

with $\delta = \omega - E_b/\hbar - E_{kin}/\hbar$. Using eqs. (3.8) we can easily obtain the rate equations for the atomic populations $N_A = |a|^2$ and $N_B = |b|^2$:

$$
\begin{aligned}
\dot{N}_A &= \dot{a}a^* + c.c = -\frac{2\gamma\Omega_0}{4\delta^2 + \gamma^2}N_A N_B \\
\dot{N}_B &= \dot{b}b^* + c.c = -\frac{2\gamma\Omega_0}{4\delta^2 + \gamma^2}N_A N_B.
\end{aligned}
\tag{3.9}
$$

From these immediately follows that $N_- = N_A - N_B$ remains constant and that

$$
\partial_t(N_A + N_B) = \dot{N} = -\gamma_e(N^2 - N_-^2)
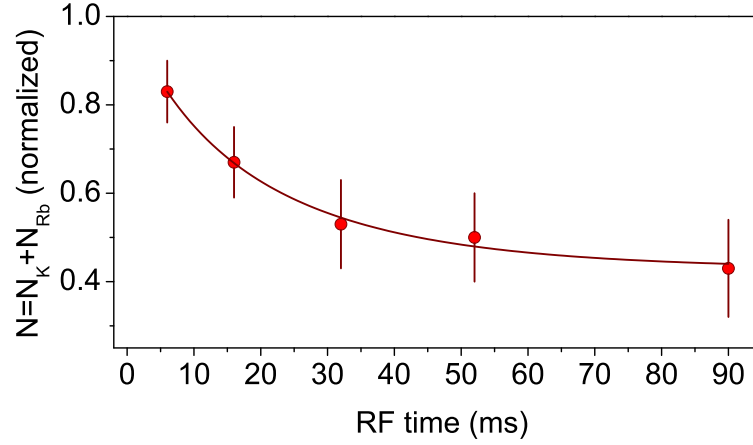\tag{3.10}
$$

Figure 3.10: Remaining atom number as a function of the rf pulse length. The solid line is a non-exponential fit made with eq. (3.13).

with

$$\gamma_e = \gamma \frac{\gamma \Omega_0}{2(4\delta^2 + \gamma^2)}. \tag{3.11}$$

The general solution of eq. (3.10) has the form

$$N(t) = N_- \frac{Ce^{2\gamma_e N_- t} + 1}{Ce^{2\gamma_e N_- t} - 1} \quad C = \frac{N(0) + N_-}{N(0) - N_-}, \tag{3.12}$$

which, in the $N_- = 0$ case reduces to

$$N(t) = \frac{N(0)}{1 + N(0)\gamma_e t} \tag{3.13}$$

that is the well-known solution of the rate equation $\dot{N} = -\gamma_e N^2$, that is used to describe losses due to two-body collisions. In our measurement we observe such a non-exponential decay, as shown in Fig. 3.10

The general solution (3.12) depends on the atomic kinetic energy E_{kin}, whose values are distributed over a range of the order of the temperature T. In order to fit our association spectra we need to take the thermal average of eq. (3.12) by convolving with the thermal distribution of kinetic energy $\sqrt{E_{kin}} \exp(-E_{kin}/k_B T)$. As reported in Fig. 3.9(b) and 3.11 our model well describes the dependence of the width on the temperature and the strong asymmetry of the association spectra. Both features are borrowed by the asymmetric Boltzmann distribution of the kinetic energies, whose width increases with the temperature. Indeed, the asymmetry of the association spectra was not observed in similar experiment with degenerate or
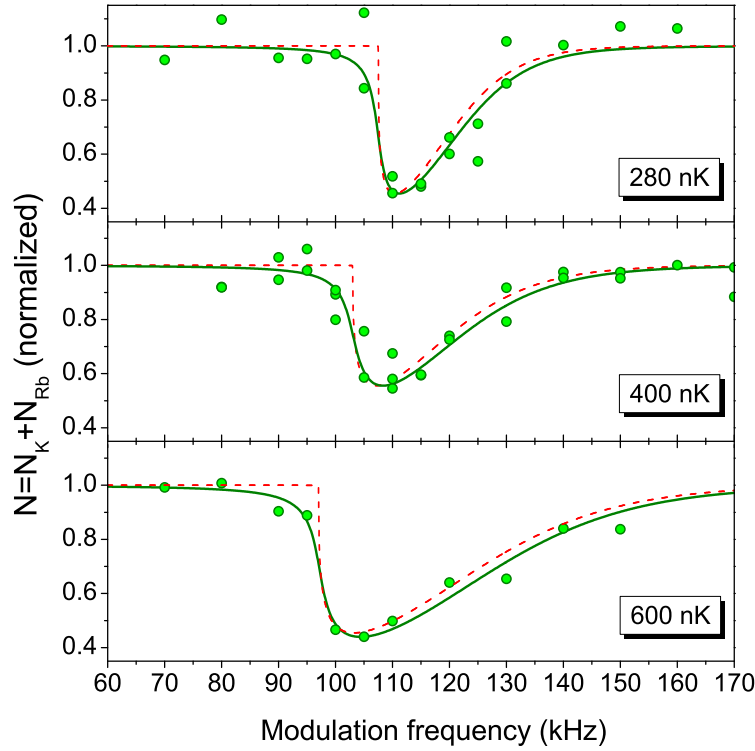
Figure 3.11: Line shapes of the molecular association process for different values of temperature. Data are taken after a rf pulse of 30 ms length around $B=78.2$ G. Solid lines are the fits made with eq. (3.12), taking E_b, γ and Ω_0 as free parameters. The temperature is measured from the ballistic expansion of the clouds. Dashed lines are the fits assuming $\gamma = 0$.

nearly-degenerate gases [38, 39, 46]. Fitting the association spectra we can hence extract the molecular binding energy E_b, that is one of the fit parameters.

Together with the binding energy, from fits we can obtain an estimate for the molecular lifetime $\tau = 1/\gamma = 60\mu s$, with an uncertainty of a factor 3. In Fig. 3.11 are compared the best fits with fits made assuming no decay. It is evident that the finite lifetime of the molecules smoothens the left edge of the association line shapes. From the association spectra we can only estimate a lower limit for the lifetime ($\tau > 20$ μs) while an upper limit ($\tau < 5$ ms) can be deduced from the lack of an observable atom decay after the rf pulse is terminated. However, the unitary limit constraints the inelastic atom-dimer collision to give a lower limit for the lifetime of the order of 100 μs; for this reason we associate the observed smoothening of the spectra to a technical-induced broadening, maybe driven by magnetic field fluctuations.

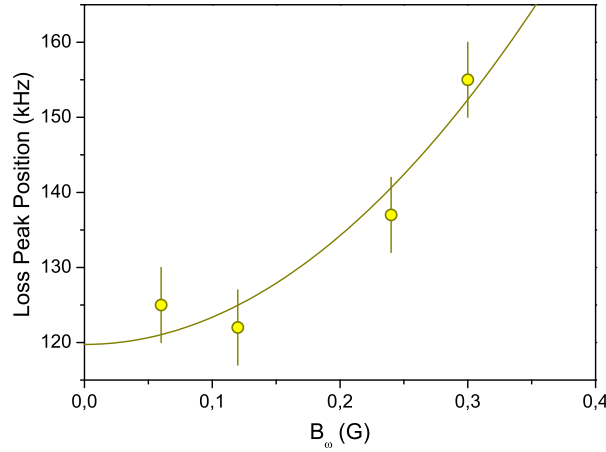Aside from the measurement of the binding energy and of the molecular lifetime

Figure 3.12: Shift of the resonant modulation frequency as a function of the modulation amplitude. The measurement is taken at $B=78.3$ G with 15 ms of rf pulse length and with a temperature of 350 nK. The solid line is a parabolic fit, as explained in the text.

an accurate analysis of the association spectra reveals other non-trivial features that must be taken into account and that can be described with our model.

First, we observe a shift of the modulation resonant frequency that increases with the modulation amplitude (see Fig. 3.12). This can be understood considering the quadratic dependence of the binding energy on the magnetic field: $E_b = \eta[\Delta B + B_\omega \sin(2\pi f_m t)]^2$, where ΔB is the detuning from the Feshbach resonance and η is the curvature. It is very easy to verify that the time-averaged value of the transition energy $\langle E(t) \rangle = \langle E_{kin} + E_b \rangle$ deviates from the value $E_{kin} + \eta \Delta B^2$ by an amount $\eta B_\omega^2/2$. Taking into account this effect we can extrapolate the correct zero-modulation amplitude frequency, as reported in Fig. 3.12. For the high-field resonance we must correct the measured resonant frequencies by -6 kHz, corresponding to a modulation amplitude of 0.13 G, while, for the low-field resonance, no correction is needed since the molecular binding energy is approximately linear with the magnetic field in the region where we take the measurements.

Another interesting feature that we observe in our measurement is that molecular association can occur also for a frequency that is half the resonant frequency f_m, as shown in Fig. 3.13. This allows us to to access a range of binding energies which lies outside the bandwidth of our excitation coil (50-200 kHz), effectively doubling the range of the measurable binding energies. Association of molecules at half the resonance frequency is due to the fact that since the binding energy is modulated at the frequency f_m the molecular amplitude contains Fourier components oscillating at
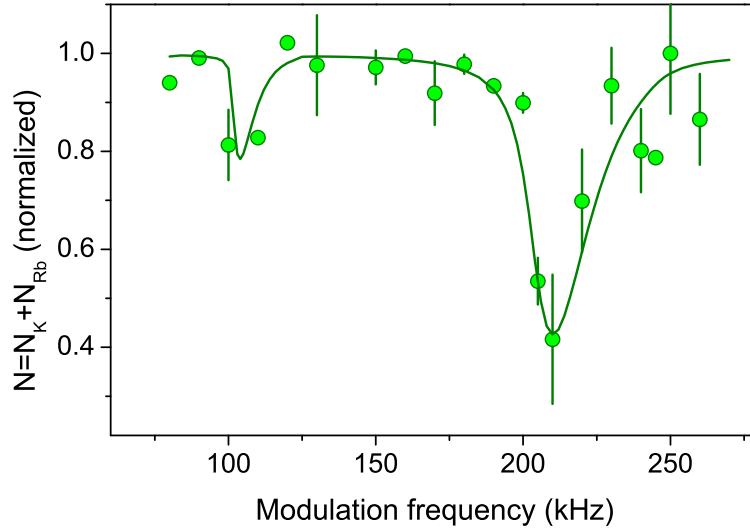
Figure 3.13: Association spectrum at $B = 78.24$ G with a rf pulse length of 15 ms. Note that we observe molecular association also at half the resonance frequency. The solid line is the result of numerical integration of eqs. (3.7).

integer multiples of f_m. When one of these harmonics is close to the time-averaged value of the binding energy, it can happen that a transfer of population occurs. This process can be described with the set of rate eqs. (3.7) indeed, solving them numerically, we can reproduce the association spectra as the one reported in Fig. 3.13.

Measurement of the s-wave Resonances Positions

Our simple model can take into account all the experimental features regarding the association spectra and is very useful to extract the correct molecular binding energy from data. Indeed, for several values of B, we measure the corresponding binding energy by fitting the experimental spectra with the theoretical model. The results are showed Fig. 3.14 where experimental data are compared with the theoretical prediction of [24]. The agreement between data and theory is fairly good once the theoretical curve is translated by -0.24 G for the high-field resonance and by -1 G for the low-field resonance (see Fig. 3.14).

As it was explained in chapter 1 a precise determination of the positions of Feshbach resonances can be made looking at the points where the molecular binding energy curves cross the threshold energy of the two colliding atoms. For this reason our most accurate measurement of the positions of the two s-wave Feshbach reso-
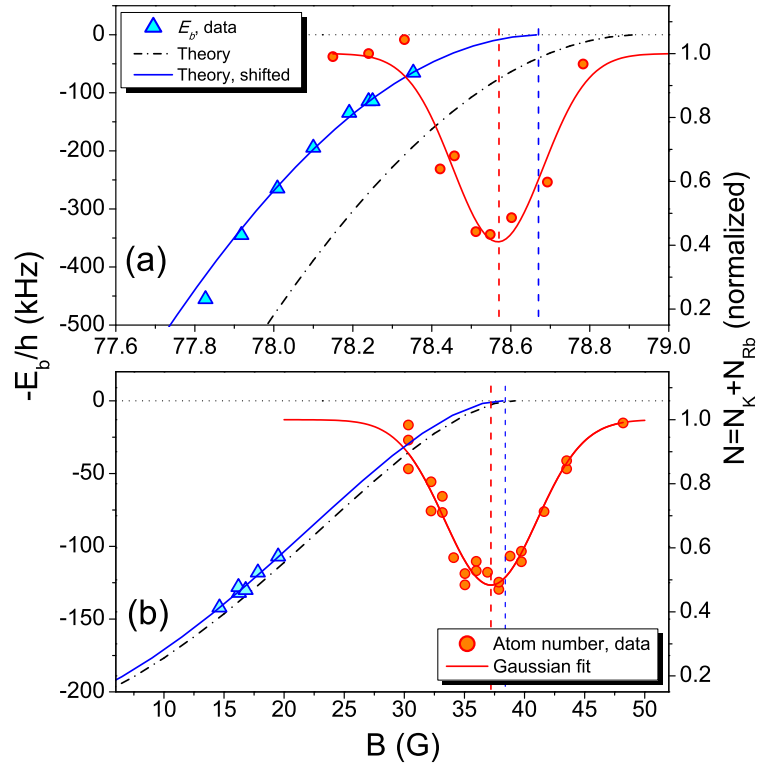
Figure 3.14: (a) KRb binding energy and three body losses as a function of the magnetic field for the high-field resonance. Triangles show the experimental data for the binding energy while circles are the experimental data for the three-body loss measurement. Dash-dotted line is the theoretical prediction of [24]; the solid blue line is the same curve but translated by -0.24 G. The solid red line is a Gaussian fit to the atom number. The vertical dashed lines mark the position of the Feshbach resonances determined by three-body losses (left, blue) and by the binding energy (right, red). (b) Same as above but for the low-field resonance. Here the theoretical prediction is shifted by -1 G.

nances is given by the values of the magnetic field where the binding energy curves that fit our data intercept the atomic threshold. These values are 38.4 G for the low-field resonance and 78.67 G for the high-field resonance. This method gives the most precise values for the positions of Feshbach resonances since a small deviation of 50 mG in the B field leads to a shift of 50 kHz in the binding energy of the leftmost points of Fig. 3.14(a). For this reason the main limitation at the precision of this method, in our apparatus, is given by the day-to-day fluctuations of the B field for which we associate an uncertainty of ± 30 mG to the B field.

As a comparison, in Fig. 3.14 we report also the measurement of the Feshbach

positions obtained with the three-body losses. For both resonance, as expected, the peak of three-body losses lies below the value obtained by the binding energy measurement. As it was explained in the previous section this shift is mainly due to the thermally-activated dynamics between atoms and molecules.

Finally we observe a big difference on the efficiency of the association process between the two resonances. In particular on the low-field resonance the poor efficiency obliges us to use rf pulse of 1 s at the maximum of the modulation amplitude, that is 0.5 G. This is due to the fact that the coupling strength Ω_0 is significant only at detuning ΔB where the bare states of the open and the closed channels mix and the energy of the molecular level deviates from the linear dependence on the field. As shown in Fig. 3.14 this happens only for the high-field resonance, indeed we calculate that, for our measurement, Ω_0 is a factor 10 smaller on the low-field resonance.

With these precise measurements of the positions of the two s-wave resonances, together with the position of the two d-wave resonances, it is possible to optimize the collisional model of [24]. The fit of new data, taking into account also the data from other isotopic mixtures, gives the following values:

$$
\begin{aligned}
a_s &= -109.6(2)a_0 \\
a_t &= -213.6(4)a_0 \\
C_6 &= 4288(2)E_H a_0^6 \\
C_8 &= 4.76(5) \times 10^5 E_H a_0^8 \\
A &= 2.01(4) \times 10^{-3} E_H
\end{aligned}
\tag{3.14}
$$

where a_s and a_t are the scattering lengths that, respectively, parametrize the singlet and triplet Born-Oppenheimer potentials.

3.3   Efimov Effect in Asymmetric Systems

Three-body systems are present at all length scales and in every physics field: the most striking examples could be the Sun-Earth-Moon system, the Helium atom or the proton. Despite their importance, yet the complexity of such systems challenges our complete understanding of their properties. A particular class of three-body systems arises when the constituents feature resonant pair wise interactions. In few seminal papers, appeared in early 70s, V. Efimov impressively advanced our understanding of such three-body systems and demonstrated the existence of a large

number of weakly bound states, thereafter known as the *Efimov effect* [52, 53]. According to Efimov's analysis, when at least two scattering lengths are much larger than the range of the pair potential (resonant interactions), the potential energy of the three-body system scales as its inverse size squared, $1/R^2$. This potential, if attractive, admits an infinite number of bound states, whose spectrum accumulates as a geometric series at zero energy $E_{n+1} = E_n \exp(-2\pi/s_0)$ (see Fig. 3.15), where s_0 depends only on the statistics and the masses of the constituents.

A convenient way to deal with the three-body problem

$$\left(-\frac{\hbar^2}{2m} \sum_{i=1}^{3} \nabla_i^2 + V(\mathbf{r}_1, \mathbf{r}_2, \mathbf{r}_3) \right) \Psi = E\Psi \tag{3.15}$$

is to formulate it in terms of *hyperspherical coordinates*. In order to define hyperspherical coordinates, we first introduce Jacobi coordinates. A set of Jacobi coordinates consists of the separation vector $\mathbf{r}_{ij}$ between a pair of atoms and the separation vector $\mathbf{r}_{k,ij}$ of the third atom from the center-of-mass of the pair. For atoms of equal mass, the Jacobi coordinates are

$$\mathbf{r}_{ij} = \mathbf{r}_i - \mathbf{r}_j \qquad \mathbf{r}_{kij} = \mathbf{r}_k - \frac{1}{2}(\mathbf{r}_i + \mathbf{r}_j). \tag{3.16}$$

The hyperradius R is defined as the root-mean-square separation of the three atoms:

$$R^2 = \frac{1}{3}(r_{12}^2 + r_{23}^2 + r_{31}^2) = \frac{1}{2}r_{ij}^2 + \frac{2}{3}r_{kij}^2. \tag{3.17}$$

The hyperradius is small only if all three atoms are close together. It is large if any single atom is far from the other two. With this definition we can expand the stationary wave function $\Psi(\mathbf{r}_1, \mathbf{r}_2, \mathbf{r}_3)$ of three identical atoms in terms of a complete set of hyperangular functions $\Phi_n(R, \Omega)$[1]:

$$\Psi(R, \Omega) = \frac{1}{R^{5/2}} \sum_n f_n(R) \Phi_n(R, \Omega) \tag{3.18}$$

where Ω is the set of hyperangular variables defined as $(\alpha_k, \mathbf{r}_{ij}, \mathbf{r}_{k,ij})$, being α_k one of the hyperangles.

Taking advantage of the orthonormality properties of the of hyperangular functions the Schrödinger equation for the $\Psi(\mathbf{r}_1, \mathbf{r}_2, \mathbf{r}_3)$ function reduces to a set of equations for the hyperradial functions $f_n(R)$. We can also make the simplifying assumption that the potential V can be expressed as the sum of three two-body potentials,

---

[1]The hyperangular functions are solutions to a differential eigenvalue equation in the hyperangular variables $[T_{\alpha_k} + \Lambda_{k,ij}^2/(2mR^2) + V(R, \Omega)]\Phi_n(R, \Omega) = V_n(R)\Phi_n(R, \Omega)$, where T_{α_k} is the kinetic energy operator associated with the hyperangle α_k and $\Lambda_{k,ij}^2$ is a generalized angular momentum operator.

each of which depends only on the separation r_{ij} of a pair of atoms. Hence, it can be demonstrated [54] that, in the low energy limit[2], the Schrödinger equation takes the following simple form

$$\left[\frac{\hbar_2}{2m} \left(\frac{\partial^2}{\partial R^2} + \frac{15}{4R^2} \right) + V_n(R) \right] f_n(R) \approx E f_n(R). \tag{3.19}$$

The above equation is valid in the adiabatic hyperspherical approximation, that consists on neglecting all the couplings between equations for different f_n. In the limit $R \ll |a|$ the hyperspherical potentials asymptote to $1/R^2$ potentials with different coefficients:

$$V_n(R) \rightarrow [\lambda_n(0) - 4] \frac{\hbar^2}{2mR^2} \tag{3.20}$$

where $\lambda_n(R)$ are the eigenvalues of the (3.19) problem with vanishing V_n potentials. It can be demonstrated [54] that the above potential is attractive, i. e., supports bound states, only for the lowest channel $n = 0$ and repulsive for the other. The channel eigenvalue for $n = 0$, in the resonant limit $a \rightarrow \pm\infty$ is $\lambda_0(R) = -s_0^2$, where, for three identical bosons, s_0 is the solution of the transcendental equation

$$s_0 \cosh(\pi s_0/2) = \frac{8}{\sqrt{3}} \sinh(\pi s_0/6). \tag{3.21}$$

Its numerical value is $s_0 \sim 1.00624$, so $e^{\pi/s_0} \sim 22.7$. The equation for the hyperradial wave function f_0 thus reduces to

$$\frac{\hbar^2}{2m} \left[-\frac{\partial^2}{\partial R^2} - \frac{s_0^2 + 1/4}{R^2} \right] f_0(R) = E f_0(R). \tag{3.22}$$

The above equation admits an infinite series of bound states, called Efimov states, whose spectrum can be expressed in the form [54]

$$E_n = (e^{2\pi/s_0})^n \epsilon. \tag{3.23}$$

In real systems, the potential energy scales as $1/R^2$ only for R in a range bound by the effective range r_e and the absolute value of the scattering length $a \gg r_e$ of the pair interactions. As a consequence the number of bound states is large but finite, of the order of $s_0/\pi \log(|a|/r_e)$ [54].

What makes Efimov states truly remarkable is their *universality*, i.e., the fact that the above properties are independent from the details of the pair short-range

---

[2]The low energy limit consists on taking into account only those states with total angular momentum quantum number $L = 0$.

potential, be it the strong interaction between two nucleons or the van der Waals force between two neutral atoms.

For over 35 years, the work of Efimov sparked an intense theoretical research [54], while eluding experimental observation. In nuclei, the Efimov effect is hampered by long-range Coulomb interactions, that make the potential energy scale as $1/R$ at large distance, and therefore confined to triads where at least two constituents are neutral. Among these, halo nuclei, i.e., nuclei like ^{6}He, ^{11}Li, ^{14}Be, ^{20}C composed of a smaller core nucleus plus two loosely bound neutrons, have been identified as possible examples of Efimov physics [55].

The first experimental evidence of Efimov states was only recently reached with ultracold ^{133}Cs [8] and ^{39}K [56] atoms. The key advantage of cold atoms has proven to be the possibility to adjust at will the scattering length by means of Feshbach resonances. However, unlike the ^{133}Cs and ^{39}K samples, most systems where Efimov physics is long sought are composed of distinguishable particles with different masses, those systems are usually called *asymmetric systems*. In this context our system can play a fundamental role since it allows to tune the interspecies interactions between different atomic species providing, therefore, the possibility to experimentally access an Efimov asymmetric system.

In the case where two of the three particles have the same mass and where only two interactions are resonant, as in our system, the above analysis is still valid, even if a little more complicated, and the scaling factor s_0 obeys the following equation [57]:

$$s_0 \cosh(s_0 \pi/2) \sin(2\phi) = 2 \sinh(s_0(\pi/2 - \phi)) \tag{3.24}$$

with

$$\phi = \arctan\left(\sqrt{\frac{m_i(m_i + 2m_j)}{m_j^2}}\right). \tag{3.25}$$

In ultracold atomic gases, the presence of deeply bound two-body molecular levels makes the Efimov states fragile and unstable upon collisions with free atoms. For this reason, direct observation of an Efimov state has never been achieved. However, Efimov states, when existing, bear a dramatic impact in the three-body recombination collision rate [54, 8] and can be detected by measuring the three-body inelastic collision rates as the resonant scattering length is varied. A pictorial scheme of the Efimov scenario in the proximity of a Feshbach resonance is shown in Fig. 3.15.

For a certain negative value of the two body scattering length a_-, the binding energy of an Efimov state vanishes, i.e., the energy of the trimer coincides with that
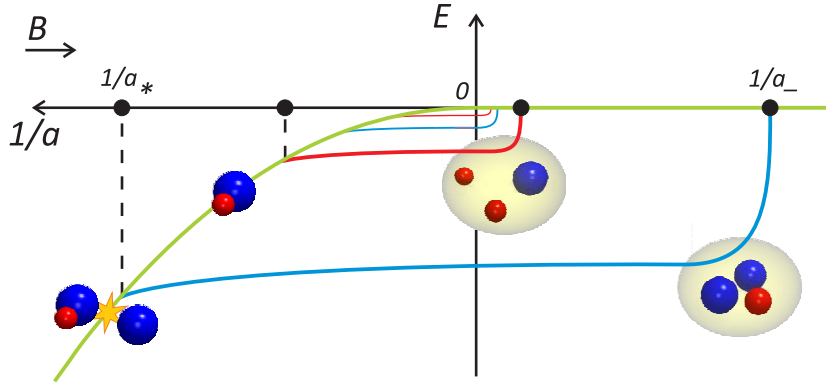
Figure 3.15: Pictorial energy diagram of the Efimov scenario in the proximity of an interspecies Feshbach resonance, that is where the scattering length diverges ($1/a = 0$). The black dots indicate the points where Efimov resonances are expected to appear. On the side of negative scattering length, a_- is the point where the energy of an Efimov trimer hits the three-atoms threshold. On the side of positive scattering length, a_* is the point where the atom-dimer threshold crosses the energy of an Efimov state. In our system two distinct kinds of Efimov series are possible: KKRb (red) and KRbRb (blue).

of three free atoms (see Fig. 3.15). At this scattering length a_-, the coupling between free atoms and trimers is resonantly enhanced, together with the three-body inelastic collisions. Hence, we expect to have an enhancement of the three-body losses around a_-, the center of the Efimov resonance.

For positive values of the scattering length the Efimov scenario is richer. The three-body recombination rate displays an oscillatory behaviour, with broad maxima and minima. In addition, at a scattering length value a_*, the energy of the Efimov trimer hits the atom-dimer threshold (see Fig. 3.15): here, a resonant enhancement occurs for the atom-dimer collisions, both elastic and inelastic. Therefore, an Efimov resonance is expected to appear also for a_* and it can be detected as an enhancement of the losses from the trap.

In the limit of infinite $|a|$ the above features repeat for each state of the Efimov spectrum as the scattering length is multiplied by an integer power of the scaling factor e^{π/s_0}, e. g. $a_-^{i+n} = a_-^i \exp(n\pi/s_0)$. This can happen rigorously only in the universal regime, i. e., where the scattering length is much larger than the Van der Waals length.

While the values of the scattering lengths a_- and a_* depend on the details of the atomic potential and are so far unpredictable, theoretical predictions are available

for their ratios, a_*/a_-, at least in systems of identical particles [54].

As it was explained at the beginning of this chapter, in our system we have four distinct three-body loss channels and, among them, only the heteronuclear ones are enhanced in the proximity of the interspecies Feshbach resonances. Correspondingly there exist two Efimov series, one for the KKRb trimers and one for the KRbRb trimers (see Fig. 3.15). From eq. (3.24) we can calculate the scaling factors e^{π/s_0} for the two series; for the KKRb series we have that $e^{\pi/s_0}=3.15\times10^5$ while for the KRbRb series $e^{\pi/s0} = 131$.

The relative location of the two series is unpredictable but the first Efimov resonances are expected to appear in the range $l_{VdW} < |a_-| < l_{VdW}e^{\pi/s_0}$, i.e., $72a_0 < |a_-| < (9.4 \times 10^3)a_0$ for the KRbRb series and $72a_0 < |a_-| < (2.5 \times 10^7)a_0$ for the KKRb series. However, in practice, the range of useful scattering length is heavily reduced from above by the unitary limit, that, looking at eq. (1.21), depend on the temperature, since $k^2 \propto k_B T$. We will see in the following that this unitary limit plays a fundamental role for the detection of one of our Efimov features.

Since, as explained above, the Efimov physics dramatically modifies the three-body scenario in the proximity of a Feshbach resonance, we expect to observe three-body loss peaks at a_- and a_*, where the three-body recombination rate and the atom-dimer collision rate are enhanced. Hence, experimentally, for the detection of the Efimov resonances we can employ the same scheme that we use for the Feshbach resonances. Once the mixture is prepared in the $|1, 1\rangle$ state we set the B field to 76 G, where the scattering length is $\simeq 200a_0$, and we perform the evaporation to the desired temperature, lowering the trap depth in 3 s. Typically, at 400 nK we have 10^5 Rb atoms and 5×10^4 K atoms. After this, we ramp the B field at the desired value in 20 ms and we hold the atoms for a fixed hold time t_h, during which the atom number decay due to three-body recombination losses. At the end we switch off the trap and the B field and we image the two clouds. Again, our main observable is the total number of atoms $N(t_h) = N_K(t_h) + N_{Rb}(t_h)$, that we record scanning the B field. The behaviour of N as a function of the magnetic field can be reproduced integrating eqs. (3.2) over the volume, the detailed analysis is presented in the following.

Rate Equations

For what concerns the Efimov physics in asymmetric systems, on the side of positive scattering length the dependence of the atomic densities on the hold time t_h is governed by eqs. (3.2). The relative equations for the atomic populations can be

derived simply integrating eqs. (3.2) over the volume. Let us consider only one three-body recombination channel, A+A+B→ A+AB=A+D:

$$\dot{n}_A = -2\alpha n_A^2 n_B$$
$$\dot{n}_B = -\alpha n_A^2 n_B$$
$$\dot{n}_D = \alpha n_A^2 n_B. \tag{3.26}$$

The integration over the volume yields the following rate equations for the atom and molecules number populations:

$$\dot{N}_A = -2\alpha N_A^2 N_B \frac{\int n_A^2 n_B d^3 x}{(\int n_A d^3 x)^2 \int n_B d^3 x}$$
$$\dot{N}_B = -\alpha N_A^2 N_B \frac{\int n_A^2 n_B d^3 x}{(\int n_A d^3 x)^2 \int n_B d^3 x}$$
$$\dot{N}_D = \alpha N_A^2 N_B \frac{\int n_A^2 n_B d^3 x}{(\int n_A d^3 x)^2 \int n_B d^3 x}. \tag{3.27}$$

Since we work with thermal clouds the atomic densities have a Gaussian profile. Considering also the gravitational differential sag we can write $n_A = n_{0A} \exp(-\theta(x^2 + y^2 + z^2))$ and $n_B = n_{0B} \exp(-\theta(x^2 + y^2 + (z - z_0)^2))$, where $\theta = m_i \omega_i^2 / 2k_B T$ and $z_0 = g/(\omega_A^2 - \omega_B^2)$, being g the gravitational acceleration. Hence, performing all the integrations contained in eqs. (3.27), we find that

$$\dot{N}_A = -2\alpha N_A^2 N_B \frac{1}{\sqrt{27}} \left(\frac{\theta}{\pi}\right)^3 e^{-\frac{2}{3}z_0^2 \theta} = -2\alpha\gamma(T) N_A^2 N_B$$
$$\dot{N}_B = -\alpha\gamma(T) N_A^2 N_B$$
$$\dot{N}_D = \alpha\gamma(T) N_A^2 N_B. \tag{3.28}$$

The final equations for the atomic populations can be derived simply including the other three-body recombination process, thus leading to

$$\dot{N}_{Rb} = -2\alpha_{KRbRb}\gamma(T) N_{Rb}^2 N_K - \alpha_{KKRb}\gamma'(T) N_{Rb} N_K^2$$
$$\dot{N}_K = -\alpha_{KRbRb}\gamma(T) N_{Rb}^2 N_K - 2\alpha_{KKRb}\gamma'(T) N_{Rb} N_K^2$$
$$\dot{N}_{(KRb)} = \alpha_{KRbRb}\gamma(T) N_{Rb}^2 N_K + \alpha_{KKRb}\gamma'(T) N_{Rb} N_K^2. \tag{3.29}$$

On the side of positive scattering length we have instead to consider the inelastic scattering between atoms and dimers: A+D* →A+D. These kind of collisions are governed by the following rate equations

$$\dot{n}_A = -\beta n_A n_D$$
$$\dot{n}_D = -\beta n_A n_D \tag{3.30}$$

that, again, through the integration over the volume, provide the rate equations for the atomic and molecular populations:

$$
\begin{aligned}
\dot{N}_{Rb} &= -\beta_{KRbRb}\gamma''(T)N_{Rb}N_{KRb} \\
\dot{N}_{K} &= -\beta_{KKRb}\gamma'''(T)N_{K}N_{KRb} \\
\dot{N}_{(KRb)} &= -\beta_{KRbRb}\gamma''(T)N_{Rb}N_{KRb} - \beta_{KKRb}\gamma'''(T)N_{K}N_{KRb}.
\end{aligned} \tag{3.31}
$$

The α coefficients must depend on a^4, as explained in section 3.1, and must contain the intrinsic log-periodicity of the Efimov physics. Also the β coefficients must contain information about the Efimov periodicity. Actually, for the heteronuclear case, the explicit expressions for α and β are unknown. For this reason we perform the calculations tracing the homonuclear formulas of Ref. [58], so that the event collision rates for the three-body recombination process and for the inelastic atom-dimer collisions (at zero temperature) are

$$
\begin{aligned}
\alpha_{ijj} &= C\frac{\sinh(2\eta)}{\sin^2[s_0(\delta)\log(a/a_-)] + \sinh^2(\eta)}\frac{\hbar a_\delta^4}{\mu_\delta} \\
\beta_{ijj} &= D\frac{\sinh(2\eta_*)}{\sin^2[s_0(\delta)\log(a/a_*)] + \sinh^2(\eta_*)}\frac{\hbar a_\delta}{\mu_\delta}
\end{aligned} \tag{3.32}
$$

where $\delta = m_i/m_j$, $a_\delta = a\sqrt{\delta(\delta+2)}/\sqrt{\delta}$ and $\mu_\delta = m_i/\sqrt{\delta(\delta+2)}$. The parameters η and η_* are the widths of the resonances, while C and D are simple multiplicative factors.

It is instructive, at this point, to understand also the energetic behaviour of the system when the Efimov physics takes place. On the side of negative scattering length, considering only one collisional channel, we can write that the energy densities, i. e., the energies per unit of volume, obey the following rate equations:

$$
\begin{aligned}
\dot{\mathcal{E}}_A &= \alpha n_A^2 n_B\left(-\xi_A(\mathbf{r}) + E_b\frac{m_D}{m_A + m_D}\right) \\
\dot{\mathcal{E}}_B &= \alpha n_A^2 n_B(-\xi_B(\mathbf{r})) \\
\dot{\mathcal{E}}_D &= \alpha n_A^2 n_B^2 E_b\frac{m_A}{m_A + m_D}
\end{aligned} \tag{3.33}
$$

where E_b is the molecular binding energy and $\xi_i = E_i^{kin} + U_i(\mathbf{r})$ is the sum of the kinetic and potential energy of the atom i in $\mathbf{r}$. The integration over the volume leads to

$$
\dot{E}_A = \alpha\gamma(T)N_A^2 N_B\left(-\frac{\int n_A^2 n_B\xi_A d^3x}{\int n_A^2 n_B d^3x} + E_b\frac{m_D}{m_A + m_D}\right)
$$

$$\dot{E}_B = \alpha\gamma(T)N_A^2 N_B \left(-\frac{\int n_A^2 n_B \xi_B d^3 x}{\int n_A^2 n_B d^3 x}\right)$$

$$\dot{E}_D = \alpha\gamma(T)N_A^2 N_B E_b \frac{m_A}{m_A + m_D}. \tag{3.34}$$

Since

$$\frac{\int n_A^2 n_B \xi_i d^3 x}{\int n_A^2 n_B d^3 x} = \langle \xi_i \rangle = E_i^{kin} + \langle U_i \rangle, \tag{3.35}$$

$E_i^{kin} = 3k_B T/2$ and $\langle U_A \rangle = k_B(T + T_s)/2$ and $\langle U_B \rangle = k_B(T + 4T_s)/2$, with $T_s = m_i \omega_i^2 z_0^2/9k_B$, including both collisional channels, eqs. (3.34) become

$$\dot{E}_{Rb} = \alpha_{KRbRb}\gamma(T)N_{Rb}^2 N_K \left(-2k_B T - \frac{1}{2}k_B T_s + E_b \frac{m_{(KRb)}}{m_{Rb} + m_{(KRb)}}\right) +$$

$$+ \ \alpha_{KKRb}\gamma(T)N_K^2 N_{Rb}(-2k_B T - 2k_B T_s)$$

$$\dot{E}_K = \alpha_{KRbRb}\gamma(T)N_{Rb}^2 N_K(-2k_B T - 2k_B T_s) +$$

$$+ \ \alpha_{KKRb}\gamma(T)N_K^2 N_{Rb}\left(-2k_B T - \frac{1}{2}k_B T_s + E_b \frac{m_{(KRb)}}{m_{(KRb)} + m_K}\right)$$

$$\dot{E}_{(KRb)} = \alpha_{KRbRb}\gamma(T)N_{Rb}^2 N_K E_b \frac{m_{Rb}}{m_{Rb} + m_{(KRb)}} +$$

$$+ \ \alpha_{KKRb}\gamma(T)N_K^2 N_{Rb} E_b \frac{m_K}{m_K + m_{(KRb)}}. \tag{3.36}$$

On the side of positive scattering length we have to consider both the elastic and inelastic atom-dimer collisions. Elastic collisions can be described by the following set of rate equations

$$\dot{\mathcal{E}}_A = n_A n_D \sigma_{AD} v_{rel} \frac{2m_A m_D}{(m_A + m_D)^2}\xi_D(\mathbf{r})$$

$$\dot{\mathcal{E}}_D = -n_A n_D \sigma_{AD} v_{rel} \frac{2m_A m_D}{(m_A + m_D)^2}\xi_D(\mathbf{r}) \tag{3.37}$$

while the inelastic scattering by

$$\dot{\mathcal{E}}_A = -\beta n_A n_D \xi_A(\mathbf{r})$$

$$\dot{\mathcal{E}}_D = -\beta n_A n_D \xi_D(\mathbf{r}). \tag{3.38}$$

Performing the integral over the volume and including both collisional channels we obtain

$$\dot{E}_{Rb} = 2N_{Rb}N_{(KRb)}\tilde{\sigma}_{KRbRb}\left(\frac{3k_B T_{KRb}}{m_{(KRb)}}\right)^{1/2}\frac{2m_{Rb}m_{(KRb)}}{(m_{Rb} + m_{(KRb)})^2}\chi(T_{Rb}, T_{(KRb)}) +$$

$$- \ \tilde{\beta}_{KRbRb}N_{Rb}N_{(KRb)}\chi(T_{Rb}, T_{(KRb)})$$

$$\dot{E}_{Rb} = 2N_K N_{(KRb)} \tilde{\sigma}_{KKRb} \left(\frac{3k_B T_{KRb}}{m_{(KRb)}} \right)^{1/2} \frac{2m_K m_{(KRb)}}{(m_K + m_{(KRb)})^2} \chi(T_K, T_{(KRb)}) +$$
$$- \tilde{\beta}_{KKRb} N_K N_{(KRb)} \chi(T_K, T_{(KRb)})$$
$$\dot{E}_{(KRb)} = -2N_{Rb} N_{(KRb)} \tilde{\sigma}_{KRbRb} \left(\frac{3k_B T_{KRb}}{m_{(KRb)}} \right)^{1/2} \frac{2m_{Rb} m_{(KRb)}}{(m_{Rb} + m_{(KRb)})^2} \chi(T_{Rb}, T_{(KRb)}) +$$
$$- \tilde{\beta}_{KRbRb} N_{Rb} N_{(KRb)} \chi(T_{Rb}, T_{(KRb)}) +$$
$$- 2N_K N_{(KRb)} \tilde{\sigma}_{KKRb} \left(\frac{3k_B T_{KRb}}{m_{(KRb)}} \right)^{1/2} \frac{2m_K m_{(KRb)}}{(m_K + m_{(KRb)})^2} \chi(T_K, T_{(KRb)}) +$$
$$- \tilde{\beta}_{KKRb} N_K N_{(KRb)} \chi(T_K, T_{(KRb)}) \tag{3.39}$$

with

$$\tilde{\sigma}_{AD} = \sigma_{AD} \left[\frac{m_A \omega_A^2}{\pi k_B (T_D - 2T_A)} \right]^{3/2} e^{-\frac{m_A \omega_A^2 z_0^2}{4k_B(T_D + 2T_A)}}$$
$$\tilde{\beta}_{AD} = \beta_{AD} \left[\frac{m_A \omega_A^2}{\pi k_B (T_D - 2T_A)} \right]^{3/2} e^{-\frac{m_A \omega_A^2 z_0^2}{4k_B(T_D + 2T_A)}}$$
$$\chi(T_A, T_D) = \frac{3}{2} k_B T_D + \frac{3}{2} k_B T_D \frac{T_A}{T_D + 2T_A} + \frac{1}{4} k_B T_s \frac{1}{(1 + 2T_A/T_D)^2} \tag{3.40}$$

where also the cross section σ_{AD} reflects the Efimov periodicity through [58]

$$\sigma_{AD} = D_{AD} \frac{a_\delta^2}{\sin^2(s_0(\delta) \log(a/a_*)) + \sinh^2(\eta_*)}. \tag{3.41}$$

Detection of Efimov Resonances

We look for Efimov feature around the low-field Feshbach resonance since in the proximity of that one the scattering length varies smoothly with the B field. Indeed, on the side of negative scattering length, we observe two distinct peaks of three-body losses. The broadest one, located at $\sim$57.7 G is very strong and is visible up to a temperature of 800 nK. The other one, that lies at $\sim$38.8 G, is weaker, narrower and visible only below 300 nK (see Fig. 3.16).

To be sure that these peaks are genuine interspecies three-body features we have made the following considerations and experimental verifications:

- Inelastic two-body collisions are suppressed since both species are in the $|1, 1\rangle$ absolute ground state.

- As a control we checked that both loss peaks are absent if we prepare samples with only one species.

- From the collisional model and from Fig. 3.4 we can verify that no sufficiently broad Feshbach resonances occur at the corresponding magnetic field values, even considering molecular levels with $l = 1, 2$.

- We have checked that the frequency offset between the two crossed trap beams (~ 220 MHz) is far detuned from any bound state, in order to avoid Raman transitions to molecular levels.

- For the broad peak we collect the individual species atom number varying the hold time in the center of the resonance, as reported in Fig. 3.17. Let us define the quantity $N_{Rb,i} - zN_{K,i}$, where the index i runs over the experimental data points. We expect that for the three-body KRbRb collisions $N_{Rb,i} - 2N_{K,i}$ remains constant, yielding $z = 2$. Vice versa for KKRb collisions $N_{Rb,i} - 0.5N_{K,i}$ must be constant. Minimizing the quantity $\sum_i (A - (N_{Rb,i} - zN_{K,i}))^2$ with respect to the parameters A, z we find that for the data-set of Fig. 3.17 $z = 1.7(3)$, indicating that the atom decay is due to the three-body process KRbRb.

We cannot rely on this decay measurement for B field values near to the Feshbach resonance since the signal-to-noise of the atomic decay is insufficient to distinguish between the different three-body recombination channels. Thus, for the weaker peak at 38.8 G we analyze the individual atom number at fixed hold time. From our data set we calculate the linear combination $2N_K - N_{Rb}$, that is expected to be constant for KRbRb collisions and to display a negative peak for KKRb collisions. Such a peak is indeed observed, as shown in Fig. 3.16(b), and we assign the resonance at 38.8 G to the KKRb channel. For comparison in Fig. 3.16(d) is plotted the combination $2N_{Rb} - N_K$ for the Efimov resonance at 57.7 G. As expected we observe a negative peak for that combination reinforcing the assignment of that resonance to the KRbRb channel.

To strengthen the channels assignment and to derive the three-body recombination coefficients, we model the loss process by the set of differential rate equations described above. The differential equations are numerically integrated and the parameters denoting the position, amplitude and width of the Efimov peaks are adjusted to the experimental data of atom number after a fixed hold time. We find that the KRbRb channel dominates three-body recombination collisions at nearly all magnetic fields, with the exception of a narrow region next to Feshbach resonance where we detect the Efimov peak due to the KKRb channel (see Fig. 3.16(a),(b)). Indeed, for the weaker peak at 38.8 G we must introduce the unitary limit for the
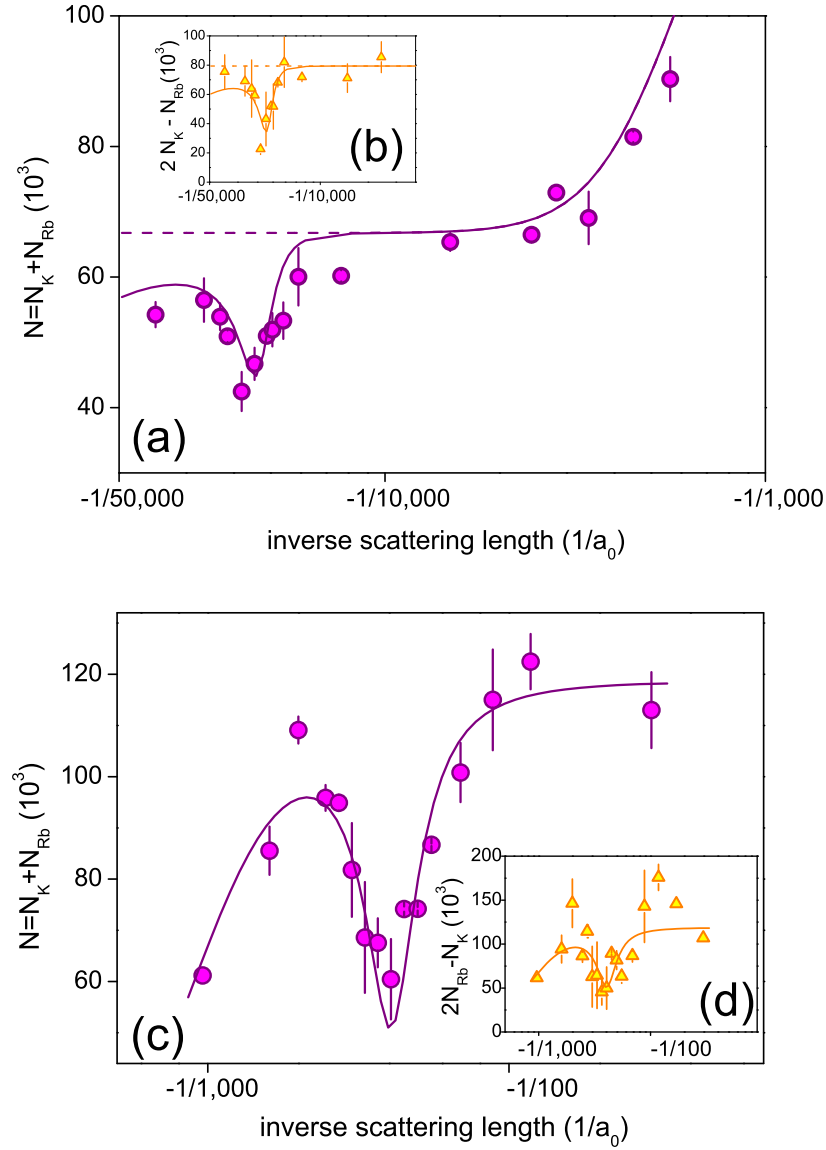
Figure 3.16: Peaks of inelastic atomic losses at negative scattering length. (a),(b) KKRb Efimov resonance at 38.8 G; (c),(d) KRbRb Efimov resonance at 57.7 G. In (a) and (c) are shown the total number of atoms $N = N_K + N_{Rb}$ remaining in the optical trap after a fixed hold time: 100 ms at 300 nK in (a) and 500 ms at 400 nK in (c). The solid lines refer to numerical results of our model. In the insets (b) and (d) are shown the linear combinations $2N_K - N_{Rb}$ and $2N_{Rb} - N_K$ respectively, supporting the channel assignment of the Efimov peaks (see text). The dashed lines in (a) and (b) show the numerical integration taking into account only the KRbRb collisional channel.
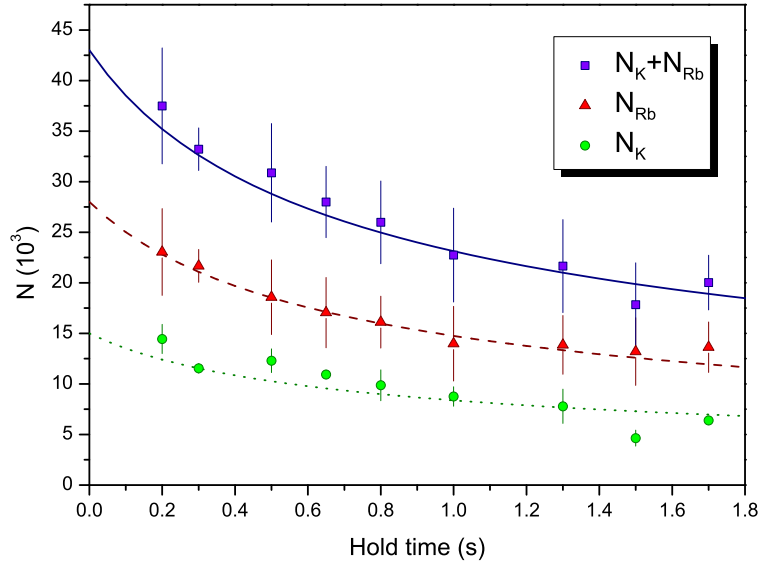
Figure 3.17: Decay of the number of atoms trapped in the dipole trap at $B = 56.8$ G. At this field the KRbRb collisional channel is enhanced, thus it is the only relevant one. The lines show the results of the numerical solution of eqs. (3.29) including only the KRbRb channel. From the fit we obtain that $K_3 = 4.2(1.7) \times 10^{-10}$ s^{-1} and, hence, $\alpha_{KRbRb} = 1.3\left(^{+1.5}_{-1.0}\right) \times 10^{-24}$ cm^6/s.

KRbRb channel. The unitary limit is a maximum value of the three-body recombination rate that we assume to be of the same order of magnitude as that of the homonuclear system, $\alpha_{max} \simeq 20\pi^2\hbar/(\mu_\delta k^4)$ [59]. In practice we replace α_{KRbRb} with an effective $\alpha_{eff} = \alpha_{max}\alpha_{KRbRb}/(\alpha_{max} + \alpha_{KRbRb})$, approximately equal to the minimum between α_{KRbRb} and α_{max}. As shown in Fig. 3.16 (a) and (b), the introduction of this limit allows us to nicely fit the data. For the broad peak at 57.7 G the introduction of the unitary limit is not necessary since the scattering length at this value of the B field is orders of magnitude smaller than the unitary-limited one (at 400 nK $a_{max} \sim 2400a_0$).

Numerically integrating eqs. (3.29) we can fit the data for both peaks, as shown in Fig. 3.16, once we adjust the fit parameters to the following values: $a_- = -246(14)a_0$, $\eta = 0.12(1)$ and $C = 34(6) \times 10^2$ in the α_{KRbRb} coefficient for the peak at 57.7 G and $a_- = -22\left(^{+4}_{-6}\right) \times 10^3 a_0$, $\eta = 0.017(10)$ and $C = 6(4) \times 10^{-4}$ in the α_{KKRb} coefficient for the peak at 38.8 G. The uncertainty on the positions reflects the estimated uncertainty on the B field ($\pm$ 50 mG). Interestingly, the widths η of the Efimov states are comparable with those observed in ^{133}Cs, 0.06 [8], and in ^{39}K, 0.05 [56]. We must notice that, since we observe no significant changes in the
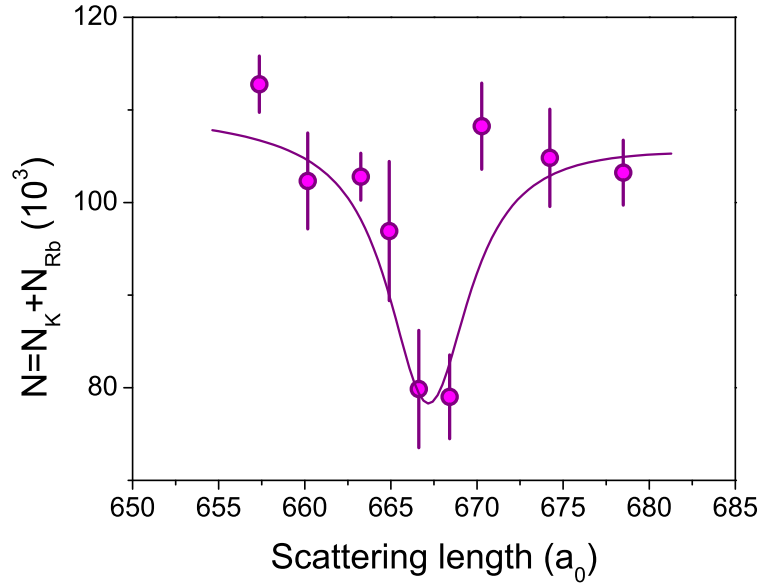
Figure 3.18: Peak of enhanced inelastic atom losses at positive scattering lengths, corresponding to the atom-dimer resonance. The total number of atoms remaining in the optical trap after a fixed hold time of 500 ms at the given the scattering length is shown. These data are taken at a temperature of 400 nK. Each point averages on 2 to 5 experimental runs. The solid line is the result of numerical integration of equations (3.31) and (3.39).

temperatures of the two samples, to fit the two peaks we integrate eqs. (3.29) with $\gamma(T)$ kept constant, i.e., omitting to integrate also eqs. (3.36).

For positive scattering length, the 3-body inelastic collision rate is expected to display an oscillatory behaviour with no sharp peaks. However, we observe a peak of atomic losses at $B=4.25(0.10)$ G, as shown in Fig. 3.18,. Loss peaks at positive values of the scattering length have been recently reported in ^{39}K [56] and attributed to resonantly enhanced secondary collisions between atoms and dimers created in three-body recombination processes. In a three-body recombination collision, the binding energy of the associated dimer is converted in kinetic energy, which is shared by the dimer itself and the remaining unbound atom, inversely proportional to their mass. When the kinetic energy of the dimer is larger than the depth of the optical trap, as is often the case, the dimer is lost but, while escaping from the trap volume, it can expel additional atoms either by sharing its kinetic energy upon elastic collisions or by undergoing inelastic collisions [56]. As explained above, the atom-dimer collisions are enhanced for values of the scattering length, $a = a_*$, where the Efimov

state intercepts the atom-dimer threshold: at this values, a resonance occurs in the atom-dimer scattering [60], similar to a Feshbach resonance. In analogy with [56], the narrow peak of losses at 4.2 G could be due to an atom-dimer resonance. The fit of the data reported in Fig. 3.18 is obtained by numerical integration of the rate equations (3.31) and (3.39). At these values of scattering length, dimers are mainly associated in the KRbRb channel: the fact that more Rb than K atoms are lost shows that dimers collide resonantly with Rb. The fit results are: $D = 1(.5) \times 10^{-4}$, $\eta_* = 2(1) \times 10^{-3}$ and $a_* = 667(1)a_0$. We notice that both the elastic cross section and the inelastic collision rate are approximately four orders of magnitudes lower than the theoretical results at zero temperature. Lower than predicted values of the inelastic collision rate β have been observed also in Cs [60], even if the discrepancy, in that case, is smaller. With the same arguments as above, we can exclude inelastic two body collisions to be the cause of this peak. However, even if data are nicely fitted by the theoretical model, further experimental and theoretical investigations are required to confirm the suggested interpretation. If confirmed, the atom-dimer resonance will allow us to assess the energy of the Efimov state, that, as shown in the picture of Fig. 3.15, is approximately equal to the dimer energy at 4.2 G, i.e. $h \times 0.2$ MHz.

Chapter 4

A Species-Selective Potential

In this chapter I present the experiments we have performed exploiting the specie-selective dipole potential (SSDP) described in chapter 2. By means of this potential we can selectively act on one of the two species (K) leaving the other (Rb) almost unperturbed. As described in section 1 we have used the SSDP to implement a novel scheme to reversibly cross the BEC transition for the K sample and to study the entropy exchange between two gases near the absolute zero [61]. Moreover, as reported in section 2, the SSDP, in the 1D optical lattice configuration, has allowed us to obtain the first experimental evidence of inter-dimensional physics through the observation of many inter-dimensional Feshbach resonances. Finally, in section 3, it is presented a theoretical analysis on the stability of a matter wave in a matter grating, that is a system that can be realized using the SSDP [62].

4.1 Entropy Exchange in Ultracold Atomic Mixtures

Cooling to lower temperatures often unveils new physical phenomena. In presence of a phase transition, the properties of a macroscopic physical system are strikingly altered, usually through the onset of some form of order. Notable examples are the solidification of a liquid, the superconductivity of a metal and the Bose-Einstein condensation of a gas. In recent years an intense research activity has been carried on in the context of quantum phases in condensed matter systems and in atomic quantum gases. Among those phases, ferromagnetic and antiferromagnetic ordered systems and frustrated systems are of particular interest, since they can own interesting useful properties for quantum computation schemes [63]. However, most of

these phases can only be reached provided that the temperature of the sample is suitably low.

Currently, the chief cooling technique in the domain of degenerate atoms is forced evaporation, which is efficient and well understood for harmonically trapped gases but not readily applicable to other important configurations, e.g. to atoms in deep optical lattices. Therefore, it is useful to devise alternative cooling strategies and to study how a sample exchange entropy with the surrounding. In addition to that, understanding the thermalization processes in strongly correlated systems is essential to engineer suitable thermometers. At present, measuring the temperature of atoms in deep optical lattices is still a challenging task, for which a straightforward measurement technique, like that used for harmonically trapped BEC, is both lacking and desirable.

The reduction and the precise control of the entropy is instrumental for the exploration of novel, strongly correlated, quantum phases. Indeed, to ascertain whether a given quantum phase is accessible, it is convenient to focus on the critical value of entropy, rather than temperature. The main advantage is especially clear when the strongly correlated regime is reached by slow, adiabatic, transformations of the trapping potential. For this reason it is of special importance to provide new schemes for the determination and the control of the entropy of quantum degenerate gases.

Our Bose-Bose mixture is particularly suitable to perform such an entropy management since it allows us to implement a simple textbook thermodynamics scheme of two distinguishable gases in an isolated box, exchanging neither particles nor energy with the outside. Let us suppose that a piston, permeable to one of the two gases (the auxiliary gas), compresses the other (the target gas) causing its temperature to increase. In thermal equilibrium, heat, and hence entropy, will flow from the target gas to the uncompressed auxiliary gas. In the limit of the auxiliary gas containing a large number of particles, it acts as a thermal bath.

Formally the above process can be described considering that the entropy S of an ideal gas of N particles is proportional to $\log(\Sigma/N)$, where Σ is the number of accessible single particle states. Σ increases with the energy density of states and with the average energy, i.e., the temperature. Therefore, in an adiabatic compression of one single gas, the reduction of the energy density of states is compensated by the temperature rising, such that Σ, and hence S, remains constant. If we add the uncompressed auxiliary gas in thermal contact, the temperature rise must be lower: Σ decreases for the target gas and increases for the auxiliary component.

In our experiment, we load the ^{41}K and ^{87}Rb samples in the millimetric trap and we sympathetically evaporate the mixture. Typically, at the end of the evaporation, we have 1×10^6 Rb atoms and 2×10^5 K atoms at ~ 400 nK. The magnetic trap provides a harmonic confinement with frequencies $(\omega_x, \omega_y, \omega_z) = 2\pi \times (24, 297, 297)$ Hz for K and a factor $\sqrt{m_K/m_{Rb}}$ smaller for Rb. The geometric mean frequencies for the two species are therefore $(\omega_{Rb}, \omega_K) = 2\pi \times (88, 128)$ Hz. To selectively act on the potential experienced by the K atoms (target gas) alone, we use a laser beam tuned to an intermediate wavelength between the D1 and D2 lines of Rb (auxiliary gas). At this wavelength, as explained in chapter 2, a species-selective dipole potential (SSDP) is produced. The beam, linearly polarized, with a waist of 55 μm, propagates along the horizontal $-y$ direction (Fig. 4.1). We experimentally determine the wavelength value to be 789.85(1) nm, by minimizing the efficiency of the Raman-Nath diffraction caused by a pulsed standing wave on a Rb condensate. With the same technique we also measured the residual potential acting on Rb to be $V_{Rb}/V_K = 0.08(1)$. From the measured temperature increase caused by the SSDP on Rb alone, we estimate a residual effective increase of ω_{Rb} lower than 7%, hereafter neglected. On the K sample, the additional confinement induced by the SSDP beam is instead a harmonic potential whose frequencies add in quadrature to those of the magnetic trap. The compression occurs mainly along the weak x axis of the magnetic trap (ω_x increases up to a factor 5), slightly along the z direction (ω_z increases less than 8%), and is utterly negligible along the propagation y axis of the SSDP beam. Overall, the dipole beam raises the ω_K up to a factor 1.7. Therefore, in our experiment, instead that in an isolated box, the gases are trapped by a magnetic harmonic potential and the role of the piston is played by a species-selective dipole potential (see Fig. 4.1), but the underlying physics is the same as described above.

We raise the power of the SSDP beam with an exponential ramp lasting 200 ms for maximum compression of the trap frequency $\omega_{Kf} = 2\pi \times 216$ Hz. The adiabaticity is preserved since the ramp is longer than the trapping periods of ^{41}K, i.e., (41,3.4,3.4) ms. Thermal equilibrium between the two gases is maintained throughout by making all transformations slow with respect to the interspecies collision times, a few ms in typical experimental conditions: we verified that the temperatures of the two species are always equal, within our statistical uncertainty. Our observables are the number of thermal atoms N_{th}, the number of condensed atoms N_c, and the temperature T of the two species that are measured by resonant absorption imaging after all confining potential are removed and the atomic clouds have expanded. For each species, the entropy is either computed from the measured tem-
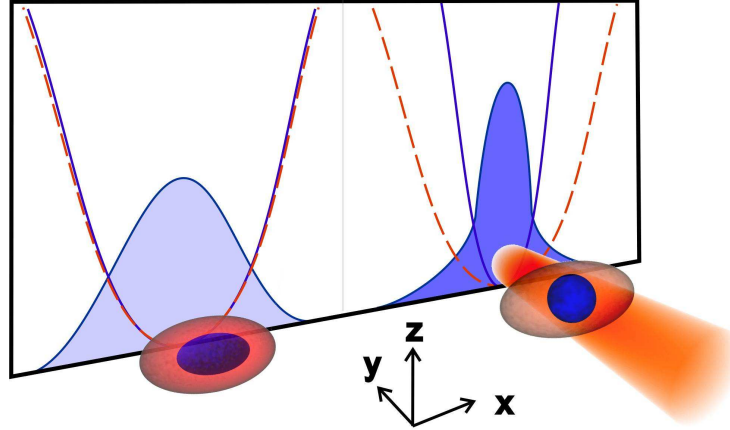
Figure 4.1: Pictorial scheme of the experimental procedure. Left: the harmonic magnetic potential is common to both gases, Rb (red,larger) and K (blue, smaller). Right: the species-selective dipole beam compresses the K sample alone driving it into the degenerate regime, keeping the Rb sample almost unchanged. On the background panels are sketched the trapping potential for the Rb (dashed line) and K (solid line) gas together with the K density distributions.

perature and atom number for samples above BEC or obtained from the condensate fraction below BEC.

To make quantitative predictions and to model the selective compression process we can start from the entropy of an ideal gas at temperature T in a harmonic potential with angular frequency ω [64]:

$$S = k_B N_T \left[4 \frac{g_4(z)}{g_3(z)} - \log(z) \right], \tag{4.1}$$

where N_T denotes the number of thermal atoms and the polylogarithmic functions are defined as

$$g_n(z) = \sum_{k \geq 1} \frac{z^k}{k^n}. \tag{4.2}$$

For temperatures above the BEC critical temperature T_c, $N_T = N$ and the fugacity z is implicitly given by

$$N = g_3(z) \left(\frac{k_B T}{\hbar \omega} \right)^3 \tag{4.3}$$

while, for $T \leq T_c$, $z = 1$ and

$$N_T = N \left(\frac{T}{T_c} \right)^3 = \frac{1}{\zeta(3)} \left(\frac{k_B T}{\hbar \omega} \right)^3, \tag{4.4}$$

with the ζ function defined by $\zeta(i) = g_i(1)$. Therefore, eq. (4.1) can be explicitly rewritten in the following form:

$$
S = \begin{cases}
4\dfrac{\zeta(4)}{\zeta(3)}Nk_B\left(\dfrac{T}{T_c}\right)^3 & T \leq T_c \\[3mm]
k_B N\left[4\dfrac{g_4(z)}{g_3(z)} - \log(z)\right] & T \geq T_c
\end{cases}.
\tag{4.5}
$$

In the presence of interactions the above expressions can still be considered valid in case of thermal, low dense, gases, while they must be modified for samples with temperatures below T_c. Indeed, in the latter case, the interactions, due to the high atomic densities, modify the low energy spectrum and must be taken into account. Following the Hartree-Fock-Bogoliubov (HFB) treatment developed in [65] we can write the entropy of a Bose gas as

$$
S = k_B \int \frac{d\mathbf{r}\,d\mathbf{p}}{(2\pi\hbar)^3} \left(\frac{\epsilon(\mathbf{r}, \mathbf{p})}{k_B T(e^{\epsilon(\mathbf{r},\mathbf{p})/k_B T} - 1)} - \log(1 - e^{\epsilon(\mathbf{r},\mathbf{p})/k_B T}) \right),
\tag{4.6}
$$

with the energy of the elementary excitations ϵ defined by:

$$
\epsilon(\mathbf{r}, \mathbf{p}) = \left(\left(\frac{p^2}{2m} + V_{ext}(\mathbf{r}) - \mu + 2gn(\mathbf{r}) \right)^2 - g^2 n_0^2(\mathbf{r}) \right)^{1/2},
\tag{4.7}
$$

where n_0 is the condensate density. In our experimental circumstances, comparing the results obtained with the numerical evaluation of eq. (4.6) with those calculated with eq. (4.5) for $T \leq T_c$ we find that the interactions increase the ideal gas value of the entropy by at most 20% for partially condensed samples. An easy-to-use expression that well approximates the HFB results can be obtained by expressing (T/T_c) in eq. (4.5) in terms of the thermal fraction $1 - f_c$, with f_c being the condensed fraction obtained from the semi-ideal model of [66]:

$$
f_c = 1 - \left(\frac{T}{T_c}\right)^3 - \eta\frac{\zeta(2)}{\zeta(3)}\left(\frac{T}{T_c}\right)^2 \left[1 - \left(\frac{T}{T_c}\right)^3\right]^{2/5},
\tag{4.8}
$$

where $\eta = \mu/k_B T$ and $\mu = (\hbar\omega/2)(15Na/a_{ho})^{2/5}$, with $a_{ho} = \sqrt{\hbar/m\omega}$ the harmonic oscillator length. With our experimental parameters η varies in the range $(0.3, 0.33)$. To consider the total entropy of the mixture we simply add the single species contributions, $S = S_K + S_{Rb}$, neglecting the interspecies interactions. This approximation is valid since, in our experimental scheme, one of the two samples is always thermal.
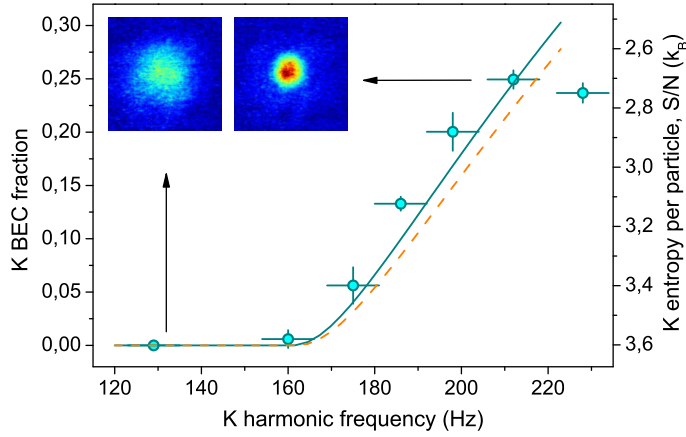
Figure 4.2: BEC fraction of the K atomic sample as a function of the K harmonic frequency at the end of the selective compression. Data are compared to the theoretical predictions based on numerical (solid line) and analytical (dashed line) solutions of eq. (4.9). On the right axes is reported the approximate value $S/(Nk_B) = 4[\zeta(4)/\zeta(3)](1 - f_c)$. The insets show absorption images of the K sample before and after the selective compression.

In fig. 4.2 it is shown that, driven by the selective compression, a sample of 2×10^5 K atoms at 410(15) nK crosses the BEC transition, indicating that its entropy clearly drops. The compression is made with the K cloud in thermal contact with a Rb sample of 9.5×10^5 atoms. We can compare our data with the theoretical predictions supposing that, since the compression $\omega_{K,i} \rightarrow \omega_{K,f}$ is adiabatic, the total entropy of the system does not vary during the compression, i.e.,

$$S_K(T_i, \omega_{K,i}, N_K) + S_{Rb}(T_i, \omega_{Rb}, N_{Rb}) = S_K(T_f, \omega_{K,f}, N_K) + S_{Rb}(T_f, \omega_{Rb}, N_{Rb}), \quad (4.9)$$

where T_i and T_f are the initial and final temperature, respectively. In our experimental circumstances the Rb sample is always thermal, hence the expression of S_{Rb} will be the one for $T \geq T_c$. Conversely, the K sample starts from just above the BEC threshold and during the compression it experiences the Bose-Einstein condensation, for this reason we use for S_K the expression for $T \leq T_c$. With this assumptions eq. (4.9) can be numerically solved for T_f and the K condensed fraction can be computed through eq. (4.8); the results are shown in Fig. 4.2.

We also find an analytical approximate solution for T_f simply truncating all the $g_i(z)$ series at the linear term so that for the Rb thermal samples $S_{Rb} = Nk_B(4 -$
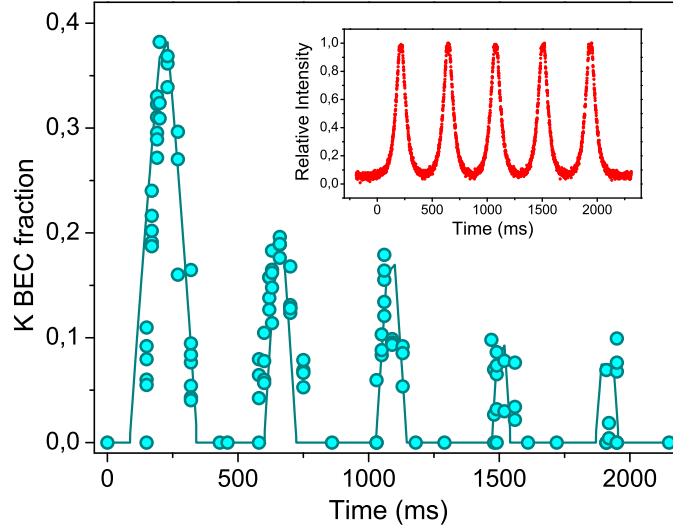
Figure 4.3: Cycles of selective compressions and decompressions on the K sample. The K condensate fraction changes in a reversible manner as we modulate the K harmonic frequency over time from 128 to 216 Hz. The solid line is obtained from the analytical eqs. (4.10) and (4.8). The inset shows the relative intensity of the SSDP beam.

$\log[N(\hbar\omega/k_B T)^3])$. With this approximation from eq. (4.9) one can find that

$$T_f = T_i \frac{\omega_{K,f}}{\omega_{K,i}} \left\{ W \left[\left(\frac{\omega_{K,i}}{\omega_{K,f}} \right)^3 \xi e^\xi \right] \frac{1}{\xi} \right\} \quad (4.10)$$

with $\xi = 4\zeta(4)(k_B T_i/\hbar\omega_{K,i})^3/N_{Rb}$ and $W(y)$ is the Lambert's function defined as the inverse of $y = xe^x$. The analytical results obtained with eqs. (4.10) and (4.8) are also shown in Fig. 4.2.

The degree of reversibility of the selective transformations across the K BEC threshold can be investigated performing multiple compression and decompression cycles. The intensity of the SSDP beam is repeatedly ramped up and down with a period of 0.43 s and with exponential ramps with $\tau = 45$ ms. As shown in Fig. 4.3 the BEC threshold for a sample of 2×10^5 K atoms can be crossed at least five times at maximum compression. The K condensate fraction decreases over successive compressions because, at each cycle, the number of Rb atoms is reduced and the temperature slightly increased. This is due to the fact that, even in absence of compression, our Rb sample experiences a heating rate of the order of 0.7 μK/s which we reduce by an order of magnitude by means of a microwave
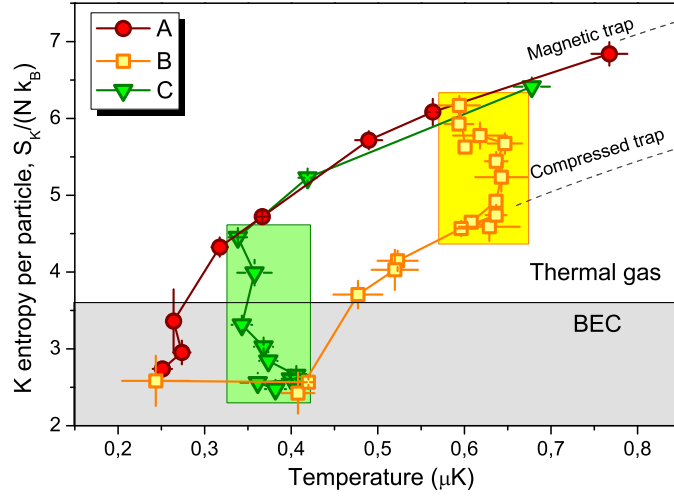
Figure 4.4: Trajectories in the entropy-temperature diagram of the K sample. For the experimental data the entropy is determined with the formulas in text. The dashed lines show the ideal entropy for a sample of 1.1×10^5 K atoms at the harmonic frequencies of the magnetic trap ($\omega_K = 2\pi \times 128$ Hz) and of the combined magnetic and SSDP maximally compressed trap ($\omega_K = 2\pi \times 216$ Hz). The shaded boxes highlight the isothermal SSDP compressions.

shield, removing trapped Rb atoms with energy $E/k_B > 5.5\mu$K. As a consequence, the Rb atom number decreases at a rate of $2.5(5) \times 10^5$ s^{-1}. Thus, starting with approximately 8.5×10^5 Rb atoms, after 2 s only 3×10^5 of them are still in the trap. For this reason, after 5 cycles, the entropy exchange still occurs, but its efficiency is undermined by the lower Rb atom number and the higher temperature before the compression. Also in this case experimental data can be reproduced by the analytical eqs. (4.10) and (4.8), as reported in Fig. 4.3, provided we take into account that successive cycles occur from different initial conditions.

Exploiting the interspecies exchange of entropy we can also explore the whole entropy-temperature diagram for the K sample. Indeed, we can manipulate the harmonic potential and the temperature of a sample of $1.1(2) \times 10^5$ K atoms in presence of the Rb auxiliary gas. This allows us to perform (quasi)isoentropic as well as (quasi)isothermal transformations on the K sample, as shown in Fig. 4.4. At each data point, the entropy of the gas is determined in the following way: above T_c, we compute the entropy per particle by the formula $S/Nk_B = 4 - \log[N(\hbar\omega/k_BT)^3)]$ obtained by truncating the polylogarithmic functions at the first order in z; be-
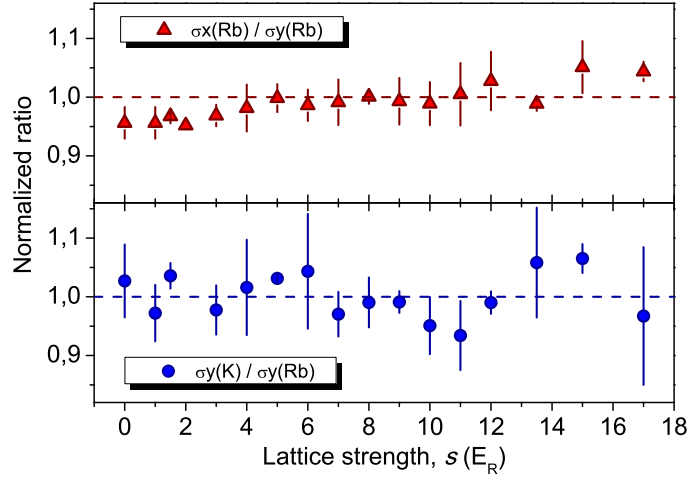
Figure 4.5: Ratio of the x-to-y rms sizes of Rb (upper) and K-to-Rb y rms sizes (lower). The cloud sizes are measured after species-dependent time-of-flight (see text); the lattice strength is in units of K recoil energy. The constant ratio in lower panel indicates that the temperatures of the two species are locked.

low T_c, we calculate the entropy from the measured condensate fraction $S/Nk_B = 4[\zeta(4)/\zeta(3)](1 - f_c)$.

By combining sympathetic cooling and control of the harmonic frequencies, we can follow different trajectories in the S-T diagram. In particular, we compare the efficiency of three trajectories indicated as A, B, C in Fig. 4.4. Trajectory A corresponds to plain sympathetic cooling in the magnetic trap. Along B, instead, we raise the SSDP beam to maximum power when the temperature of the samples reaches 600 nK, and we proceed with evaporation of Rb and sympathetic cooling of K. When the Rb is exhausted, at 410 nK, we extinguish the SSDP beam intensity, thus decompressing the trapping potential, and reach the same final point of the previous trajectory. Finally along C, we raise the SSDP when the K sample is close to BEC at 340 nK and cross threshold by selective compression as in Fig. 4.2. The end point of all trajectories is reached when the Rb sample is either exhausted (B) or depleted to the point that further sympathetic cooling is inefficient, $N_{Rb}/N_K \sim 2$ (A, C). The three described paths have similar efficiencies, since the end values of entropy are approximately equal. Obviously the efficiency strongly depends on N_{Rb}/N_K; in particular, for higher values of this ratio, the Rb sample tends to be a more efficient thermal bath and lower values of S_K/N_K can be reached.

The entropy exchange between two atomic species as well as the independent manipulation of them open also new perspectives for the thermometry of cold gases in optical lattices. Indeed, as a first application, we have investigated the thermalization of the two species when the SSDP forms a 1D lattice for K only. For this purpose we shine the SSDP beam along the x weak axis of the magnetic trap retro-reflecting it. The SSDP beam intensity is ramped in 200 ms, kept constant for 20 ms and then linearly extinguished in 1 ms. The magnetic trap is abruptly switched off immediately afterwards and the atoms expand freely for 10 ms (K) and 15 ms (Rb). We observe that the size of the Rb cloud in the x and y directions do not depend on the SSDP lattice depth and either can be used to extract the gas temperature (see Fig. 4.5). We also find that the K temperature obtained from the y size slightly increases with the lattice strength, but it is always equal to Rb within our statistical uncertainty of 10%. This shows that, in a 1D lattice configuration, up to a strength of 20 recoil energy, the auxiliary gas can be used to read out the system temperature and to validate proposed methods to extract the temperature of a gas in an optical lattice, such as the recent analysis of Ref. [67].

4.2   Mixtures in Mixed 2D-3D Dimensions

The idea that we are living in an universe which allows the existence of more dimensions than the ones we can experience dates back to the first years of the last century, when the impressive Einstein's work on the special relativity [68] put the time on the same footing of the spatial dimensions. In the following decades many fascinating theories expecting the appearance of extra-dimensions were formulated and, in particular, in the last years, a great effort was made in the development of the so-called M theory [69]. This theory predicts that the observable universe could be a $(1 + 3)$-surface (the *brane*) embedded in a $(1 + 3 + d)$-dimensional space-time (the *bulk*), with particles and fields trapped on the brane, while gravity is free to access the bulk.

What makes the field of ultracold atoms truly exceptional is the unique possibility to explore and simulate widely different physical systems having an almost total control on all the experimental parameters. In particular, with our setup, we have the chance to experimentally study and access, for the first time, a system where a 2D object interacts with a 3D object; the key tool is the species-selective dipole potential.

Once the mixture in the $|1, 1\rangle$ state is cooled in the optical trap at the desired

temperature we shine on the atoms, along the x direction, the SSDP beam, retro-reflecting it. Thus we create a SSDP optical lattice that is not experienced by the Rb atoms. Optical lattices have proven to be an useful and flexible tool to create arrays of 2D pancakes, indeed they are widely used in almost all the experiments devoted to the study of low-dimensional systems [70, 71].

A gas confined in a harmonic trap with frequency ω can be considered 2D once two conditions are fulfilled:

- *Energetic condition*: $\hbar\omega \gg k_B T$

- *Collisional condition*: $a \gg \sqrt{\hbar/(m\omega)}$.

In our experimental circumstances, for an height of the SSDP optical lattice of $10E_R^K$ (that, as we will see in the following is the lowest we employ), we have that in each lattice site $\omega \simeq 2\pi \times 49$ kHz for the K atoms. Hence, the K sample is energetically 2D if $T \ll 2.4\mu$K and collisionally 2D if $a \gg 1400a_0$. We will see in the following that the energetic condition is fulfilled in our experiment cooling the atoms to 100 nK while the collisional condition will not, since $a_K = 63a_0$. We must notice, however, that the collisional condition is never completely fulfilled in cold atoms experiments in 2D. Since we are dealing with optical lattices there is another condition that must be kept into account: the tunnelling time between sites must be bigger than the experiment time. For an height of the lattice of $10E_R^K$ the tunnelling time is $\sim$7 ms. This condition is not completely fulfilled in our experimental circumstances since we must hold the atoms for some tens of milliseconds in order to let them decay via inelastic collisions. We will see in the following that the finite tunnelling between sites must be taken into account to slightly modify the theory.

When the SSDP optical lattice is applied to the atoms the K sample is separated in many 2D layers while the Rb sample remains 3D. In this way we create a system of interacting objects with different dimensions. The ability to tune at will the interspecies scattering length via the magnetic field allows us to perform an extensive analysis on the inter-dimensional interactions. Moreover, for this system, many inter-dimensional features are predicted to appear [72] as inter-dimensional Feshbach resonances. In the following I present the exact theory from Y. Nishida [73] about this system and compare it with our experimental data.

Theoretical Model

Let us consider a system composed by two interacting particles where one of the two is confined by a one dimensional harmonic potential; the Schrödinger equation is

$$\left[-\frac{\hbar^2}{2m_1}\nabla^2_{\mathbf{r}_1} - \frac{\hbar^2}{2m_2}\nabla^2_{\mathbf{r}_2} + \frac{1}{2}m_1\omega^2 x_1^2 + gV \right] \psi(\mathbf{r}_1, \mathbf{r}_2) = E\psi(\mathbf{r}_1, \mathbf{r}_2) \qquad (4.11)$$

where the interaction is given by the pseudo-potential

$$\begin{aligned} V\psi(\mathbf{r}_1, \mathbf{r}_2) &= \tilde{a}(E_c)\delta(\mathbf{r}_1 - \mathbf{r}_2)\frac{\partial}{\partial|\mathbf{r}_1 - \mathbf{r}_2|}[|\mathbf{r}_1 - \mathbf{r}_2|\psi(\mathbf{r}_1, \mathbf{r}_2)] \\ &\equiv \delta(\mathbf{r}_1 - \mathbf{r}_2)\psi_{reg}(\mathbf{r}_1, \mathbf{r}_2), \end{aligned} \qquad (4.12)$$

whose strength is $g = 2\pi\hbar^2/\mu$, with μ being the reduced mass. Here we have also defined the energy-dependent scattering length $\tilde{a}(E_c)$.

Because of the translational symmetry in the $y - z$ plane we can eliminate the center of mass motion in the plane such that the Schrödinger equation reduces to

$$\left[-\frac{\hbar^2}{2\mu}\nabla^2_{\mathbf{r}} - \frac{\hbar^2}{2m_1}\nabla^2_{x1} - \frac{\hbar^2}{2m_2}\nabla^2_{x2} + \frac{1}{2}m_1\omega^2 x_1^2 + gV \right] \psi(\mathbf{r}, x_1, x_2) = E\psi(\mathbf{r}, x_1, x_2), \qquad (4.13)$$

where $\mathbf{r} = (y_1 - y_2, z_1 - z_2)$. The general solution of this equation can be written as [73]

$$\psi(\mathbf{r}, x_1, x_2) = \psi_0(\mathbf{r}, x_1, x_2) + g\int_{-\infty}^{\infty} dx' G_E(\mathbf{r}, x_1, x_2; \mathbf{0}, x', x')\psi_{reg}(x') \qquad (4.14)$$

where ψ_0 is the solution of the non-interacting Schrödinger equation and G_E is the two particle retarded Green's function defined as

$$G_E(\mathbf{r}, x_1, x_2; \mathbf{r}', x_1', x_2') = \langle \mathbf{r}, x_1, x_2| \frac{1}{E - H_0 + i\delta} |\mathbf{r}', x_1', x_2'\rangle. \qquad (4.15)$$

To obtain an explicit expression for the ψ we can look at the large and short distance behaviours of the wave function. Indeed, in the long distance limit, the Green's function (4.15) has the following representation [73]

$$G_E(\mathbf{r}, x_1, x_2; \mathbf{r}', x_1', x_2') =$$

$$-\frac{2\mu\sqrt{2m_2}}{\hbar^2}\sum_n \frac{e^{-\sqrt{(1/2+n)\hbar\omega - E - i\delta}\sqrt{\frac{2\mu(\mathbf{r}-\mathbf{r}')^2}{\hbar^2} + \frac{2m_2(x_2-x_1)^2}{\hbar^2}}}}{4\pi\sqrt{2\mu(\mathbf{r} - \mathbf{r}')^2 + 2m_2(x_2 - x_1)^2}}\phi_n(x_1)\phi_n^*(x_1'), \quad (4.16)$$

where $\phi_n(x)$ are the wave functions of the 1D harmonic oscillator with mass m_1 defined as

$$\phi_n(x) = \frac{1}{\sqrt{2^n n!}}\left(\frac{m_1\omega}{\pi\hbar}\right)^{1/4} e^{-\frac{m_1\omega}{2\hbar}x^2} H_n\left(\sqrt{\frac{m_1\omega}{\hbar}}x\right), \qquad (4.17)$$

with H_n being the Hermite polynomials. In the "zero-energy" limit $E \to \hbar\omega/2$ the wave function thus becomes

$$\psi(\mathbf{r}, x_1, x_2) = C\phi_0(x_1) - \int_{-\infty}^{\infty} dx' \sum_n \frac{e^{-\sqrt{n\hbar\omega}\sqrt{\frac{2\mu r^2}{\hbar^2} + \frac{2m_2(x_2-x')^2}{\hbar^2}}}}{\sqrt{\frac{\mu}{m_2}r^2 + (x_2 - x')^2}} \phi_n(x_1)\phi_n^*(x')\psi_{reg}(x'),$$

(4.18)

where we exploited the fact that when $E \to \hbar\omega/2$ the non-interacting wave function is the product of the wave function in the ground state of the harmonic oscillator and the wave function of two free particles. In the asymptotic region $r \to \infty$ and $(x_1 - x_2) \to \infty$ it remains only the lowest term of the above sum, i. e.,

$$\psi(\mathbf{r}, x_1, x_2) = \phi_0(x_1)\left[C - \frac{1}{\sqrt{\frac{\mu}{m_2}r^2 + x_2^2}}\int_{-\infty}^{\infty} dx'\phi_0^*(x')\psi_{reg}(x')\right],$$

(4.19)

from which we can define an effective scattering length as

$$a_{eff} = \sqrt{\frac{m_2}{\mu}}\frac{1}{C}\int_{-\infty}^{\infty} dx'\phi_0^*(x')\psi_{reg}(x').$$

(4.20)

To eliminate the unknown coefficient C from the previous equation we have to look at the short distance behaviour of the wave function. Indeed when $R = \sqrt{r^2 + (x_1 - x_2)^2} \to 0$ the left-hand side of eq. (4.14) becomes

$$\psi(\mathbf{r}, x_1, x_2) \to \left[\frac{1}{\tilde{a}(E_c)} - \frac{1}{R}\right]\psi_{reg}(x)|_{x=x_1=x_2} = \left[\frac{1}{a} - \frac{\mu r_0 \hat{E}_c}{\hbar^2} - \frac{1}{R}\right]\psi_{reg}|_{x=x_1=x_2},$$

(4.21)

where we have exploited the following definition of the energy-dependent scattering length

$$\frac{1}{\tilde{a}(E_c)} = \frac{1}{a} - \frac{\mu r_0 E_c}{\hbar^2},$$

(4.22)

with r_0 the effective range of the interaction potential and $\hat{E}_c$ the energy operator defined as

$$\hat{E}_c = E + \frac{\hbar^2 \nabla_x^2}{2(m_1 + m_2)} - \frac{1}{2}m_1\omega^2 x^2.$$

(4.23)

Hence, in the "zero-energy" limit $E \to \hbar\omega/2$,

$$\psi(\mathbf{r}, x_1, x_2) \to \left[\frac{1}{a} - \mu r_0\left(\frac{\omega}{2} + \frac{\hbar^2 \nabla_x^2}{2(m_1 + m_2)} - \frac{1}{2}m_1\omega^2 x^2\right) - \frac{1}{R}\right]\psi_{reg}|_{x=x_1=x_2}. \quad (4.24)$$

The right-hand side of eq. (4.14) can be instead written as

$$C\phi_0(x) + g\psi_{reg}(x)\int_{-\infty}^{\infty} dx' G_0(\mathbf{r}, x_1, x_2; x')|_{R\to 0} +$$

$$+ g\int_{-\infty}^{\infty} dx' G_0(\mathbf{0}, x, x; x')[\psi_{reg}(x') - \psi_{reg}(x)]$$

(4.25)

so that, in the "zero-energy" limit $E \to \hbar\omega/2$ we can obtain the following equation for the ψ_{reg}:

$$\psi_{reg}(x) = C\phi_0(x) + F_1(x)\psi_{reg}(x) + \int_{-\infty}^{\infty} dx' F_3(x, x')[\psi_{reg}(x') - \psi_{reg}(x)] \quad (4.26)$$

where, exploiting the following representation of the Green's function [73]

$$G_E(\mathbf{r}, x_1, x_2; \mathbf{r}', x_1', x_2') = -\int_0^{\infty} d\tau \frac{\mu}{2\pi\hbar^3\tau} \sqrt{\frac{m_1\omega e^{\omega\tau}}{2\pi \sinh(\omega\tau)}} \sqrt{\frac{m_2}{2\pi\tau}} \times$$

$$\times e^{\left[-\frac{\mu}{2\hbar\tau}(\mathbf{r}-\mathbf{r}')^2 - \frac{m_1\omega}{2\hbar} \frac{(x_1^2+x_1'^2)\cosh(\omega\tau) - 2x_1 x_1'}{\sinh(\omega\tau)} - \frac{m_2}{2\hbar\tau}(x_2 - x_2')^2 \right]}, \quad (4.27)$$

we have defined

$$F_1(x) = \sqrt{\frac{\mu}{2\pi\hbar}} \int_0^{\infty} \frac{d\tau}{\tau^{3/2}} \left[1 - \sqrt{\frac{(m_1+m_2)e^{\omega\tau}}{m_1\cosh(\omega\tau) + m_2 \frac{\sinh(\omega\tau)}{\omega\tau}}} \times \right.$$

$$\left. \times \exp\left(-\frac{x^2}{\hbar\tau} \frac{m_1 m_2(\cosh(\omega\tau) - 1) + m_1^2\omega\tau\sinh(\omega\tau)/2}{m_1\cosh(\omega\tau) + m_2\sinh(\omega\tau)/(\omega\tau)} \right) \right] \quad (4.28)$$

and

$$F_3(x, x') = -\int_0^{\infty} \frac{d\tau}{2\pi\hbar\tau} \sqrt{\frac{m_1 m_2 \omega e^{\omega\tau}}{\tau \sinh(\omega\tau)}} \times$$

$$\times \exp\left[-\frac{m_1\omega}{2\hbar} \frac{(x^2 + x'^2)\cosh(\omega\tau) - 2xx'}{\sinh(\omega\tau)} - \frac{m_2}{2\hbar\tau}(x - x')^2 \right]. \quad (4.29)$$

We can now expand the wave function ψ_{reg} in the basis of the wave functions of the 1D harmonic oscillator with mass m_1:

$$\psi_{reg}(x) = \sum_{j=0}^{\infty} b_j \phi_j(x) \quad (4.30)$$

and, inserting eq. (4.20) in eq. (4.26), we can eliminate the unknown coefficient C obtaining the following eigenvalues equation

$$\frac{1}{a}b_i - \tilde{M}_{ij}b_j = \left[\frac{1}{a_{eff}}\sqrt{\frac{m_2}{\mu}}\delta_{0i}\delta_{0j} + M_{ij} \right] b_j \quad (4.31)$$

where

$$\tilde{M}_{ij} = \mu r_0 \int_{-\infty}^{\infty} dx \phi_i^*(x) \left[\frac{\hbar\omega}{2} + \frac{\hbar^2\nabla_x^2}{2(m_1+m_2)} - \frac{1}{2}m_1\omega^2 x^2 - \frac{1}{R} \right] \psi_{reg}|_{x=x_1=x_2} \quad (4.32)$$

and

$$M_{ij} = \int_{-\infty}^{\infty} dx \phi_i^*(x) F_1(x)\phi_j(x) + \int_{-\infty}^{\infty} dx dx' \phi_i^*(x) F_3(x, x')[\phi_j(x') - \phi_j(x)]. \quad (4.33)$$

Eq. (4.31) can be numerically solved once the masses of the two atoms and the harmonic frequency are known. In our case $m_1 = m_K$ and $m_2 = m_{Rb}$ while the harmonic frequency in each well of the SSDP lattice is given by $V_{lat}(x) = sE_R \sin^2(k_{lat}x) \simeq sE_R k_{lat}^2 x^2 = m_K \omega^2 x^2/2$, hence $\omega = \sqrt{s}4\pi^2\hbar/(\lambda_{SSDP}^2 m_K)$. Inserting the experimental parameters in eq. (4.31) we can calculate the dependence of a_{eff} on a and therefore, on the B field. To extract an analytical dependence of a on the B field we fit the curve of Fig. 3.1 with an empirical formula that implies the existence of another Feshbach resonance in the range of negative values[1] of B, finding that

$$a(B) = 208a_0 \left(1 + \frac{30.9}{B + 38.52} - \frac{49.92}{B - 38.37} - \frac{1.64}{B - 78.67} \right). \tag{4.34}$$

Another unknown parameter is the effective range of the interaction potential r_0. This can be evaluated fitting the measured binding energy with [74]

$$E_b = -\frac{1}{\mu r_0^2} \left(1 - \frac{r_0}{a} - \sqrt{1 - 2\frac{r_0}{a}} \right). \tag{4.35}$$

For the low-field Feshbach resonance we find that $r_0 = 168.373 \times a_0$.

The results of the numerical calculations for $B < 50$ G are shown in Fig. 4.6 for different values of the lattice depth. The same scenario occurs also around the high-field Feshbach resonance but, experimentally, it is convenient to investigate the 2D-3D physics around the low-field resonance since there the scattering length varies smoothly with the magnetic field. Hence the inter-dimensional features are expected to be broader for the low-field resonance with respect to the high-field resonance.

The appearance of the inter-dimensional resonances can be qualitatively understood looking at Fig. 4.7: the 1D harmonic confinement of the K atoms shifts the atomic threshold by a quantity $\hbar\omega/2$, that is the zero-point energy of the harmonic oscillator with mass m_K. Also the molecules experience the harmonic confinement induced by the SSDP lattice, this implies that their energy is shifted as well, this time by a quantity $\hbar\omega_{KRb}/2 = \hbar\sqrt{m_K/(m_K + m_{Rb})}\omega/2$. Therefore the shifted binding energy intercepts the shifted atomic threshold in a different position with respect to the full-3D case. In particular, since $\omega_{KRb} < \omega$, the 2D-3D resonance is expected to occur for higher magnetic field values. The same picture repeats for every molecular harmonic level, whose separation is $\hbar\omega_{KRb}$, thus implying the appearance of

---

[1]The existence of a Feshbach resonance in the range of negative values of B is equivalent at the existence of a Feshbach resonance for the $|1, -1\rangle$ state in the range of positive values of the B field. Indeed a resonance in this state is predicted from the collisional model of [24], even if in a slightly different position with respect to the one given by our fit.
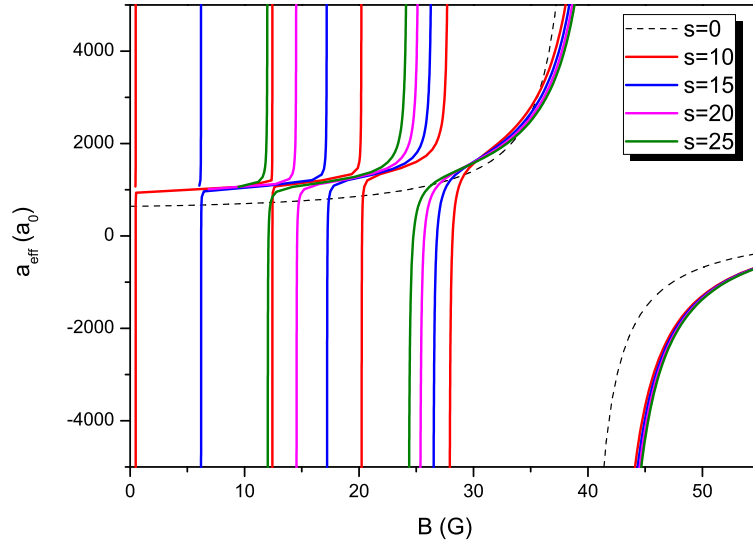
Figure 4.6: Effective scattering length a_{eff} for our inter-dimensional system as a function of the magnetic field. Numerically evaluated curves for different values of the lattice depth s are shown, together with the theoretical curve in the full-3D case (dashed line).

other resonances for lower B field values. Thus, in this approximate picture, we can write that an inter-dimensional resonance appears for any integer n that satisfies the following equation:

$$\left(n + \frac{1}{2}\right)\sqrt{\frac{m_K}{m_K + m_{Rb}}}\hbar\omega - E_b = \frac{1}{2}\hbar\omega. \tag{4.36}$$

The treatment above is made considering a single 2D disk of K atoms. In our experimental setup we employ an optical lattice thus the number of 2D disks is much larger than one ($\sim$1100) and we must consider the finite tunnelling between the lattice sites. For this reason we have to slightly modify the 1-disk results to include the lattice physics in our theory. It is well-known that a particle in a periodic potential obeys the Bloch theorem and its wave function $\Psi_{q,n}$ is a plane wave modulated by a function having the same periodicity of the lattice. These Bloch wave functions are labelled by two quantum numbers: the band index n and the quasimomentum q. For a given quasimomentum q many different solutions with different energies $E_n(q)$ exist. These solutions are identified with the band index n, indeed the periodic potential causes a segmentation of the energy spectrum into allowed and forbidden zones, the so-called energy bands. Hence, in our experimental circumstances, we have to think in terms of bands instead that of harmonic oscillator levels and the
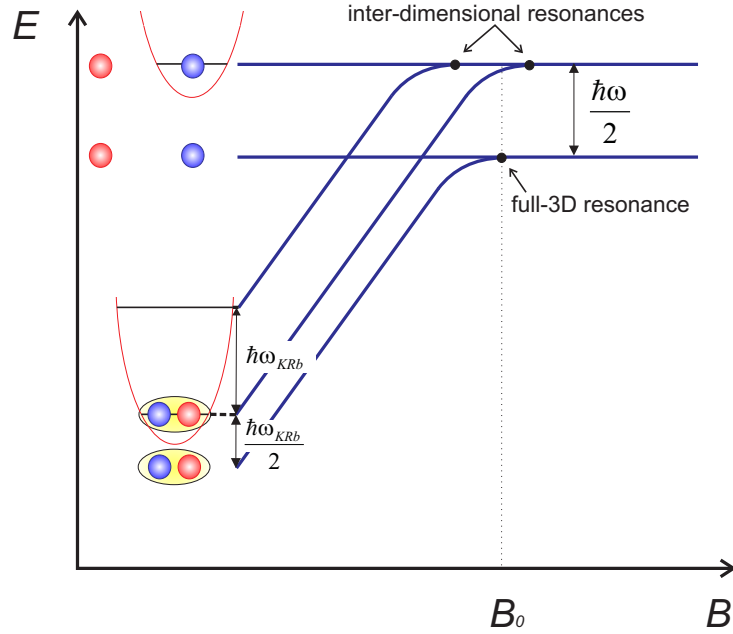
Figure 4.7: Pictorial representation of the 2D-3D scenario around a 3D Feshbach resonance. Due to the harmonic confinement induced by the SSDP lattice the atom threshold and the energy of the dimers are shifted by $\hbar\omega/2$ and $\hbar\omega_{KRb}/2$ respectively (see text). For this reason the resonance in the 2D-3D configuration is shifted with respect to the full-3D case. Additional inter-dimensional resonances appear any time an excited molecular harmonic level intercepts the 2D-3D threshold.

scenario depicted in Fig. 4.6 changes according to the band treatment. In particular, referring to Fig. 4.7, every energetic level broadens and moves according to the Bloch analysis and eq. (4.36) becomes

$$E_n^{KRb} - E_b = E_0^K. \tag{4.37}$$

The Bloch bands can be easily calculated projecting the Bloch waves on the free-particle base: $\Psi_{q,n}(x) = \sum_j a_j \exp(-i(q + 2jk)x)$. The presence of many 2D disks make the system "less" 2D because there is a finite tunnelling between them, but, as we will see in the following, experimental data nicely agree with the inter-dimensional analysis here reported, hence we can state that we still deal with a mixed-dimensional system.

Detection of Inter-Dimensional Feshbach Resonances

Our experimental procedure for the detection of the positions of the inter-dimensional Feshbach resonances is the following: we evaporatively cool the mixture in the $|1, 1\rangle$ state to ~ 100 nK in the proximity of the low-field zero-crossing in 3 s and, when the evaporation is finished, we ramp the B field on the side of positive scattering length of the low-field Feshbach resonance, at 15.7 G. Then we adiabatically ramp up the SSDP optical lattice at the selected height in 50 ms. We have chosen this procedure in order to cross the low-field Feshbach resonance always in the same configuration, i.e., without the SSDP optical lattice. This ensures that the initial conditions are the same for any height of the optical lattice. The beam, linearly polarized, with a waist of 90 μm, propagates along the x direction. We experimentally determine the wavelength value to be 790.02(1) nm, by minimizing the efficiency of the Raman-Nath diffraction caused by a pulsed standing wave on a Rb condensate. With the same technique we also measured the residual potential acting on Rb to be $V_{Rb}/V_K \simeq 0.01(1)$.

Once the mixture is loaded in the inter-dimensional configuration, we set the magnetic field at the desired value in 20 ms and we hold the atoms for a certain time t_h. At the end of the hold time we ramp down the SSDP lattice intensity in 1 ms and we abruptly switch off the trap and the B field. We detect the remaining atoms by means of the usual absorption imaging technique on the expanding clouds. Also in this case our main observable is the total number of remaining atoms $N(t_h) = N_K(t_h) + N_{Rb}(t_h)$.

As reported in Fig. 4.8 we observe several inter-dimensional Feshbach resonances for different values of the lattice height s. For convenience, here and in the following, the height of the lattice is measured in unit of the K recoil energy $E_R^K = \hbar^2 k_{lat}^2/(2m_K)$; the corresponding s_{KRb} for the molecules is a factor $m_K/(m_K + m_{Rb})$ smaller. Since these resonances are not observable in the full-3D system or with single species samples we can state that they are genuine inter-dimensional features.

We are able to detect a complete series of resonances corresponding to the $n = 0, 1, 2, 3$ bands of the molecular spectrum for $s = 10$ and $s = 20$ and incomplete series, corresponding to the $n = 1, 2, 3$ and $n = 0, 1, 3$ bands, for $s = 15$ and $s = 25$ respectively. For $s = 20$ and $s = 25$ we also observe a resonance corresponding at the $n = 4$ band, not reported in Fig. 4.8.

The widths of the resonances depend strongly on the band index n and weakly on the height of the SSDP lattice s. For every height of the SSDP lattice, a broad
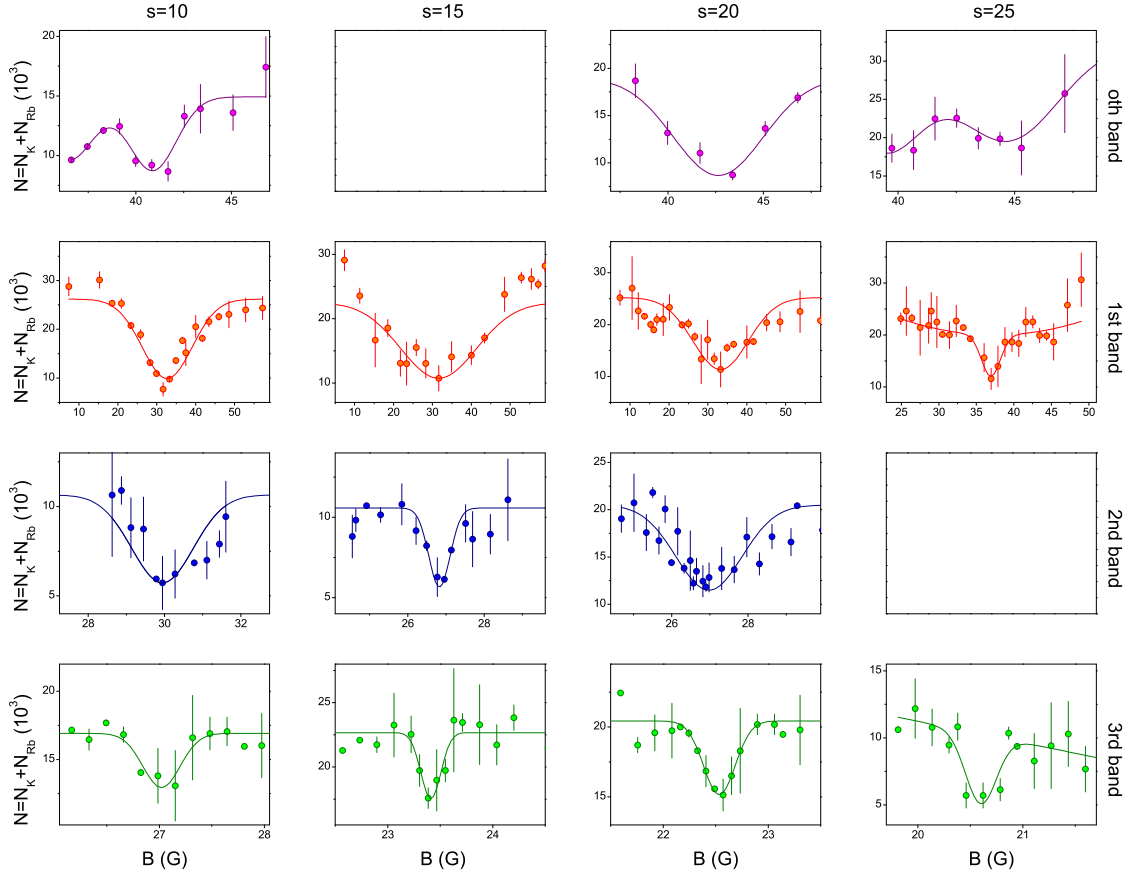
Figure 4.8: Peaks of inelastic atomic losses due to inter-dimensional Feshbach resonances. Each column corresponds to a given height of the SSDP lattice (in unit of the K recoil energy) while each row corresponds to a given band of the molecular spectrum. For each resonance a Gaussian fit is performed. Please note the dependence of the horizontal and vertical scales with the band index.

resonance with a width (FWHM) of $\sim$23.5 G, comparable to the one of the full-3D resonance, appears. The center of this resonance corresponds to the one expected in the first band, hence we assign it to the $n = 1$ band. The resonances corresponding at the $n = 0$ band are narrower, with a width of $\sim$6 G, and those corresponding at the $n = 2$ and $n = 3$ bands have widths of the order of $\sim$2.5 G and $\sim$0.6 G, respectively. Also the strengths of the resonances depend mostly on the band index and follow the same behaviour of the widths, hence the resonances are progressively weaker for the $n = 1, 0, 2, 3$ bands. The widths and the strengths of the resonances depend on the coupling of the molecular levels in the nth band with the atomic threshold in the 0th band. From our measurements the coupling of the $n = 1$ band
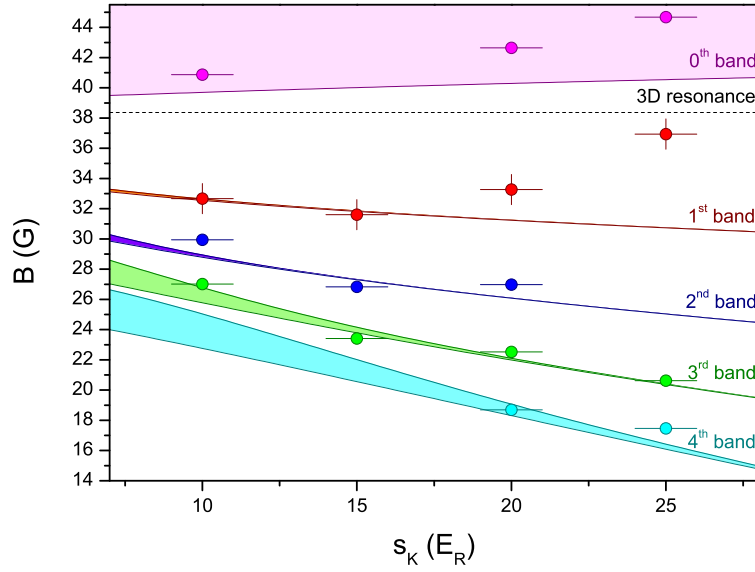
Figure 4.9: Position of inter-dimensional resonances as a function of the height of the SSDP lattice (in unit of K recoil energy). Data (dots) are compared with the predicted bands (shaded areas), calculated by means of eq. (4.37).

is the strongest, then, in decreasing order, there are the couplings of the $n = 0, 2, 3$ bands. At the moment it is still unclear how to calculate this couplings.

In Fig. 4.9 are reported the position of the observed resonances with the theoretical calculations of the bands, according to eq. (4.37). The experimental data agree with the theoretical predictions, indeed the dependence of these positions as a function of the magnetic field and of the height of the SSDP lattice reflects the expected behaviour. For what concerns the 0th band we can only give a lower limit since the extension of the binding energy above the 3D atomic threshold is unknown (see Fig. 4.7). We calculate this limit extending the linear part of the binding energy until it crosses the atomic threshold in the 0th band. Then we calculate the shift of the linear extension with respect of the real trend in the full-3D regime and we add this shift also in the mixed-dimensional regime.

4.3 A Matter Wave in a Matter Grating

Bose-Einstein condensates in optical lattices have proven to be a versatile tool for investigating fundamental issues of quantum mechanics, solid state physics, nonlinear systems and superfluidity [75, 76]. Already in 1D, and in the mean field regime, the dynamics of BECs in a periodic potential presents non-trivial features

emerging from the interplay of non-linearity, arising from atomic interactions, and the discrete translational invariance of the lattice. Noticeable features are the formation of solitonic structures [77, 78] and the presence of several kinds of instabilities [79, 80, 81, 82, 83, 84, 85, 86, 87]. In particular, the dynamical instability of non-linear Bloch waves in the flow of a BEC in a 1D optical lattice has been carefully explored. This phenomenon is characterized by the exponential growth of arbitrarily small fluctuations that may lead to a partial or complete destruction of the condensate [79, 83, 85] or to the occurrence of a pulsating behaviour [86, 87], depending on the interaction regime. Recently, also instabilities of two component BECs have been investigated theoretically [88, 89, 90], and first experiments with two BECs in an optical lattice have been realized in our experiment [91].

All the studies performed so far, however, have been restricted to the case where the periodic potential is not perturbed by the condensate flow, since optical lattices cannot support excitations. Different scenarios may occur instead when excitations of the lattice interact with that of the condensate, like electrons and phonons in a crystal lattice. This condition can be realized, for example, by considering a two component BEC system, where one of the two condensates is periodically modulated by an external optical potential, playing the role of a periodic lattice, where the other condensate (transparent to the optical potential) flows through. As for the previous section, this configuration can be designed experimentally exploiting the optical lattice produced by the species-selective dipole potential.

Let us consider a one-dimensional system composed by a mixture of two interacting bosonic species at zero temperature, with the second species being immersed in a SSDP optical lattice. At the meanfield level, as it was explained in chapter 1, this system can be described by two coupled 1D Gross-Pitaevskii equations [64, 92, 88]

$$
\begin{aligned}
i\frac{\partial}{\partial t}\Psi_1 &= \left[-\lambda\frac{\partial^2}{\partial x^2} + g_{11}|\Psi_1|^2 + g_{12}|\Psi_2|^2\right]\Psi_1 \\
i\frac{\partial}{\partial t}\Psi_2 &= \left[-\frac{\partial^2}{\partial x^2} + s\cos^2(x) + g_{21}|\Psi_1|^2 + g_{22}|\Psi_2|^2\right]\Psi_2
\end{aligned}
\tag{4.38}
$$

that here are written in dimensionless form, with lengths in units of the lattice wavevector $k_{lat} = 2\pi/\lambda_{opt}$, and the height of the lattice s in units of the recoil energy $E_R = \hbar^2 k_{lat}^2/2m_2$. The coupling constants can be expressed in terms of the scattering lengths a_{ij} and of the mean densities in each site of the lattice n_i as $g_{ij} = 2^{2+\delta_{ij}}\pi\sqrt{n_i n_j}a_{ij}\lambda^{\delta_{i1}\delta_{j1}}[1 + \lambda(1 - \delta_{ij})]/k_{lat}^2$, with $\lambda = m_2/m_1$ (notice that $g_{12} = g_{21}$). With this choice, the wavefunctions Ψ_i are normalized to unity over a single period.

It is well-known that eq. (4.38) admits stationary solutions in the form of Bloch waves

$$\Psi_j(x) = e^{i(\mu_j t - kx)}\phi_j(k, x), \tag{4.39}$$

where $\phi_j(k, x)$ has the same periodicity of the lattice. The Bloch wave vector k represents the condensate quasimomentum (restricted to the first Brillouin zone), and μ_j is the chemical potential of each species. For investigating the stability of these Bloch states, we consider three different configurations that can be experimentally realized:

A) BEC1 propagates through BEC2 at rest: $k_1 = k$, $k_2 = 0$.

B) analogous to the former, but with the role of the two condensate exchanged: $k_1 = 0$, $k_2 = k$.

C) both condensate are moving with the same quasimomentum: $k_1 = k_2 = k$.

As for the case of a single condensate, two kinds of instability are relevant for this system, namely energetic (or Landau) and dynamical instabilities. Energetic instability takes place when the stationary solution of the GP equation is no longer a local minimum of the energy functional, and the system can lower its energy by emitting phononic excitations. This happens, for instance, when a condensate flows with velocity larger than the Bogoliubov sound velocity, and corresponds to the Landau criterion of superfluidity [79]. Instead, dynamical instability occurs when the frequency of some of the eigenmodes of the system get a nonzero imaginary part. Therefore, the occupation of these modes, if initially non-vanishing, may grow exponentially in time, rapidly driving the system away from the steady state.

The instability analysis can be performed by considering the stability of the system against small perturbations, writing

$$\Psi_j(x) = e^{i(\mu_j t - kx)}\left[\phi_j(k, x) + \delta\phi_j(k, x)\right], \tag{4.40}$$

according to Bogoliubov theory [92]. For the case of energetic instability the excitations can be decomposed in terms of Bloch waves of quasimomentum q as [79]

$$\delta\phi_j = \frac{1}{\sqrt{n_j}}\left(u_{k,q}^{(j)}(x)e^{iqx} + v_{k,q}^{(j)*}(x)e^{-iqx}\right) \tag{4.41}$$

where the functions u and v have the same spatial periodicity of the lattice and satisfy the relation

$$\int dx\, u_{k,q}^{(i)*}u_{k,q}^{(j)} - v_{k,q}^{(i)*}v_{k,q}^{(j)} = \pm\delta_{ij}, \tag{4.42}$$

where $\pm$ refer to the quasiparticle (phonon) and antiquasiparticle (antiphonon) sector of the spectrum, respectively [79, 85, 92].

Writing the stationary GPEs for the wave function (4.41) with (4.42), and dropping all the terms non linear in the fluctuations, we can find that the u and v functions satisfy the following eigenvalue equation

$$M(q)X = E(q)X\,, \qquad X = \begin{pmatrix} u^{(1)} \\ v^{(1)} \\ u^{(2)} \\ v^{(2)} \end{pmatrix}. \tag{4.43}$$

The matrix $M(q)$ is given by

$$M(q) = \begin{pmatrix} M^{(1)}_{k_1,q} & I_{12} \\ I_{21} & M^{(2)}_{k_2,q} \end{pmatrix} \tag{4.44}$$

with

$$M^{(i)}_{k,q} = \begin{pmatrix} \mathcal{L}_i(q+k) & g_{ii}\phi_i^2 \\ g_{ii}\phi_i^{*2} & \mathcal{L}_i(q-k) \end{pmatrix}, \tag{4.45}$$

whose diagonal terms are defined by

$$\mathcal{L}_j(k) = -\lambda^{2-j}\left(\frac{\partial^2}{\partial x^2} + ik\right)^2 + (j-1)s\cos^2(x) + $$
$$-\mu_j + 2g_{j,j}|\phi_j|^2 + g_{j,3-j}|\phi_{3-j}|^2, \tag{4.46}$$

while

$$I_{ij} = g_{ij}\begin{pmatrix} \phi_i\phi_j^* & \phi_i\phi_j \\ \phi_i^*\phi_j^* & \phi_i^*\phi_j \end{pmatrix}. \tag{4.47}$$

The energetic instability occurs when the condensate flow corresponding to a Bloch wave is no more a local minimum of the energy functional, that is when the $M_k(q)$ matrix has negative eigenvalues [79].

For the case of dynamical instability we look for time-dependent fluctuation of the form

$$\delta\phi_j = \frac{1}{\sqrt{n_j}}\left(u^{(j)}_{k,q}(x)e^{i(qx-\omega_{kq}t)} + v^{(j)*}_{k,q}(x)e^{-i(qx-\omega_{kq}t)}\right) \tag{4.48}$$

yielding the following Bogoliubov equations [79, 89, 90]

$$\Sigma_3 M(q)X = \omega_{kq}X\,, \qquad \Sigma_3 = \begin{pmatrix} \sigma_3 & 0 \\ 0 & \sigma_3 \end{pmatrix} \tag{4.49}$$

where σ_3 is the third Pauli matrix. Dynamical instability occurs when some of the eigenfrequencies ω_{kq} get a non-zero imaginary part, indicating an exponential

growth of the corresponding modes, that rapidly drive the system away from the steady state in the dynamical evolution.

The eigenvectors X are unknown but the u and v functions can be projected on a Fourier basis:

$$u_i = \sum_{s=-n}^{n} \alpha_{i,s} e^{iskx} \tag{4.50}$$

$$v_i = \sum_{s=-n}^{n} \beta_{i,s} e^{iskx}, \tag{4.51}$$

such that the resulting $4(n+1) \times 4(n+1)$ matrix equations can be easily solved by means of standard LAPACK routines.

In the following, for obvious reasons, it will be considered the case of a ^{87}Rb -^{41}K mixture with tunable interspecies interactions and with an optical lattice of wavelength $\lambda_{opt} = 790$ nm and linear polarization. Hence the condensate of ^{87}Rb will experience no optical potential, playing therefore the role of BEC1, while the ^{41}K is subjected to the optical lattice, being BEC2. The mean densities will be also fixed to 10 particles per lattice site, corresponding to the following values of the intraspecies couplings: $g_{11} \simeq 0.021$, $g_{22} \simeq 0.027$. However, the effects that will be presented can be obtained in a wide range of parameters, with different species or different lattice periodicity.

The typical stability diagrams in the $k-q$ plane, obtained by numerical diagonalization of eqs. (4.43) and (4.49) are shown in Fig. 4.10 (for the case A and B) and in Fig. 4.11 (case C), for different values of the lattice intensity s and interspecies interaction g_{12}. In all three cases, the energetic stability behaviour is similar to that of the single species [79], whereas the regions of dynamical instability show a very different and richer behaviour, due to the coupling between the two condensates (as we will see in the following).

In particular, the configuration A resembles the case of a single *attractive* condensate [86], where the instability starts at low condensate quasimomenta (low k) and initially pertains only to long wavelength excitations (low q), with the difference that in the present case there are additional instability regions due to the interspecies interaction, and the system cannot be stabilized by tuning the condensate quasimomentum. Configurations B and C show instead a more complex behaviour, where the previous effects add up with the usual instability of a repulsive condensate moving in an optical lattice (concerning modes that become unstable for $k > 0.5$) [79, 80, 81, 83, 84, 85]. Even in these cases the scenario is complicated by the appearance of further instability regions.
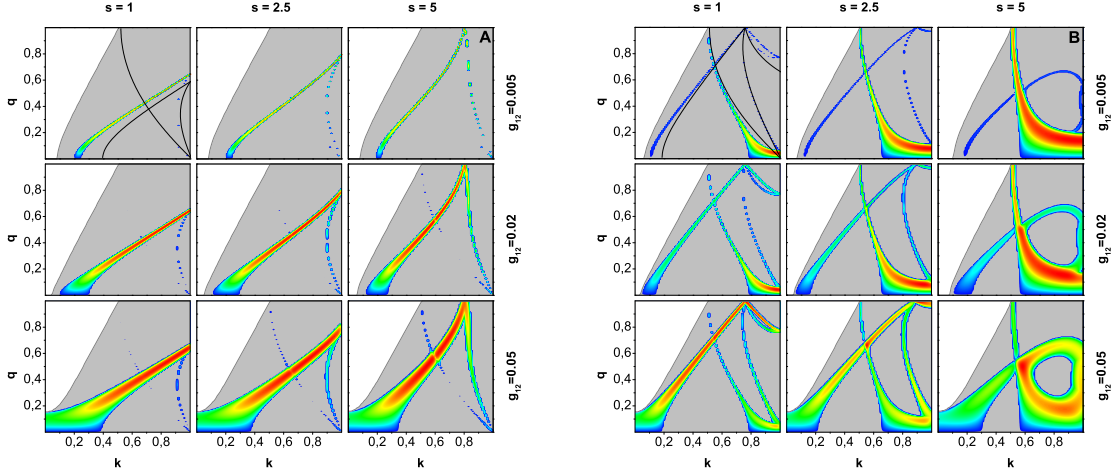
Figure 4.10: Configurations A (left) and B (right): stability diagrams as a function of the quasimomenta k of the condensates and and q of the excitations, for different values of s and g_{12}. In the light shaded region the system is energetically unstable. Regions in color scale indicate where the system is also dynamically unstable. The intensity of the color scale corresponds to the growth rate of the unstable modes ($\propto \mathrm{Im}(\omega_{kq})$). Solid lines: coupling between phonon-antiphonon modes in the limit $s \to 0$, $g_{12} \to 0$ (see text).

Notably, the fact that for large enough repulsion between the two species the system becomes unstable also for low k values in all the three configurations (see the bottom row diagrams), is related to occurrence of a phase separation instability [93, 94, 89, 90] for $g_{12} > \sqrt{g_{11}g_{22}}$ (here the critical interaction strength is $g_{12}^c = 0.018$).

We can now analyze in more details the structure of the dynamical unstable regions. Since these instabilities are determined by the mixing of both components, it is instructive to know to which extent they contribute. This can be done by considering the norm V_i of the projection of the unstable modes along each of the two components, $V_i(k,q) = \int_x |u_{k,q}^{(i)}(x)|^2 + |v_{k,q}^{(i)}(x)|^2$, and defining the *mixing ratio* η as

$$\eta(k,q) = \frac{V_1(k,q) - V_2(k,q)}{V_1(k,q) + V_2(k,q)} \tag{4.52}$$

that ranges between -1 and 1, being positive (negative) when the major component corresponds to the BEC1 (BEC2), and close to zero when the contribution of the two BECs is almost the same. This indicator is shown explicitly for the configuration C in Fig. 4.11, since this is the case that presents the most complex mixing
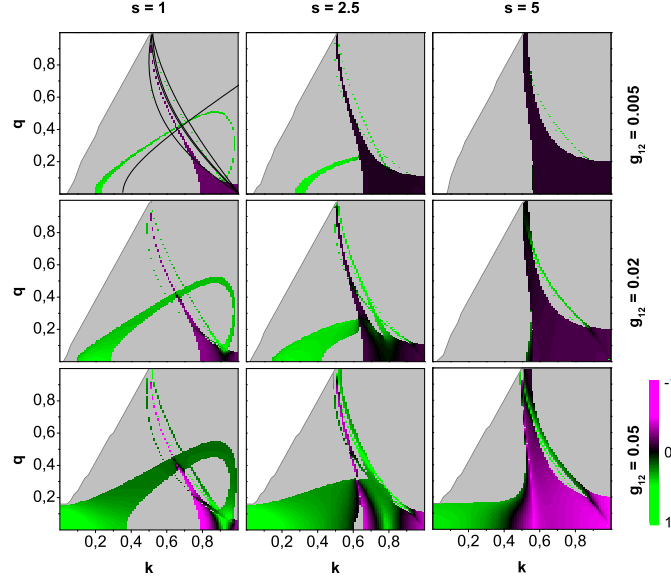
Figure 4.11: The same notations as Fig. 4.10 but for configuration C. Here the color scale corresponds to the values of $\eta(k, q)$ in the dynamically unstable regions, measuring the relative weight of each species.

behaviour (due to the fact that both condensate quasimomenta are non vanishing). In particular, it emerges that the instability at low values of k gets the primary contribution from BEC1, whereas that at higher k is dominated by BEC2. Instead, for the configurations A and B of Fig. 4.10 η is mostly positive (A) or negative (B).

Analytic Limits

We can better understand the origin of the dynamical instability regions considering the limit of vanishing lattice, $s \to 0$, and vanishing interspecies interactions, $g_{12} \to 0$. In this case $I_{ij} = 0$, the matrices $M_k^{(i)}(q)$ read

$$M_k^{(i)}(q) = \begin{pmatrix} \lambda^{\delta_{i1}}(q^2 + 2kq) + g_{ii} & g_{ii} \\ g_{ii} & \lambda^{\delta_{i1}}(q^2 - 2kq) + g_{ii} \end{pmatrix} \qquad (4.53)$$

and the full matrix $\Sigma_3 M(q)$ is block diagonal. Hence, the two species are decoupled and the eigenvectors have the form $X^{(1)} = [u^{(1)}, v^{(1)}, 0, 0]$ and $X^{(2)} = [0, 0, u^{(2)}, v^{(2)}]$, with eigenvalues that will be indicated as $\omega_{\pm}^1$ and $\omega_{\pm}^2$ respectively (the $\pm$ refers to the positive and negative sectors of the spectrum [79]). In this limit the four eigenvalues $\omega_{\pm}^1$ and $\omega_{\pm}^2$ have a simple analytical expression in all the three configurations; they
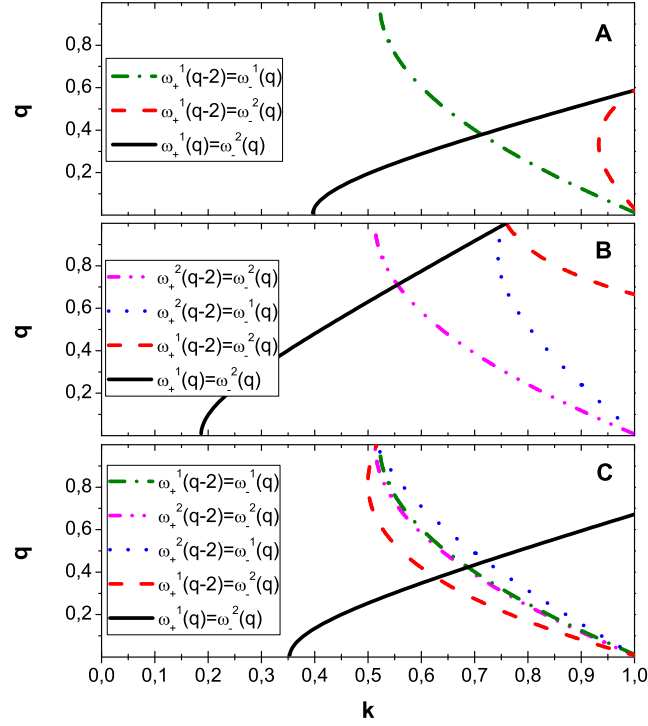
Figure 4.12: Analytical solutions for the coupling of the phonon and antiphonon modes in the limit $s \to 0$, $g_{12} \to 0$ for the three configurations A,B and C.

are always real and therefore the system is dynamically stable. However, as soon as $s \neq 0$ and $g_{12} \neq 0$, a resonant coupling between phonon and antiphonon modes may cause the appearance of an imaginary component in the spectrum, and hence dynamical instability. Indeed, owing to the properties of the matrix $\Sigma_3 M(q)$, complex eigenvalues can appear only in pairs, so that the onset of instability is signaled by the appearance of a pair of real degenerate eigenvalues [79].

Notably, in all the three cases, there are several ways to couple phonon and antiphonon modes, due to the fact that besides the usual intraspecies coupling [79] here we can also have interspecies resonances, namely $\omega_+^i(q-2) = \omega_-^i(q)$, $\omega_+^i(q-2) = \omega_-^j(q)$, and $\omega_\pm^i(q) = \omega_\mp^j(q)$. The curves corresponding to the possible resonances lying in the range $k, q \in [0, 1]$ are reported in Fig. 4.12 for each of the three configurations A,B or C. They are also reported in the top left panels in Figs. 4.10 and 4.11. As we move away from the analytic limit, both by increasing the interspecies interactions g_{12} or the lattice intensity s, the strong mixing between the

different modes eventually causes a broadening and a deformation of the instability regions.

Remarkably the seeding of most of the instabilities is the coupling of a phonon (antiphonon) mode of the species 1 with an antiphonon (phonon) mode of the species 2, i.e., the excitation of the matter grating can interfere with those of the matter wave. This situation is completely different with respect to the case of a single condensate in an optical lattice, since the latter cannot support excitations. Therefore, these features make the possibility to load multicomponent BECs with tunable interspecies interactions in SSDP optical lattices a very interesting opportunity for studying the interplay of nonlinearity and periodicity in novel regimes.

Conclusions

In this thesis I presented the results of the work made in one of the LENS laboratories during the three years of my PhD. In this period our research activities have been focused on the exploration of a new field in the realm of cold atomic physics: the Bose-Bose mixtures.

The experimental apparatus, described in chapter 2, has proven to be an excellent and versatile toolbox that has allowed us to study and to characterize many aspects of the physics of two distinguishable interacting Bose gases. Indeed, the experiments presented here cover a wide and heterogeneous range of physical phenomena: from the association of heteronuclear ultracold few-body particles to the characterization of fundamental physics, such as the entropy exchange between two gases near the absolute zero.

The most intriguing and interesting feature of cold atomic physics is the possibility to experimentally realize many models that have been introduced in other fields of physics in order to give an approximate and simple description of real systems (solid state physics, condensed matter physics, nuclear physics...). The peculiar key feature is the absolute control on all the parameters of the system, being them the interactions as well as the entropy or the temperature. In particular, as shown in chapter 3, the ability to tune the interactions at will, by means of Feshbach resonances, has allowed us to investigate the physics of few-body systems. Indeed, we have been able to associate heteronuclear ultracold molecules starting from two atomic clouds. The most important property of these molecules is the long-range interaction that arise from their permanent electric dipole moments (once they are transferred in the vibrational ground state) and that candidate them as possible qubits as well as the constituents of a dipolar Bose-Einstein condensate. Moreover, in our laboratory, it has been demonstrated, for the first time, the existence of Efimov physics in asymmetric systems. These systems of distinguishable particles characterized by only two resonant interactions, have been sought, without success, for more than 35 years in nuclear physics. Our research, due to the universality of

the Efimov scenario, permits to extend this theory also at the case of halo nuclei.

Another interesting aspect that is peculiar in mixtures is the possibility to selectively act on just one of the two species. This, as shown in chapter 4, has been done in our experiment by means of a species-selective dipole potential. Exploiting this kind of potential we have been able to adiabatically compress the K sample, leaving the Rb atoms almost unperturbed. Due to the interspecies collisions the two clouds are always in thermal equilibrium, hence, they exchange entropy. We have characterized this entropy exchange and we have used it to implement a novel scheme to reversibly reach the Bose-Einstein condensation for K atoms. Moreover, exploiting a species-selective optical lattice and the tunabilty of the interactions, we have studied the fascinating system composed by two distinguishable interacting atomic clouds in different dimensions. We have observed and characterized several inter-dimensional resonances. Our results represent the first experimental signature of inter-dimensional physics, that is expected to take place in a wide range of phenomena, such as the Coulomb interactions between 2D electrons in graphene or the existence of extra-dimensions in cosmology. Another interesting scenario would arise once the species-selective optical lattice is used on a double Bose-Einstein condensate. In this case the interactions of a matter wave with a matter grating could be studied and, as shown in this thesis, many instability regimes would take place from the coupling of the matter wave phonons with those of the matter grating.

In the future a three dimensional optical lattice setup will be implemented on our apparatus. This will allow us to study the few-body physics avoiding collisions between the few-body particles and the atomic background. Indeed, if we manage to place two or three atoms in each lattice site, we can then associate long-living molecules or Efimov states and we can use these particles as fundamental tools to engineer spin hamiltonians. Another interesting scenario would arise with two degenerate species with tunable interactions in a three-dimensional optical lattice. For this system a rich phase diagram with many exotic phases is expected to occur when the interspecies scattering length or the height of the lattice is varied [95]. Moreover one can use the two species in the optical lattice to simulate spin hamiltonians like the XXZ Heisenberg model, where the Rb atoms play the role of the spin-up particles while the K atoms the role of the spin-down particles.

Many open questions still lie on this route. In particular the detection technique for these spin-like phases is lacking and the achievement of the temperatures that are necessary to the onset of such phases will be the most challenging task for future experiments. The results presented here are useful for this purpose indeed Feshbach

resonances give the extraordinary possibility of tuning the interspecies scattering length to the limit of zero interactions and the SSDP allows efficient cooling and thermometry.

Bibliography

[1] *Bose-Einstein Condensation in a Gas of Sodium Atoms*, K. B. Davis, M. -O. Mewes, M. R. Andrews, N. J. van Druten, D. S. Durfee, D. M. Kurn, and W. Ketterle, Phys. Rev. Lett. 75, 3969 (1995)

[2] *Observation of Bose-Einstein Condensation in a Dilute Atomic Vapor*, M. H. Anderson, J. R. Ensher, M. R. Matthews, C. E. Wieman, and E. A. Cornell, Science 269, 198 (1995)

[3] *Evidence of Bose-Einstein Condensation in an Atomic Gas with Attractive Interactions*, C. C. Bradley, C. A. Sackett, J. J. Tollett, and R. G. Hulet, Phys. Rev. Lett. 75, 1687 (1995)

[4] *Onset of Fermi Degeneracy in a Trapped Atomic Gas*, B. DeMarco and D. S. Jin, Science 285, 1703 (1999)

[5] *Quantum phase transition from a superfluid to a Mott insulator in a gas of ultracold atoms*, Markus Greiner, Olaf Mandel, Tilman Esslinger, Theodor W. Hänsch, Immanuel Bloch, Nature 415, 39 (2002)

[6] *Atom-molecule coherence in a Bose-Einstein condensate*, Elizabeth A. Donley, Neil R. Claussen, Sarah T. Thompson, Carl E. Wieman, Nature 417, 529 (2002)

[7] *Creation of ultracold molecules from a Fermi gas of atoms*, Cindy A. Regal, Christopher Ticknor, John L. Bohn, Deborah S. Jin, Nature 424, 47 (2003)

[8] *Evidence for Efimov quantum states in an ultracold gas of caesium atoms.* T. Kraemer, M. Mark, P. Waldburger, J. G. Danzl, C. Chin, B. Engeser, A. D. Lange, K. Pilch, A. Jaakkola, H.-C. Nagerl, R. Grimm., Nature, 440, 315 (2006)

[9] *Optimizing a Phase Gate Using Quantum Interference*, E. Charron, E. Tiesinga, F. Mies and C. Williams, Phys. Rev. Lett. 88, 077901 (2002)

[10] *Micro-optical Realization of Arrays of Selectively Addressable Dipole Traps: A Scalable Configuration for Quantum Computation with Atomic Qubits*, R. Dumke, M. Volk, T. Müther, F. B. J. Buchkremer, G. Birkl and W. Ertmer, Phys. Rev. Lett. 89, 097903 (2002)

[11] *Elements of Quantum Gases: Thermodynamic and Collisional Properties of Trapped Atomic Gases*, J.T.M. Walraven, University of Amsterdam, 2009

[12] *Collisional and molecular spectroscopy in an ultracold Bose-Bose mixture*, G. Thalhammer, G. Barontini, J. Catani, F. Rabatti, C. Weber, A. Simoni, F. Minardi and M. Inguscio, New J. Phys. 11, 055044 (2009)

[13] *High-precision calculations of van der Waals coefficients for heteronuclear alkali-metal dimers*, A. Derevianko, J. F. Babb, and A. Dalgarno, Phys. Rev. A 63, 052704 (2001)

[14] *Production of cold molecules via magnetically tunable Feshbach resonances*, Thorsten Kohler, Krzysztof Goral, and Paul S. Julienne, Rev. Mod. Phys. 78, 1311 (2006)

[15] *Theory of Bose-Einstein condensation in trapped gases*, Franco Dalfovo, Stefano Giorgini, Lev P. Pitaevskii, Sandro Stringari, Rev. Mod. Phys. 71, 463 (1999)

[16] *Damping and frequency shift in the oscillations of two colliding Bose-Einstein condensates*, M. Modugno, C. Fort, P. Maddaloni, F. Minardi and M. Inguscio, Eur. Phys. J. D 17 (2001)

[17] *Direct evaporative cooling of ^{41}K into a Bose-Einstein condensate* , T. Kishimoto, J. Kobayashi, K. Noda, K. Aikawa, M. Ueda, and S. Inouye, Phys. Rev. A 79, 031602 (2009)

[18] *Heterodyne saturation spectroscopy through frequency modulation of the saturating beam*, G. Camy, C. J. Borde, M. Ducloy, Optics Communications 41, 325 (1982)

[19] *A new apparatus for ultracold K-Rb Bose-Bose atomic mixtures*, J. Catani, Ph.D. thesis, Università di Firenze (2006).

[20] *Ultracold bosonic mixtures: cold collisions and optical lattices*, L. De Sarlo, Ph.D. thesis, Università di Firenze (2007).

[21] *Intense slow beams of bosonic potassium isotopes*, J. Catani, P. Maioli, L. De Sarlo, F. Minardi and M. Inguscio, Phys. Rev. A 73, 033415 (2006)

[22] *Bose-Einstein Condensation of Potassium Atoms by Sympathetic Cooling*, G. Modugno, G. Ferrari, G. Roati, R. J. Brecha, A. Simoni, and M. Inguscio, Science 9 1320-1322 (2001)

[23] *Optical Dipole Traps for Neutral Atoms*, Rudolf Grimm, Matthias Weidemüller, Yurii B. Ovchinnikov Adv. In Atomic, Molecular, and Optical Physics, Volume 42, 95 (2000)

[24] *Near-threshold model for ultracold KRb dimers from interisotope Feshbach spectroscopy*, Andrea Simoni, Matteo Zaccanti, Chiara D'Errico, Marco Fattori, Giacomo Roati, Massimo Inguscio, and Giovanni Modugno, Phys. Rev. A 77, 052705 (2008)

[25] *Double Species Bose-Einstein Condensate with Tunable Interspecies Interactions*, G. Thalhammer, G. Barontini, L. De Sarlo, J. Catani, F. Minardi, and M. Inguscio, Phys. Rev. Lett. 100, 210402 (2008)

[26] *Association of ultracold double-species bosonic molecules*, C. Weber, G. Barontini, J. Catani, G. Thalhammer, M. Inguscio, and F. Minardi, Phys. Rev. A 78, 061601 (2008)

[27] *Observation of heteronuclear atomic Efimov resonances* , G. Barontini, C. Weber, F. Rabatti, J. Catani, G. Thalhammer, M. Inguscio, F. Minardi, Phys. Rev. Lett. 103, 043201 (2009)

[28] Andrea Simoni, private communication.

[29] *Three-Body Recombination of Ultracold Atoms to a Weakly Bound s Level*, P. O. Fedichev, M. W. Reynolds, and G. V. Shlyapnikov, Phys. Rev. Lett. 77, 2921 (1996)

[30] *Production of Long-Lived Ultracold Li_2 Molecules from a Fermi Gas*, J. Cubizolles, T. Bourdel, S. J. J. M. F. Kokkelmans, G. V. Shlyapnikov, and C. Salomon, Phys. Rev. Lett. 91, 240401 (2003)

[31] *Observation of Molecules Produced from a Bose-Einstein Condensate*, Stephan Dürr, Thomas Volz, Andreas Marte, and Gerhard Rempe, Phys. Rev. Lett. 92, 020406 (2004)

[32] *Dissociation of ultracold molecules with Feshbach resonances*, Stephan Dürr, Thomas Volz, and Gerhard Rempe, Phys. Rev. A 70, 031601 (2004)

[33] *Preparation of a Pure Molecular Quantum Gas*, Jens Herbig, Tobias Kraemer, Michael Mark, Tino Weber, Cheng Chin, Hanns-Christoph Nägerl, and Rudolf Grimm, Science 301, 1510 (2003)

[34] *Pure Gas of Optically Trapped Molecules Created from Fermionic Atoms*, S. Jochim, M. Bartenstein, A. Altmeyer, G. Hendl, C. Chin, J. Hecker Denschlag, and R. Grimm, Phys. Rev. Lett. 91, 240402 (2003)

[35] *Conversion of an Atomic Fermi Gas to a Long-Lived Molecular Bose Gas*, Kevin E. Strecker, Guthrie B. Partridge, and Randall G. Hulet, Phys. Rev. Lett. 91, 080406 (2003)

[36] *Formation of Quantum-Degenerate Sodium Molecules*, K. Xu, T. Mukaiyama, J. R. Abo-Shaeer, J. K. Chin, D. E. Miller, and W. Ketterle, Phys. Rev. Lett. 91, 210402 (2003)

[37] *Ultracold Heteronuclear Molecules in a 3D Optical Lattice*, C. Ospelkaus, S. Ospelkaus, L. Humbert, P. Ernst, K. Sengstock, and K. Bongs, Phys. Rev. Lett. 97, 120402 (2006)

[38] *Collisional Stability of Fermionic Feshbach Molecules*, J. J. Zirbel, K.-K. Ni, S. Ospelkaus, J. P. D'Incao, C. E. Wieman, J. Ye, and D. S. Jin, Phys. Rev. Lett. 100, 143201 (2008)

[39] *Heteronuclear molecules in an optical dipole trap*, J. J. Zirbel, K.-K. Ni, S. Ospelkaus, T. L. Nicholson, M. L. Olsen, P. S. Julienne, C. E. Wieman, J. Ye, and D. S. Jin, Phys. Rev. A 78, 013416 (2008)

[40] *Radio-frequency association of heteronuclear Feshbach molecules*, C. Klempt, T. Henninger, O. Topic, M. Scherer, L. Kattner, E. Tiemann, W. Ertmer, and J. J. Arlt, Phys. Rev. A 78, 061602 (2008)

[41] *Observation of Heteronuclear Feshbach Molecules from a ^{85}Rb-^{87}Rb Gas* S. B. Papp and C. E. Wieman, Phys. Rev. Lett. 97, 180404 (2006)

[42] *Ultracold Heteronuclear Fermi-Fermi Molecules* A.-C. Voigt, M. Taglieber, L. Costa, T. Aoki, W. Wieser, T. W. Hansch, and K. Dieckmann, Phys. Rev. Lett. 102, 020405 (2009)

[43] *Molecules in a Bose-Einstein Condensate*, Roahn Wynar, R. S. Freeland, D. J. Han, C. Ryu, and D. J. Heinzen, Science 287, 1016 (2000)

[44] *Time-Dependent Feshbach Resonance Scattering and Anomalous Decay of a Na Bose-Einstein Condensate*, F. A. van Abeelen and B. J. Verhaar, Phys. Rev. Lett. 83, 1550 - 1553 (1999)

[45] *Manipulation of Feshbach resonances in ultracold atomic collisions using time-dependent magnetic fields*, F. H. Mies, E. Tiesinga, and P. S. Julienne, Phys. Rev. A 61, 022721 (2000)

[46] *Ultracold Molecule Production via a Resonant Oscillating Magnetic Field*, S. T. Thompson, E. Hodby, and C. E. Wieman, Phys. Rev. Lett. 95, 190404 (2005)

[47] *Quantum Computation with Trapped Polar Molecules*, D. DeMille, Phys. Rev. Lett. 88, 067901 (2002)

[48] *A toolbox for lattice-spin models with polar molecules*, A. Micheli, G. K. Brennen, P. Zoller, Nature Physics 2, 341 (2006)

[49] *Quantum Phases of Dipolar Bosons in Optical Lattices*, K. Góral, L. Santos, and M. Lewenstein, Phys. Rev. Lett. 88, 170406 (2002)

[50] *Bose-Einstein Condensation in Trapped Dipolar Gases*, L. Santos, G. V. Shlyapnikov, P. Zoller, and M. Lewenstein, Phys. Rev. Lett. 85, 1791 (2000)

[51] *Association of heteronuclear molecules in a harmonic oscillator well*, Jesper Fevre Bertelsen and Klaus Molmer, Phys. Rev. A 76, 043615 (2007)

[52] *Energy levels arising from resonant two-body forces in a three-body system*, V. Efimov, Phys. Lett. 33B, 563 (1970)

[53] *Weakly-bound states of three resonantly-interacting particles*, V. Efimov, Sov. J. Nucl. Phys. 12, 589 (1971)

[54] *Universality in few-body systems with large scattering length*, E. Braaten and H. -W. Hammer, Physics Reports 428, 259 (2008)

[55] *Structure and reactions of quantum halos*, A. S. Jensen, K. Riisager, D. V. Fedorov, and E. Garrido, Rev. Mod. Phys. 76, 215 (2004)

[56] *Observation of an Efimov spectrum in an atomic system*, M. Zaccanti, B. Deissler, C. D'Errico, M. Fattori, M. Jona-Lasinio, S. Müller, G. Roati, M. Inguscio, G. Modugno, Nature Physics 5, 586 (2009)

[57] *Efimov states in asymmetric systems*, A. S. Jensen, D. V. Fedorov, Europhys. Lett. 62,336 (2003)

[58] *Enhancing the observability of the Efimov effect in ultracold atomic gas mixtures*, J. P. D'Incao and B. D. Esry, Phys. Rev. A 73, 030703 (2006)

[59] *Limits on Universality in Ultracold Three-Boson Recombination*, J. P. D'Incao, H. Suno, and B. D. Esry, Phys. Rev. Lett. 93, 123201 (2004)

[60] *Observation of an Efimov-like trimer resonance in ultracold atom-dimer scattering*, S. Knoop, F. Ferlaino, M. Mark, M. Berninger, H. Schöbel, H.-C. Nägerl, R. Grimm, Nature Physics 5, 227 (2009)

[61] *Entropy exchange in a mixture of ultracold atoms* , J. Catani, G. Barontini, G. Lamporesi, F. Rabatti, G. Thalhammer, F. Minardi, S. Stringari, M. Inguscio, Phys. Rev. Lett. 103, 140401 (2009)

[62] *Instabilies of a matter wave in a matter grating* , Giovanni Barontini, Michele Modugno, Phys. Rev. A 80, 063613 (2009)

[63] *Ultracold atomic gases in optical lattices: Mimicking condensed matter physics and beyond*, Maciej Lewenstein, Anna Sanpera, Veronica Ahufinger, Bogdan Damski, Aditi Sen(De), and Ujjwal Sen, Adv. Phys. 56, 243 (2007)

[64] *Bose-Einstein condensation*, L. Pitaevskii and S. Stringari, Oxford University Press, Oxford, 2003

[65] *Thermodynamics of a trapped Bose-condensed gas*, S. Giorgini, L. P. Pitaevskii and S. Stringari, J. Low Temp. Phys., 109, 1-2 (1997)

[66] *Analytical description of a trapped semi-ideal Bose gas at finite temperature*, M. Naraschewski, D. M. Stamper-Kurn, Phys. Rev. A 58, 2423 - 2426 (1998)

[67] *Lattice thermodynamics for ultracold atoms*, D. McKay, M. White, and B. De-Marco, Phys. Rev. A 79, 063605 (2009)

[68] *Zur Elektrodynamik bewegter Körper*, Albert Einstein, Annalen der Physik 17, 891 (1905)

[69] *Brane-World Gravity*, Roy Maartens, Living Rev. Relativity, 7, (2004) and references therein

[70] *Berezinskii-Kosterlitz-Thouless Crossover in a Trapped Atomic Gas* , Zoran Hadzibabic, Peter Krüger, Marc Cheneau, Baptiste Battelier , Jean B. Dalibard, Nature 441, 1118 (2006)

[71] *Vortex Proliferation in the Berezinskii-Kosterlitz-Thouless Regime on a Two-Dimensional Lattice of Bose-Einstein Condensates* , V. Schweikhard, S. Tung, and E. A. Cornell, Phys. Rev. Lett. 99, 030401 (2007)

[72] *Universal Fermi Gases in Mixed Dimensions* , Y. Nishida, Phys. Rev. Lett. 101, 170401 (2008)

[73] Yusuke Nishida, unpublished notes (2009)

[74] *Three-boson problem near a narrow Feshbach resonance*, D. S. Petrov , Phys. Rev. Lett. 93, 143201 (2004)

[75] *Dynamics of Bose-Einstein condensates in optical lattices*, Oliver Morsch and Markus Oberthaler, Rev. Mod. Phys. 78, 179 (2006)

[76] *Many-body physics with ultracold gases*, Immanuel Bloch, Jean Dalibard, and Wilhelm Zwerger, Rev. Mod. Phys. 80, 885 (2008)

[77] *Bright Bose-Einstein Gap Solitons of Atoms with Repulsive Interaction*, B. Eiermann, Th. Anker, M. Albiez, M. Taglieber, P. Treutlein, K.-P. Marzlin, and M. K. Oberthaler, Phys. Rev. Lett. 92, 230401 (2004)

[78] *Discrete Solitons and Breathers with Dilute Bose-Einstein Condensates*, Andrea Trombettoni and Augusto Smerzi, Phys. Rev. Lett. 86, 2353 (2001)

[79] *Landau and dynamical instabilities of the superflow of Bose-Einstein condensates in optical lattices*, Biao Wu and Qian Niu, Phys. Rev. A 64, 061603 (2001)

[80] *Dynamical Superfluid-Insulator Transition in a Chain of Weakly Coupled Bose-Einstein Condensates* A. Smerzi, A. Trombettoni, P. G. Kevrekidis, and A. R. Bishop, Phys. Rev. Lett. 89, 170402 (2002)

[81] *Superfluid dynamics of a Bose-Einstein condensate in a periodic potential*, C Menotti, A Smerzi and A Trombettoni, New J. Phys. 5, 112 (2003)

[82]   *Band structure, elementary excitations, and stability of a Bose-Einstein condensate in a periodic potential*, M. Machholm, C. J. Pethick, and H. Smith, Phys. Rev. A 67, 053613 (2003)

[83]   *Observation of Dynamical Instability for a Bose-Einstein Condensate in a Moving 1D Optical Lattice*, L. Fallani, L. De Sarlo, J. E. Lye, M. Modugno, R. Saers, C. Fort, and M. Inguscio, Phys. Rev. Lett. 93, 140406 (2004)

[84]   *Unstable regimes for a Bose-Einstein condensate in an optical lattice*, L. De Sarlo, L. Fallani, J. E. Lye, M. Modugno, R. Saers, C. Fort, and M. Inguscio, Phys. Rev. A 72, 013603 (2005)

[85]   *Role of transverse excitations in the instability of Bose-Einstein condensates moving in optical lattices*, M. Modugno, C. Tozzo, and F. Dalfovo, Phys. Rev. A 70, 043625 (2004)

[86]   *Dynamical instability and dispersion management of an attractive condensate in an optical lattice*, G. Barontini and M. Modugno, Phys. Rev. A 76, 041601 (2007)

[87]   *Pulsating Instability of a Bose-Einstein Condensate in an Optical Lattice*, Uttam Shrestha, Marijan Kostrun, and Juha Javanainen, Phys. Rev. Lett. 101, 070406 (2008)

[88]   *Modulation instability and solitary-wave formation in two-component Bose-Einstein condensates*, Kenichi Kasamatsu and Makoto Tsubota, Phys. Rev. A 74, 013617 (2006)

[89]   *Dynamical instabilities in a two-component Bose-Einstein condensate in a one-dimensional optical lattice*, Samantha Hooley and Keith A. Benedict, Phys. Rev. A 75, 033621 (2007)

[90]   *Dynamical and energetic instabilities in multicomponent Bose-Einstein condensates in optical lattices*, J. Ruostekoski and Zachary Dutton, Phys. Rev. A 76, 063607 (2007)

[91]   *Degenerate Bose-Bose mixture in a three-dimensional optical lattice*, J. Catani, L. De Sarlo, G. Barontini, F. Minardi, and M. Inguscio, Phys. Rev. A 77, 011603 (2008)

[92] *Bose-Einstein condensation in the alkali gases: Some fundamental concepts*, Anthony J. Leggett, Rev. Mod. Phys. 73, 307 (2001)

[93] *Stability Signature in Two-Species Dilute Bose-Einstein Condensates*, C. K. Law, H. Pu, N. P. Bigelow, and J. H. Eberly, Phys. Rev. Lett. 79, 3105 (1997)

[94] *Binary Bose-Einstein condensate mixtures in weakly and strongly segregated phases*, P. Ao and S. T. Chui, Phys. Rev. A 58, 4836 (1998)

[95] *Sign-Alternating Interaction Mediated by Strongly-Correlated Lattice Bosons*, S.G. Söyler, B. Capogrosso-Sansone, N.V. Prokof'ev, B.V. Svistunov, New J. Phys. 11, 073036 (2009)